Towards Silicon Nanowire Based Resonant Systems

Noel Arellano

Electrical Engineering and Computer Sciences
University of California at Berkeley

Technical Report No. UCB/EECS-2008-61

http://www.eecs.berkeley.edu/Pubs/TechRpts/2008/EECS-2008-61.html

May 20, 2008

Copyright © 2008, by the author(s).
All rights reserved.

Permission to make digital or hard copies of all or part of this work for personal or classroom use is granted without fee provided that copies are not made or distributed for profit or commercial advantage and that copies bear this notice and the full citation on the first page. To copy otherwise, to republish, to post on servers or to redistribute to lists, requires prior specific permission.

Towards Silicon Nanowire Based Resonant Systems

by

Noel Arellano

B.S. (University of Illinois at Chicago) 2000

M.S. (University of California, Berkeley) 2004

A dissertation submitted in partial satisfaction of the
requirements for the degree of
Doctor of Philosophy
in

Engineering – Electrical Engineering and Computer Sciences

in the

GRADUATE DIVISION

of the

UNIVERSITY OF CALIFORNIA at BERKELEY

Committee in charge:

Professor Roger T. Howe, Co-Chair
Professor Jeffrey Bokor, Co-Chair
Professor Roya Maboudian
Professor Richard M. White

Spring 2008

The dissertation of Noel Arellano is approved:

Co-Chair	Date
Co-Chair	Date
	Date
	Date

University of California at Berkeley

Spring 2008

Towards Silicon Nanowire Based Resonant Systems

Copyright 2008

by

Noel Arellano

Abstract

Towards Silicon Nanowire Based Resonant Systems

by

Noel Arellano

Doctor of Philosophy in Engineering – Electrical Engineering and Computer Sciences

University of California at Berkeley

Professor Roger T. Howe, Co-Chair

Professor Jeffrey Bokor, Co-Chair

Silicon nanowires have attracted a lot of interest from both the nano- and microelectromechanical systems (NEMS and MEMS) communities due to their small size. Their small mass facilitates the creation of high frequency NEMS resonators for sensing or electromechanical signal processing applications. Due to their low stiffness and small mass, silicon nanowires are also ideally suited to replace microscale coupling beams in high quality factor MEMS filters. Nanowire coupled MEMS filters could, in theory, achieve smaller bandwidths and lower passband distortion than microscale-beam coupled MEMS filters.

This dissertation investigates the feasibility of using silicon nanowires as mechanical coupling beams in microscale resonant systems with resonant frequencies ranging from 14 to 19 MHz. Silicon nanowires, typically 400 to 200 nm wide, 6.2 μm long and 275 nm thick, are used as flexural coupling elements tethering two MEMS clamped-clamped resonators (L = 10 μm, W = 3.1 μm, and T = 275 nm). The resonant

systems are measured in a two-port capacitive configuration; one MEMS resonator is actuated electrostatically with a polysilicon electrode suspended 100 nm above it, mechanical energy is then transmitted to the other resonator via the silicon nanowire coupling beam and resonant motion is sensed capacitively with the second MEMS resonator electrostatically coupled to a second polysilicon electrode. The coupled resonant systems vibrate in two modes and the ratio of the nanowire coupler stiffness to the effective stiffness of the MEMS resonators determines the frequency span between the two resonant modes which varies from a maximum of 1.49 MHz to a minimum of 60 kHz. The frequency span of the resonant system is tuned by attaching the nanowire coupler at two different locations along the length of the MEMS resonators, trimming the width of the nanowire coupler with a focused ion beam, or by depositing films, such as platinum, SiC or a self assembled monolayer, on the nanowire coupler.

The silicon nanowires are fabricated using a six inch silicon-on-insulator (SOI) wafer with a device layer thickness of 275 nm and a 400 nm thick buried oxide. The nanowires are initially defined with i-line lithography which limits the achievable nanowire width to 600 nm. An oxygen plasma based ashing process is used to reduce the width of the i-line defined nanowires. Finally, the ashed photoresist patterns are etched into the device layer, using a reactive ion etching process, to define the silicon nanowires.

A new field-effect transduction technique for silicon nanowire resonators is demonstrated on single nanowire resonators and mechanically coupled nanowire resonant systems with natural frequencies ranging from 18 MHz to 135 MHz. Tri-gate polysilicon electrodes, which are capacitively coupled to both lateral surfaces of the nanowires with symmetric 60 nm gaps and the top nanowire surface with a 100 nm gap, deplete electrons

from three surfaces of vibrating silicon nanowires. A DC current on the order of 100s of microamperes flows through the nanowires while harmonic nanowire motion is induced electrostatically. As the nanowires deflect relative to the stationary tri-gate electrodes, the depletion regions on the lateral surfaces of the wire grow and recede, altering the resistance of nanowire segments located beneath the gate electrodes. For a coupled nanowire resonant system vibrating at frequency of 124.14 MHz, the resistance of the nanowire segment surrounded by one tri-gate electrode is estimated to oscillate between 1560 Ω and 1569 Ω. The oscillating resistance results in an AC current component on the order of single microamperes which is easily detected with the 50 Ω internal resistor of a network analyzer operating in the transmission mode (S_{21}), even in the presence of large parasitic capacitances.

____

Professor Roger T. Howe, Co-Chair   Date

____

Professor Jeffrey Bokor, Co-Chair   Date

Dedicado a mi padre Leocadio Arellano (Callito 1) que en paz descanse, a mi madre Ana Maria Arellano (Callito 2), a mi hermana Emilia y su esposo Oscar, a mi hermano Manuel y su esposa Gabriela, finalmente a Agustin y Nicolas, y a mis futuros sobrinos o sobrinas

Contents

1. Introduction

1.1. Silicon Nanowire Resonators……………………………………………………1

1.1.1. Resonant Mass Sensors………………………………………………………2

1.1.2. NEMS Resonators for Frequency Domain Signal Processing and Nanomechanical Computation……………………………………………3

1.2. Nanowires Mechanically Coupled to Resonant Microelectromechanical Systems (MEMS)……………………………………………………………………4

1.3. Bottom-Up Vs. Top-Down Nanowires………………………………………6

1.4. Dissertation Overview…………………………………………………………7

1.5. References………………………………………………………………………8

2. Silicon Nanowire Coupled MEMS Resonators

2.1. Introduction……………………………………………………………………11

2.2. Nanowire Coupled MEMS Resonators: Operation and Design………………12

2.2.1. Flexural-Mode Nanowire Coupled System Theory………………………14

2.3. Measurement Equipment and Testing Approach ……………………………17

2.4. Measurment Results for Nanowire Coupled MEMS Resonators……………20

2.4.1. Contact Pad Parasitic Capacitance…………………………………………25

2.5. Coupled System Tuning…………………………………………………………26

2.5.1. FIB Nanowire Trimming……………………………………………………27

2.5.2. FIB Pt Deposition on Nanowire Coupler……………………………………32

2.5.3. Frequency Span Tuning with a Self Assembled Monolayer (SAM)…..35

2.5.4. Frequency Span Tuning with High Stress SiC………………………………38

2.6. Coupled System Frequency Span Models………………………………………39

2.6.1. Maximum Velocity Coupled System Frequency Span Model……………39

2.6.2. Low Velocity Coupled System Frequency Span Model……………………46

2.6.3. Coupled System Frequency Span Model Limitations……………………49

2.7. Chapter Summary…………………………………………………………………49

2.8. References…………………………………………………………………………50

3. Silicon Nanowire and Coupled MEMS Fabrication

3.1. Introduction ………………………………………………………………………52

3.2. Top-Down Process Flow……………………………………………………………52

3.2.1. Nitride Anchors………………………………………………………………56

3.2.2. Nanowire Patterning…………………………………………………………58

3.2.3. Electrostatic Gap Formation…………………………………………………60

3.2.4. Vapor HF Release……………………………………………………………64

3.3. Focused Ion Beam Post Processing………………………………………………66

3.4. Chapter Summary…………………………………………………………………70

3.5. References…………………………………………………………………………71

4. Silicon Nanowire Resonators
4.1. Introduction…...74
4.2. Driving and Detection Techniques Overview…74
4.2.1. Capacitance Drive and Sense …75
4.2.2. Magnetomotive Transduction…76
4.2.3. Capacitive Drive and Conductivity Modulation Sense…78
4.2.4. Field-Effect detection of MEMS Resonators…80
4.3. Field-Effect Detection of Silicon Nanowire Resonators…83
4.3.1. Silicon Nanowire Resonator Design…...83
4.3.2. Polysilicon Gate Electrode Design and Device Operation…85
4.3.3. Measurement Equipment and Testing Approach…87
4.4. Linear Out-of-Phase Resonator…...90
4.4.1. Mode Verification…...93
4.4.2. Frequency Tuning…...95
4.4.3. DC Characterization…...96
4.4.4. Model of Device OP-A…98
4.4.4.1. Mechanical Domain Single 3rd Mode Nanowire Resonator…99
4.4.4.2. Electrical Domain Single 3rd Mode Nanowire Resonator…...101
4.4.4.3. ANSYS 11 Finite Element Mechanical Model for Device OP-A..106
4.4.4.4. OP-A Model Discussion and Limitations…109
4.4.5. OP-A Transconductance Calculation…...110
4.5. Nonlinear Nanowire Resonators…...112
4.5.1. (100) Nonlinear Coupled Resonators…112
4.5.2. Nonlinear 2nd Mode Nanowire Resonators…..115
4.6. Chapter Summary…...121
4.7. References…...122

5. Conclusions and Future Directions
5.1. Nanowire Coupled MEMS Resonators Conclusions…126
5.2. Silicon Nanowire Resonators Conclusions…127
5.3. Suggestions for Future Work…....128
5.3.1. Top-Down Fabrication Process …128
5.3.2. Nanowire Coupled MEMS Resonators…129
5.3.3. Silicon Nanowire Resonators…...130
5.3.4. References…132

Appendix A …...135
Appendix B…..140
Appendix C…152

Acknowledgements

I would like to begin by thanking my advisors Roger T. Howe and Roya Maboudian for their support and guidance. Roger and Roya gave me the freedom to steer my project in a variety of interesting directions. They patiently allowed me to iron out problems which I encountered during my first two fabrication attempts. I am also grateful to Professor Jeffrey Bokor for helping me with my EE grad student reviews and serving as co-chair of my dissertation committee. I would like to thank Professor Richard M. White for serving as the chair of my qualifying exam and also for serving on my dissertation committee.

I would also like to thank Dr. Emmanuel Quévy for teaching me about resonator design and teaching me some RF testing techniques. We had great brainstorming sessions concerning nanowire resonant devices and fabrication processes. He is a great collaborator and a good friend, merci beaucoup mon ami! Dr. Alvaro San Paulo performed the galvanic displacement and the preliminary nanowire growth for the top-down bottom-up hybrid process. He also became a good friend while we collaborated on the project, gracias amigo! Dr. J. Provine helped me with the focused-ion-beam post processing. He has the steady hands of a surgeon. I enjoyed the late night fib sessions at Stanford, thanks my friend!

The microlab staff did a stand up job keeping equipment running and creating extremely useful process recipes. I would like to thank Evan Stateler, David Lo, Kim Chan, Marilyn Kushner, and Jimmy Chang for all their help.

I would like to thank my fellow Howe group members for their advice and friendship. Specifically, I would like to thank Dr. Frank J. Zendejas (Frank the Bank) for

helping me countless times through out my graduate career at Berkeley. He is a great sounding board for wild ideas and is a constant source of encouragement (Gracias Carnal!). Will Holtz helped me study for prelims and gave valuable feedback for my qualifying exam talk (thanks Will!). I want to thank the G-unit (Rishi Kant), Pedro (Peter Chen), CLD (Carrie Low), Maryam, Sunny B (Sunil Bhave), and Michel Maharbiz for making my experience in the Howe group quite memorable.

I met a lot of great people during my tenure in 373 Cory Hall. Justin Black and Phil Stephanou helped me out when the vacuum probe station began to act up. Donovan Lee, Joanna Lai, Alvaro Padilla, and Wesley Chang helped me release a few die when I was in a bind (thank you). Dan Good trained me on a few pieces of equipment in the microlab (thanks). I had a blast every Friday with Wesley Chang (Rocket Boy), Yu-chih Tseng (Das Gooch) and Raymond Wong (future Wes) at the telescope makers' workshop. Tomohiro Ishikawa, his wife Mariko, Jonathan Foster and Hyuck Choo were great dining buddies, later the Vegasauri (Reynaldo Vega and Li-Wen Hung) kept me company in a few instances. Alvaro Padilla and I always had interesting lunch conversations which spanned a wide variety of topics (I will definitely miss them). Koichi Fukuda always extended an invitation every time he cooked up a storm. Ming Ting Wu (Triple M) always had crazy stories to tell from his military service days in Taiwan. He was also a good hitting partner on the tennis court. I shared hearty laughs with quite a few people including (in no particular order): Michael Helmbrecht, Cliff Knollenberg, Turi Aytur, Jaein Jeong, Daewon Ha, Gang Liu (my 143 lab mate), Mohan Dunga, Pankaj Kalra, Drew Carlson, Alejandro de la Fuente, Xin Sun, Darsen Lu, Hei

Kam, Nathan Emley, Tim Bakhishev, Steve Volkman, Qintao Zhang, and Anu Bowonder.

I would also like to thank Roya Maboudian's group for rolling out the red carpet for me: Carlo Carraro, Di Gao, Chris Roper, Greg Doerk, Brian Bush, Jingchun Zhang, Frank Del Rio, Calvin Da Rosa, Marta Cerruti, Nicola Ferralis, Wei-Cheng Lien, Fang Liu, and Ian Laboriante.

I would like to thank Carla Trujillo and Sheila Humphreys. They both helped me get into the superb undergraduate program and helped me during the first few years of my graduate career. As an undergrad in the superb program I met a lot of great friends including: my brother Bukola (Buki is always there when I need him and is always ready to give me his opinion even when I don't ask for it, ha ha ha), my sisters Debbie Senesky (she slapped me around when I needed it before quals) and Shiloe Bear (a great friend and very young at heart), Annalee Ledesma, Ayres Fan, Nadia Navarro, AJ Cantu (my roommate), Brian Lafaille, Raecine Meza, Magali Figueroa, Tanya Roosta, and Miller Allen. I also had the privilege of serving as a graduate student mentor for my little sister Sonia Arteaga (Bollywood) during the 2003 edition of the program.

I would also like to thank my friends from undergrad at UIC for their support and friendship: Gera Rangel, Peter Flores, Norma Castrejon, Walberto Ralon, Chirag, Amit, Kwamena, Josef, Mikias, Rafael, Tomas, and Luis.

Lots of love for my boys from Blue Island. There are too many of you to list here; however, I will never forget all the great times we shared. I would not be where I am without your support and friendship.

Deepti thanks for lending a sympathetic ear these last few months as I wrote this dissertation. You allowed me to vent when I thought I was going to blow my top. You always managed to make me smile whenever we talked.

Last but certainly not least I would like to thank my family for their love and support. Momma Bear, I appreciate all of the sacrifices you made to raise me and I love you very much. You always encouraged me to do my best and you taught me to appreciate everything I had. I would also like to thank my sister Emilia and brother Manuel for their unconditional love and support. They were and continue to be great role models. I always tried to emulate them in every aspect of my life, especially with regards to my academic endeavors. I would like to thank their respective spouses, Oscar and Gabriela, for taking care of them and supporting them. I also want to thank my Pops for doing all he could to provide for his family. He taught me the value of hard work and he managed to keep me out of a boat load of trouble when I was young. I really miss you Pops.

Chapter 1. Introduction

1.1 Silicon Nanowire Resonators

For this dissertation, silicon nanowires are defined as single crystal structures with lateral dimensions below 400 nm (width and height) and unconstrained lengths. Silicon nanowires have attracted a lot of attention because their small size facilitates the creation of high frequency resonators [1,2]. The natural frequency of a nanowire resonator depends on its mass:

$$f_0 \propto \sqrt{\frac{1}{m_{NW}}} \qquad (1)$$

f_0 is the resonant frequency of a nanowire resonator and m_{NW} is the active mass of a silicon nanowire. Assuming the nanowire resonator is clamped at both ends and vibrates in the fundamental mode (Fig. 1), the active mass of the resonator is about half of the total static mass of the nanowire [1]. Quantum effects, for these devices, begin to influence their operation when the molecular scale is reached. This transition, into quantum dominated mechanics, is believed to occur when nanowires are a few nanometers in diameter [1]. However, small-diameter single-walled carbon nanotubes (CNTs), still obey continuum bending mechanics with only slight modifications [3].

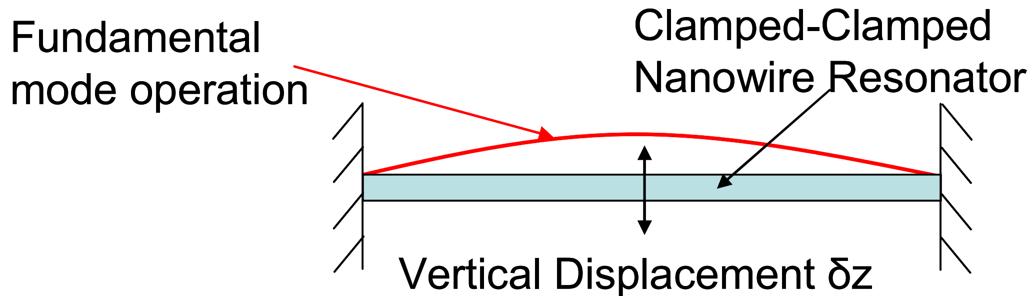

Figure 1. A clamped-clamped nanowire resonator operating in the fundamental bending mode.

In general, a small amount of power is required to drive bending-mode nanoelectromechanical systems (NEMS) [2], but sensing techniques for NEMS resonators are either electronically complex [4,5] or require cryogenic temperatures to minimize thermal noise sources which could mask the small signal generated by a NEMS resonator [1].

1.1.1 Resonant Mass Sensors

Nanowire resonators are ideally suited for mass sensing applications because of their small active mass. As predicted by eq. (1), if mass is added to a fundamental-mode nanowire resonator (Fig. 1) its resonant frequency decreases (Fig. 2). Recently, zeptogram mass sensors have been demonstrated at cryogenic temperatures using SiC NEMS resonators [6].

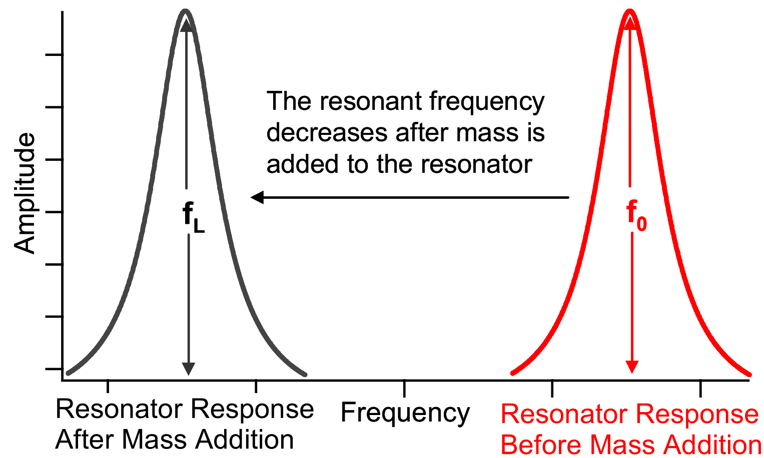

Figure 2. The red and grey traces represent the amplitude response of the unloaded and mass loaded NEMS resonator respectively ($f_L < f_0$).

1.1.2 NEMS Resonators for Frequency Domain Signal Processing and Nanomechanical Computation

High frequency and low-operating-power NEMS resonators are especially attractive for signal processing and nanomechanical computing applications [7]. High quality factor (high-Q) NEMS resonators are desired for frequency domain signal processing applications. Electrical signals which match the resonant frequency of high-Q NEMS resonators are easily distinguished from signals at slightly lower frequencies (Fig. 3). For low insertion loss NEMS resonators high-Qs are essential [1].

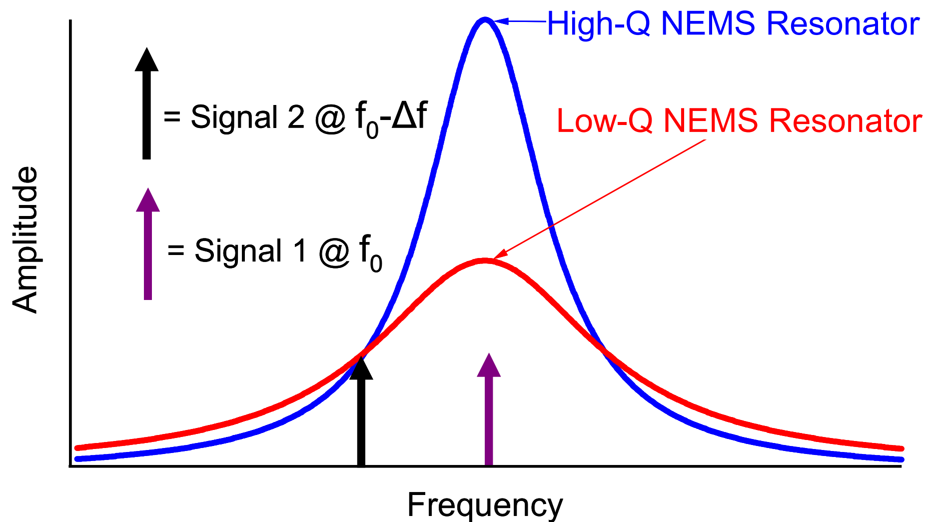

Figure 3. Frequency response comparison of a low-Q (red) and a high-Q (blue) NEMS resonator. The high-Q frequency response is better suited to discriminate between an electrical signal (signal 1) at the natural frequency of a NEMS resonator and a signal (signal 2) with a frequency slightly lower than the natural frequency of the NEMS device.

For nanomechanical computation applications, low-Q NEMS resonators may be required to prevent excessive ringing when transitioning between mechanical logic states and to achieve logic transition times on the order of $1/f_0$ [7]. However, a mechanical

XOR logic gate was recently demonstrated with high-Q GaAs cantilevers operating at their resonant frequencies (about 10 MHz), so low-Q NEMS resonators may not be absolutely necessary for nanomechanical computation [8].

To realize the full potential of NEMS based signal processing and computation systems simple low-power actuation and detection techniques should be developed to facilitate integration with complementary metal-oxide-semiconductor (CMOS) electronics. Progress has been made in this regard with the advent of GaAs piezoelectric NEMS logic gates [8]. DC bias voltages were not required to actuate or sense the cantilever resonators; however, the GaAs fabrication process used to create the devices was not suitable for monolithic integration with CMOS. Researchers have begun to investigate doped silicon NEMS resonators to create a new class of integrated systems in which a NEMS resonator would also serve as a mechanically active electronic device [21] in the same vein as the micro-scale vibrating gate transistor [22,23]. Field-effect transduced NEMS resonators would facilitate system integration.

1.2 Nanowires Mechanically Coupled to Resonant Microelectromechanical Systems (MEMS)

Researchers have integrated nanostructures with larger scale MEMS resonators to improve the performance of MEMS sensors [9,10]. MEMS bandpass filters can also benefit from nanostructure integration. Nanowire beams are the ideal elements to mechanically couple high-Q MEMS resonators due to their low stiffness and small mass. The stiffness of the coupling beam controls the frequency span between the resonant modes of a MEMS filter [11] (Fig. 3). As a result, future nanowire-coupled MEMS

filters can achieve smaller bandwidths and lower passband distortion or ripple [11,12,13] (Fig. 3).

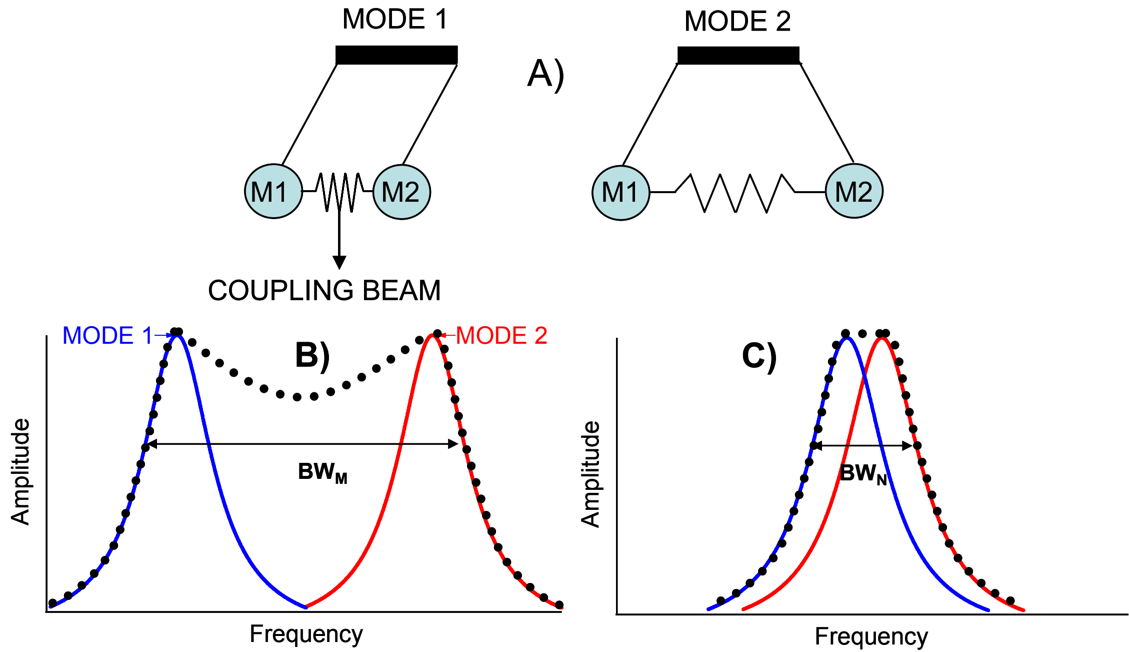

Figure 3. A) Two identical MEMS resonators, represented schematically as pendulums M1 and M2, are mechanically coupled with a beam (spring) to create a passband filter. Mode 1 and 2 are the in-phase and out-of-phase vibration modes of the coupled resonant system respectively. The bandwidth of the MEMS filter depends on the frequency span between the two modes. B) The passband filter characteristic (black dots) of the coupled system with microscale beams has a large bandwidth (BW_M). C) The filter bandwidth decreases ($BW_N < BW_M$) and has less passband distortion for the nanowire beam coupled MEMS filter.

Typical actuation techniques for NEMS resonators rely on forces that scale with surface area (electrostatic) [4,5] or length (magnetomotive) [6]. To avoid using excitation forces which do not scale favorably, NEMS resonators can be mechanically

actuated with coupled high-Q MEMS resonators [14]. Recently, surface acoustic wave (SAW) devices have been used to acoustically drive high-order bending modes of NEMS resonators and to study the effect of acoustic agitation on a two dimensional electron gas that was confined within a NEMS resonator [15].

1.3 Bottom-Up Vs. Top-Down Nanowires

The most popular bottom-up technique used to synthesize silicon nanowires is known as the Vapor-Liquid-Solid (VLS) process [16]. A metal catalyst, which forms a eutectic mixture with silicon, and a silicon vapor precursor are required for the VLS synthesis technique [17,18]. When catalyst particles with diameters above 20 nm are used to grow VLS nanowires, the preferred growth orientation lies along a <111> direction. For catalyst particles with diameters below 20 nm, VLS nanowires prefer the <110> or <112> direction [17]. Microfabricated structures have been used successfully as templates for lateral VLS nanowire growth [17,18,19]; however, absolute control over the location of nanowire attachment points to contact pads or MEMS structures has not yet been demonstrated. A new assembly technique was developed to create large arrays of nanowire resonators with harvested VLS nanowires, but the assembly process is still random resulting in missing or multiple nanowires at patterned nanowire trap sites [20].

Top-down nanowires are usually created using thin Silicon-on-Insulator (SOI) wafers. The thickness of the SOI device layer usually defines the height of the nanowires while the length and width of top-down nanowires are defined using nanoscale patterning techniques such as e-beam lithography. In contrast to VLS nanowires, the orientation of top-down nanowires can be arbitrarily chosen depending on the SOI wafer orientation. However, the width of top-down nanowires is limited by the minimum feature size

capabilities of the patterning technique used. Furthermore top-down nanowires generally have much rougher sidewall surfaces than VLS nanowires.

1.4 Dissertation Overview

Chapter 2 investigates the feasibility of using of silicon nanowires as flexural coupling beams tethering a pair of clamped-clamped MEMS resonators. The frequency response of the coupled system is tuned by varying the location of the nanowire attachment points along the length of the MEMS resonators. A focused-ion-beam tool is used to tune the frequency span between the two resonant modes of the coupled system by milling the nanowire coupler or depositing platinum on the top surface of the nanowire coupler.

Chapter 3 describes the top down fabrication process used to create the devices described in Chapters 2 and 4. Nitride anchor pillars are designed to suspend polysilicon electrodes above the MEMS and NEMS devices. An oxygen plasma is used to reduce the width of i-line defined features to create the silicon nanowires.

Chapter 4 introduces a new field-effect detection technique for silicon nanowire resonators. Polysilicon electrodes electrostatically actuate the nanowires while tuning the resistance of the nanowire as it displaces. This sensing technique is demonstrated using relatively low DC bias voltages. Finally, Chapter 5 concludes the dissertation with some thoughts on future research directions.

1.5 References

[1] M. L. Roukes, "Nanoelectromechanical Systems," *Technical Digest of the 2000 Solid-State Sensor and Actuator Workshop*, Hilton Head Island, SC, June 4-8, 2000, pp.1-10.

[2] K. L. Ekinci and M. L. Roukes, "Nanoelectromechanical systems," *Review of Scientific Instruments*, Vol. 76, 2005, article #061101.

[3] S. Govindjee and J. L. Sackman, "On the use of continuum mechanics to estimate the properties of nanotubes," *Solid State Communications*, Vol. 110, No.4, March 1999, pp.227-230.

[4] V. Sazonova, et al., "A tunable carbon nanotube electromechanical oscillator" *Nature*, Vol. 431, Sept. 2004, pp.284-287.

[5] H. B. Peng, et al., "Ultrahigh Frequency Nanotube Resonators," *Physical Review Letters*, Vol. 97, Aug. 2006, article# 087203.

[6] Y. T. Yang, C. Callegari, X. L. Feng, K. L. Ekinci, and M. L. Roukes, "Zeptogram-Scale Nanomechanical Mass Sensing," *Nano Letters*, Vol. 6, No. 4, Apr. 2006, pp.583-586.

[7] M. L. Roukes, "Mechanical Computation, Redux?," *Technical Digest of the IEEE International Electron Device Meeting*, Dec. 13-15, 2004, pp.539-542.

[8] S. C. Masmanidis, et al., "Multifunctional Nanomechanical Systems via Tunably Coupled Piezoelectric Actuation," *Science*, Vol. 317, Aug. 2007, pp.780-783.

[9] F. Torres, et al., “Coupling Resonant Micro and Nanocantilevers to Improve Mass Responsivity by Detectability Product,” *Proceedings of the 14th International Conference on Solid-State Sensors, Actuators and Microsystems* (*Transducers 2007*), Lyon, France, June 10-14, 2007, pp.237-240.

[10] S. Boussand and N. J. Tao, “Polymer Wire Chemical Sensor Using a Microfabricated Tuning Fork,” *Nano Letters*, Vol. 3, No. 8, 2003 pp.1173-1176.

[11] S.-S. Li, Y.-W. Lin, Z. Ren, and C. T.-C. Nguyen, “An MSI Micromechanical Differential Disk-Array Filter”, *Proceedings of the 14th International Conference on Solid-State Sensors, Actuators and Microsystems* (*Transducers 2007*), Lyon, France, June 10-14, 2007, pp.307-311.

[12] K. Wang, C. T.-C. Nguyen, “High-Order Medium Frequency Micromechanical Electronic Filters”, *IEEE Journal of Microelectromechanical Systems*, Vol. 8, 1999, pp.534-556.

[13] F. D. Bannon, J. R. Clark, and C. T.-C. Nguyen, “High-Q Microelectromechanical Filters”, *IEEE Journal of Solid-State Circuits*, Vol. 35, 2000, pp. 512-526.

[14] F. W. Beil, A. Wixforth, and R. H. Blick, “Investigation of nano-electromechanical-systems using surface acoustic waves,” *Physica E*, Vol. 13, 2002, pp.473-476.

[15] F. W. Beil, et al., “Shock Waves in Nanomechanical Resonators,” *Physical Review Letters*, Vol. 100, Jan. 2008, article # 026801.

[16] R.S. Wagner and W. C. Ellis, “Vapor-Liquid-Solid Mechanism of Single Crystal Growth,” *Applied Physics Letters*, Vol. 4, No. 5, March 1964, pp.89-90.

[17] R. He, *Silicon Nanowires for Nanoelectromechanical Systems*, University of California, Berkeley Ph.D. Dissertation Fall 2006.

[18] O. Englander, *Localized Synthesis, Assembly and Integration of Silicon Nanowires*, University of California, Berkeley Ph.D. Dissertation Fall 2005.

[19] A. San Paulo, et al., “Suspended Mechanical Structures Based on Elastic Silicon Nanowire Arrays,” *Nano Letters*, Vol. 7, No. 4, pp.1100-1104.

[20] M. Li, et al., “Bottom-up assembly of large-area nanowire resonator arrays,” *Nature Nanotechnology*, Vol. 3, Feb. 2008, pp.88-92.

[21] D. V. Scheible, H. Qin, H.-S. Kim, and R. H. Blick, “Fabrication of doped nano-electromechanical systems,” *Physica Status Solidi Rapid Research Letters*, Vol. 1, No. 5, Aug. 2007 pp.205-207.

[22] H. C. Nathanson, W. E. Newell, R. A. Wickstrom, and J. R. Davis, “The Resonant Gate Transistor,” *IEEE Transactions on Electron Devices*, Vol. ED-14, No. 3, March 1967 pp.117-133.

[23] N. Abele, et al., “Ultra-Low Voltage MEMS Resonator Based on RSG-MOSFET,” *Proceedings of the 19th IEEE International Conference on Micro Electro Mechanical Systems (MEMS 2006)*, Istanbul, Turkey Jan. 22-26 2006, pp.882-885.

Chapter 2. Silicon Nanowire Coupled MEMS Resonators

2.1 Introduction

Microscale flexural-mode beams have been used with great success as mechanical coupling springs tethering multiple resonators to create microelectromechanical systems suitable for filtering electrical signals in the frequency domain [1,2]. Microscale coupling beams play an important role in determining the bandwidth [1], stopband rejection [2] and passband distortion [3] of RF MEMS filters. State-of-the-art MEMS filters rely on medium scale integration of high-quality-factor (high-Q) resonators with extensional-mode microscale couplers, to avoid the use of submicron mechanical coupling beams, which would otherwise be required to generate small bandwidths at frequencies above 100 MHz [4]. In general the bandwidth BW of a mechanically coupled MEMS filter depends on the ratio of coupler stiffness to resonator stiffness:

$$BW \propto \left(\frac{k_{MC}}{k_R} \right) \quad (1)$$

where k_{MC} is the stiffness of a microscale coupler and k_R is the effective stiffness of a single coupled resonator.

To first order, the stiffness of a coupling beam depends on its physical dimensions. Reducing the cross-sectional area of a coupling beam decreases its stiffness resulting in a smaller bandwidth MEMS filter, as shown by Eq. (1). A scaled cross-section coupling beam also has a lower mass than an equivalent microscale coupler which, in theory, should minimize the passband distortion of a MEMS filter [3]. For these reasons, silicon nanowires are the ideal candidates to replace microscale coupling beams in MEMS filters due to their low stiffness and small mass.

This chapter investigates the feasibility of using silicon nanowires as mechanical coupling elements by attaching a silicon nanowire to a pair of clamped-clamped MEMS resonators. The work reported in this chapter constitutes an initial step towards the creation of nanowire-coupled MEMS filters and can potentially be adapted for sensing [5,6] or nanometrology applications.

2.2 Nanowire Coupled MEMS Resonators: Operation and Design

The nanowire coupled resonator system, which is similar in structure and operation to the MEMS filter described in [1], vibrates in two modes depicted in Fig. 1. Mechanical energy is transmitted from one clamped-clamped microresonator to an identical resonator via the silicon nanowire coupling beam. In the first mode, the MEMS beams vibrate in phase with each other (Fig. 1A), whereas in the second mode the beams vibrate out of phase (Fig. 1B). The device shown in Fig. 1 is referred to as a maximum velocity coupled system, since the nanowire coupler is attached to the maximum displacement points, or maximum velocity points, of both MEMS resonators. A low velocity coupled system was also designed where a nanowire was attached near the anchors of both clamped-clamped microresonators.

Figure 2 features two scanning electron micrographs (SEMs) of a fabricated maximum velocity coupled device (Fig. 2A) and a low velocity coupled device (Fig. 2B). The couplers and the MEMS resonators have the same height defined by the thickness of the silicon-on-insulator wafers used to create the coupled systems (275 nm). The MEMS resonators were 10 μm long and 3.1 μm wide. The nanowire couplers were 6.2 μm long and their widths varied from a minimum of 280 nm to a maximum of 500 nm.

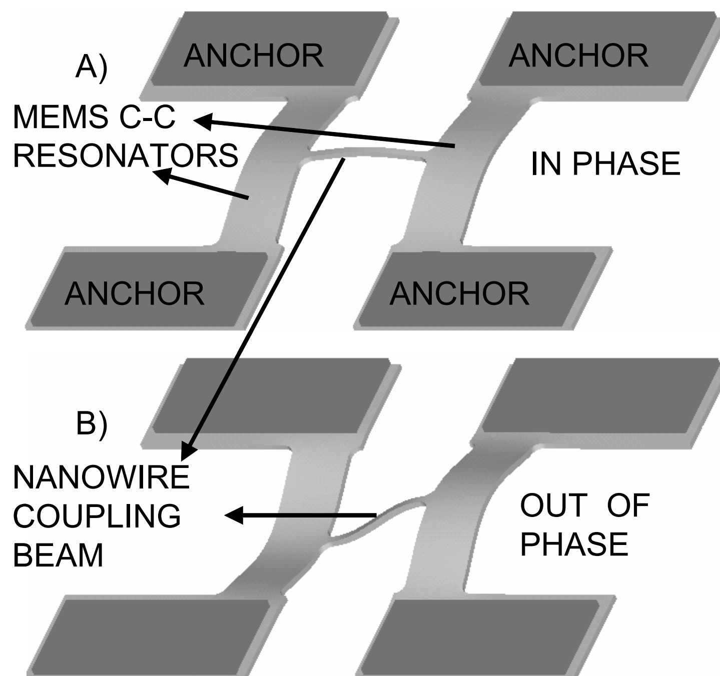

Figure 1. ANSYS mode simulations of a nanowire coupled clamped-clamped resonator system (maximum velocity coupled). A) In-phase vibration mode (Mode 1). B) Out-of-phase vibration mode (Mode 2).

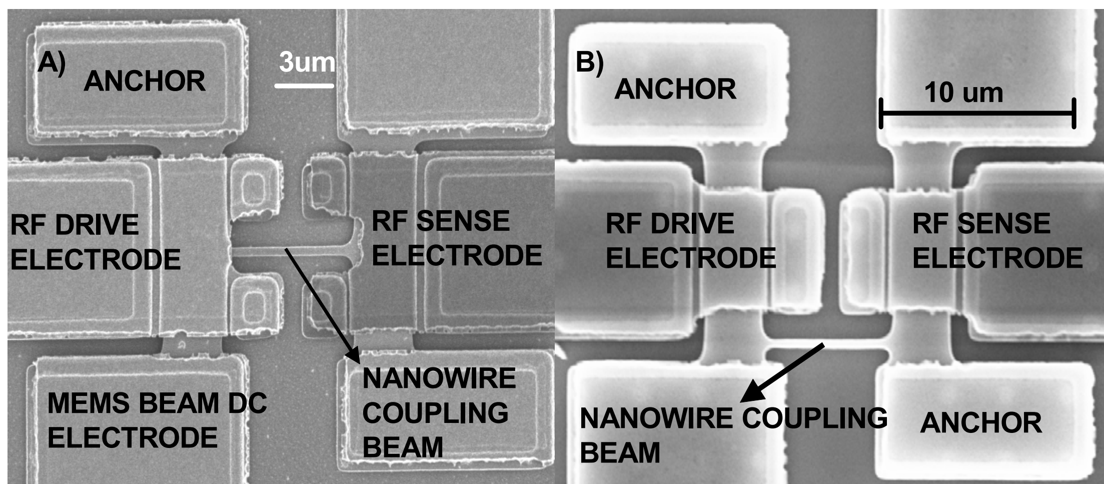

Figure 2. SEMs of fabricated nanowire coupled resonator systems. A) Maximum velocity coupled system (MVA). B) Low velocity coupled system (LVA). The polysilicon RF electrodes partially conceal the clamped-clamped MEMS resonators.

The MEMS clamped-clamped resonators were suspended 100 nm beneath polysilicon drive and sense electrodes (Fig. 3) to induce the out-of-plane resonator displacement depicted in Fig. 1. A pair of lateral electrostatic gaps were created, but did not contribute to the driving force applied to the system since they were balanced on each side of the MEMS resonators. The lateral gap on the right side of the resonator is not shown in Fig. 3.

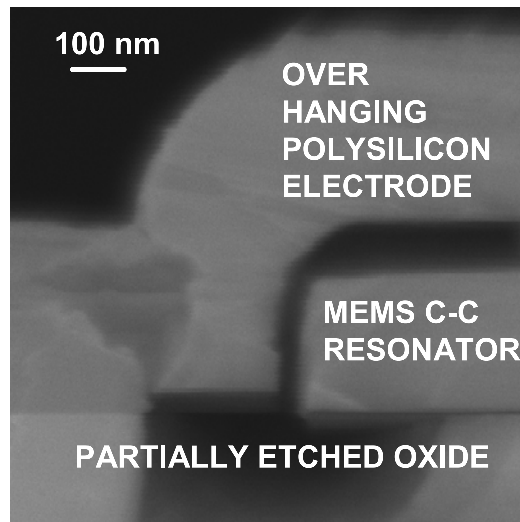

Figure 3. Cross-sectional SEM of a polysilicon electrode suspended above the single crystal device layer. The vertical gap is 100 nm and the lateral gap is 60 nm. The oxide was partially etched for better contrast. Single crystal silicon is 275 nm thick.

2.2.1 Flexural-Mode Nanowire Coupled System Theory

The ratio of the coupler stiffness to the effective stiffness of the microresonators determines the frequency span between the two resonant modes depicted in Fig. 2. Assuming both MEMS resonators are matched, the resonant frequency of a single MEMS clamped-clamped resonator is required to determine the stiffness of both the nanowire

coupler and the effective stiffness of the MEMS resonators. For a single clamped-clamped (C-C) beam the resonant frequency is given by:

$$f_0 = \frac{1.03 H_R}{L_R^2}\sqrt{\frac{E}{\rho}} \tag{2}$$

where H_R (275 nm) and L_R (10 μm) are the height and width of the C-C beam respectively, E is Young's modulus of (100) silicon (129 GPa), and ρ is the density of silicon 2330 kg/m^3. The mode shape of the C-C MEMS resonator is described by the modal displacement of the bending beam, ϕ, given by:

$$\phi = \sin\beta x - \sinh\beta x + \alpha(\cosh\beta x - \cos\beta x)\text{, where} \tag{3}$$

$$\alpha = \frac{\sinh\beta_n L_R - \sin\beta_n L_R}{\cosh\beta_n L_R - \cos\beta_n L_R} \tag{4}$$

with β_n = 4.73/L_R for the fundamental bending mode and x is the location along the L_R = 10 μm C-C beam (Fig. 4). The effective mass, m_{EFF} ,and the effective spring constant,

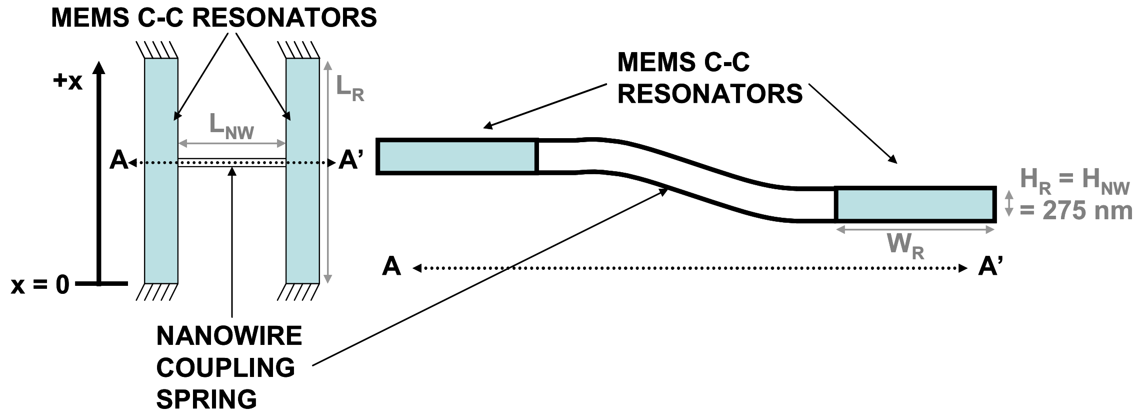

Figure 4. A cross-section view of the flexural-mode nanowire coupling the C-C MEMS resonators for the out-of-phase mode from Fig. 1B. Dimensions are highlighted with grey arrows.

k_{EFF}, of a fundamental mode beam at a given point x, along its length L_R, are given by [1,5]:

$$m_{EFF} = \frac{KE_{tot}}{\left(\frac{1}{2}\right)\dot{\phi}_X} = \rho W_R H_R \frac{\int_0^L \phi^2(x)dx}{\phi_X^2}, \text{ and} \quad (5)$$

$$k_{EFF} = (2\pi f_0)^2 m_{EFF} \quad (6)$$

where KE_{tot} is the kinetic energy of the bending beam, $\dot{\phi}_X$ is the modal velocity of the nanowire at particular point x along the length of the resonator, ϕ_X is the modal displacement of the nanowire at x, and W_R (3.1 μm) is the width of the C-C beam.

Quarter wavelength ($\lambda/4$) design rules were used to minimize mass loading contributions from the nanowire coupler to the MEMS resonators [1,5]. The stiffness of a quarter wavelength nanowire coupler, which vibrates in the flexural mode shown in Fig. 4, is given by [7]:

$$\alpha_C = L_{NW}\left(\frac{\rho W_{NW} H_{NW} (2\pi f_0)^2}{EI_{NW}}\right)^{0.25} \quad (7)$$

$$k_{NW} = \frac{EI_{NW}\alpha_C^3(\sin\alpha_C + \sinh\alpha_C)}{L_{NW}^3(\cos\alpha_C \cosh\alpha_C - 1)} \quad (8)$$

where L_{NW}, H_{NW} and W_{NW} are the length, height (275 nm) and width of the nanowire coupler respectively (see Fig. 4), the flexural rigidity of the nanowire is $I_{NW} = W_{NW}H_{NW}^3/12$, and f_0 is the resonant frequency of one C-C resonator assuming both MEMS resonators coupled by the nanowire are identical. For Eq. (8) to be valid L_{NW}, H_{NW} and W_{NW} must satisfy the quarter wavelength criteria [7]:

$$\sinh\alpha_C \cos\alpha_C + \cosh\alpha_C \sin\alpha_C = 0. \quad (9)$$

For a nanowire with W_{NW} = 400 nm and H_{NW} = 275 nm, the quarter wavelength coupler should be 5.5 μm long; however, to prevent the RF drive and sense electrodes from shorting, the nanowire was made 0.8 μm longer. The frequency span ΔF, or bandwidth BW, for a nanowire coupled system is estimated to be:

$$\Delta F = BW \approx \left(\frac{k_{NW}}{k_{EFF}} \right) f_0 . \qquad (10)$$

The frequency span between the two resonant modes can be tuned by fixing the nanowire coupler at different positions along the length of the C-C beam resonators because the stiffness of the MEMS resonators, k_{EFF}, varies along its length, Eqs. (3)-(6). Assuming equivalent nanowire couplers, maximum velocity coupled resonators should have a larger frequency span than low velocity coupled resonators. Another way to tune the frequency response of the coupled systems is to alter the stiffness of the nanowire coupler, Eqs. (7)-(10). Section 2.5 describes techniques which were used to alter the nanowire coupler stiffness.

2.3 Measurement Equipment and Testing Approach

The nanowire coupled resonators were tested in the Janis Research vacuum probe station shown in Fig. 5. The probe station was capable of reaching a minimum pressure of 1 mTorr with the aid of a turbo pump. When the RF testing first began five out of the six probes shown in the figure below were operational (GSG 1,2,4 and DC 1,2), probe GSG 3 had a damaged ground shield resulting in extremely noisy measurements so it was never used, see Fig. 5. On two separate occasions, two micromanipulation stages failed under vacuum while testing devices, damaging not only the devices but probes GSG 1 and DC 1 rendering them unusable.

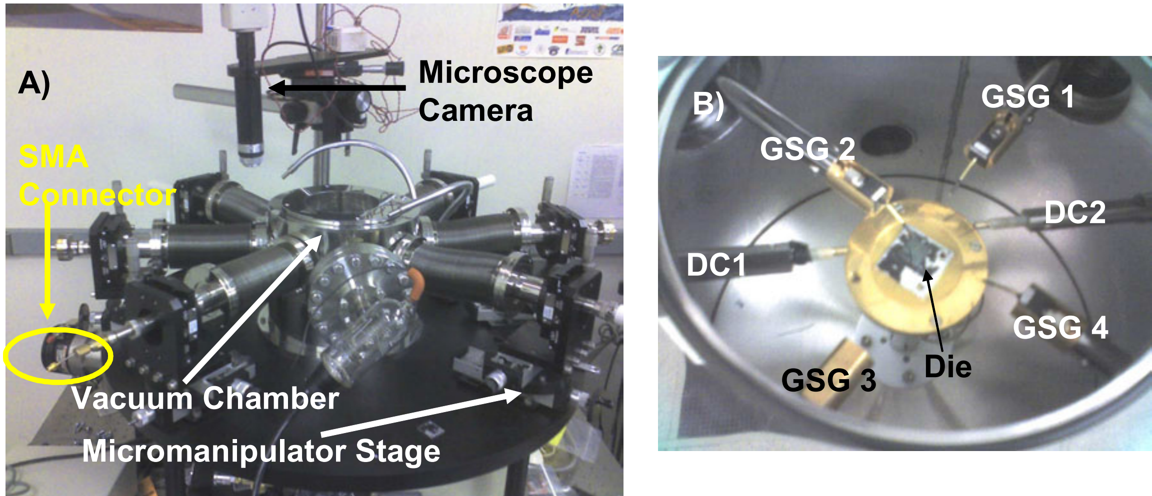

Figure 5. A) Picture of the Janis Research probe station used to test the coupled devices. B) Close up image of the vacuum chamber shown in A.

The nanowire coupled devices were tested in the two-port capacitive configuration depicted in Fig. 6. A single DC power supply was used to apply the bias voltage, V_P, to one C-C MEMS resonator which was shorted to the other resonator through the highly doped, $8X10^{18}/cm^3$ n-type, nanowire coupler. An Agilent Technologies E5071B Network Analyzer was used in the transmission measurement mode (S_{21}) to supply the RF forcing signal from port 1 to the RF drive electrode and detect the output RF signal directly from RF sense electrode at port 2. The measured signals were averaged 16 times and saved.

In the two-port configuration, parasitic capacitors create a RF feedthrough path directly coupling the drive and sense electrodes through the lightly doped handle wafer (Fig. 7). An attempt was made to reduce the feedthrough current by grounding the handle wafer near the device to partially divert the parasitic current; however, the attempt

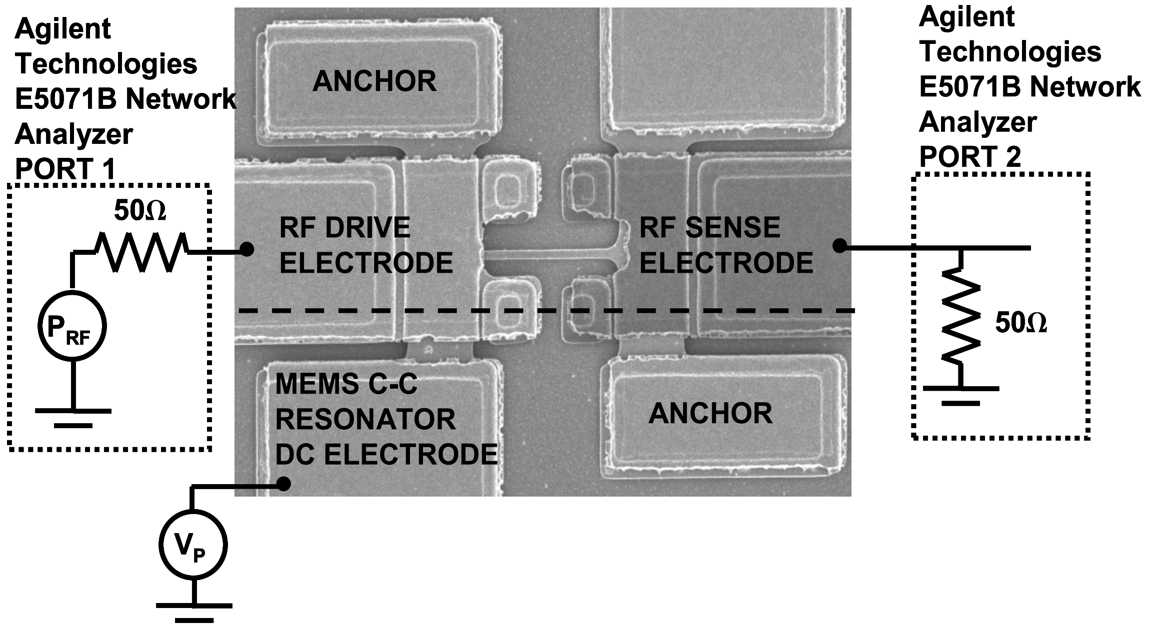

Figure 6. Two port capacitive configuration used to measure the transmission response (S_{21}) of the nanowire coupled systems.

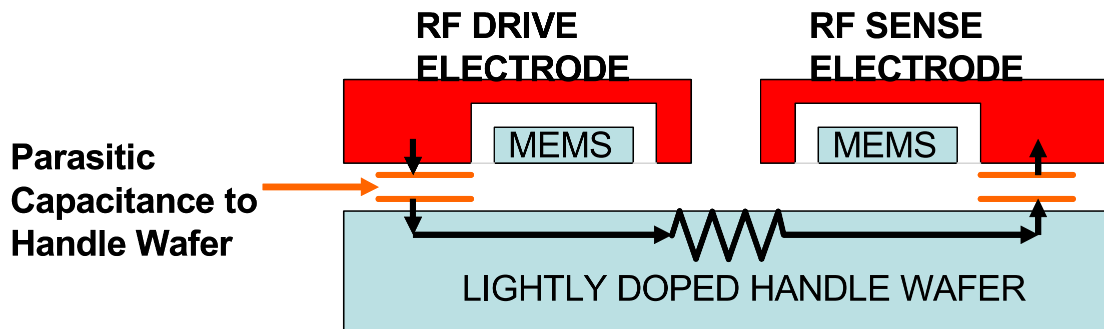

Figure 7. A cross-sectional schematic, taken at the dashed line in Fig. 6, that illustrates the parasitic capacitors which couple the drive and sense electrodes to the lightly doped handle wafer creating a RF feedthrough path represented by the black arrows.

failed to reduce the feedthrough signal. Typically, a highly doped wafer is used as a ground plane beneath MEMS resonators to divert the feedthrough signal away from the sense electrode because the resistance of a silicon substrate cannot be made large enough to effectively reduce the feedthrough current from the drive to sense electrode. It was determined that the large area contact pads of the device were responsible for the majority of the parasitic capacitance highlighted in Fig. 7 (see Sec. 2.4.1).

2.4 Measurement Results for Nanowire Coupled MEMS Resonators

The maximum velocity device shown in Fig. 2A, was tested using the two-port capacitive configuration from Fig. 6. The S_{21} transmission magnitude for the device, with (110) sidewalls referred to as MVA (Fig. 2A), is displayed in Fig. 8 at two bias voltages, V_P = 5.1V and V_P = 11.1V. In Fig. 8, the labels Mode 1 and Mode 2 correspond to the in-phase and out-of-phase resonant peaks respectively. Similar to [1] the parasitic capacitance creates dips in the transmission response before Mode 1 and after Mode 2. The frequency span, or bandwidth, for MVA was defined as the frequency range in between these two resonant peaks. The frequency span extracted from the data at 5.1V was 1.32 MHz and 1.30 MHz for 11.1V (a model for this device is given in Sec. 2.6).

The 3dB quality factor measured at 11.1V for the in-phase mode of MVA was 350, slightly larger than the quality factor measured, 270, for the out-of-phase mode. The coupler mass could be damping the response of the MEMS resonators, since the nanowire was attached to the maximum displacement points of both resonators. Anchor losses are also responsible for the low quality factors because the silicon nitride anchors of MEMS C-C resonators were attacked during the HF release (see Chapter 3). For the out-of-phase

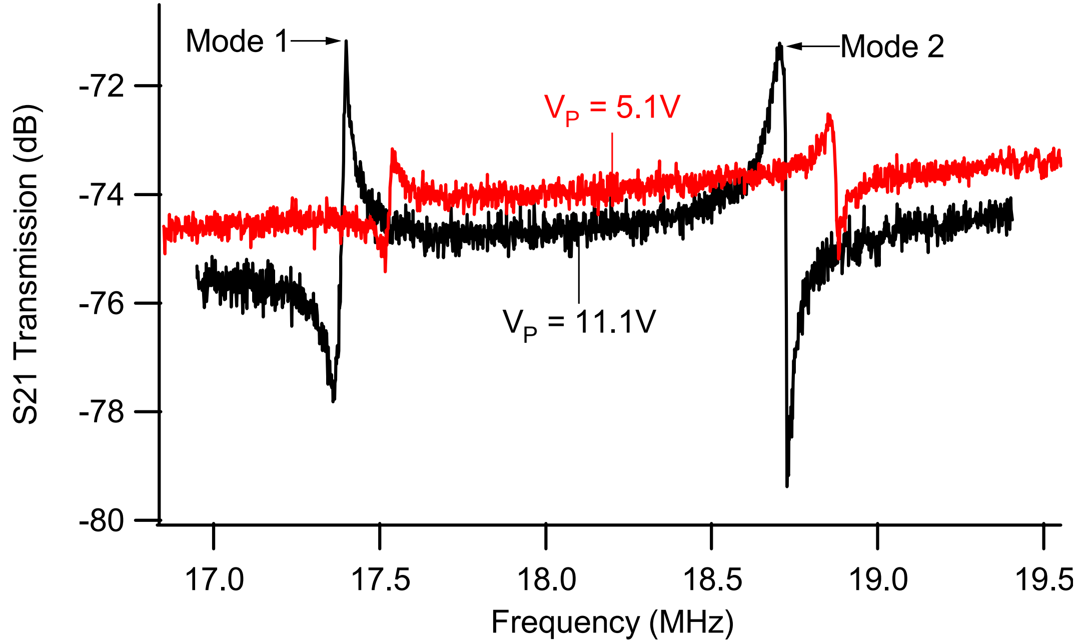

Figure 8. S_{21} transmission magnitude of device MVA with (110) sidewalls from Fig. 2A. P_{RF} = -10dBm with W_{NW} = 380 nm and L_{NW} = 6.2 μm for both traces.

mode, the MEMS resonators displace in opposite directions inducing an axial tension on the nanowire coupler, as shown in Fig. 1B and Fig. 4, also contributing to the lower quality factor of Mode 2.

A (100) oriented maximum velocity system with a 470 nm wide nanowire was tested (see Fig. 9). The S_{21} transmission magnitude for this device is depicted in Fig. 10. The resonant frequencies of both modes were lower than the corresponding peaks of device MVA, demonstrating the dependence of the frequency on the MEMS C-C resonator and nanowire orientation. Devices aligned with the wafer flat (110) are stiffer than devices aligned to the (100) plane. The frequency span for the (100) oriented device (Fig. 10) was 1.35 MHz at 8V and 1.45 MHz at 10V resulting in a large (100 kHz) span variation over a bias voltage range of 3V compared to the lower frequency span variation

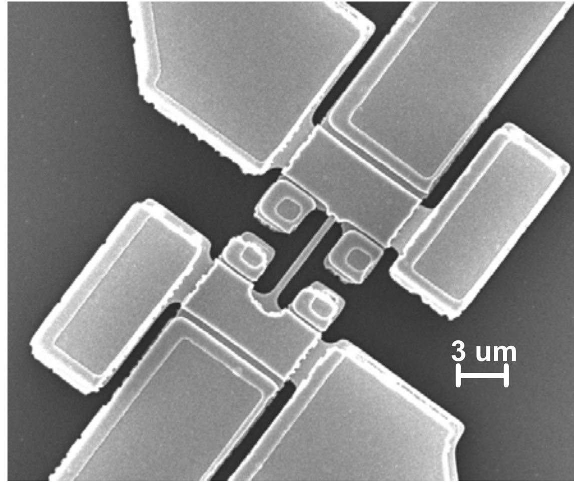

Figure 9. Maximum velocity coupled system with (100) sidewalls. The nanowire coupler was 470 nm wide and 6.2 μm long. The corresponding S_{21} transmission response is given in Fig. 8.

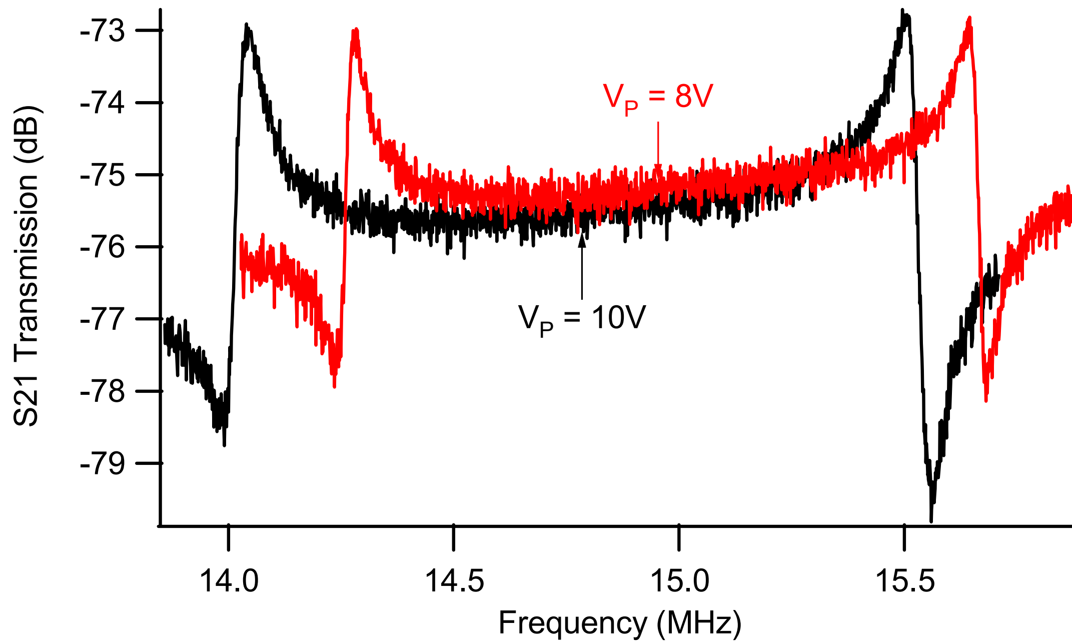

Figure 10. S_{21} transmission magnitude of device from Fig. 10 with (100) sidewalls. P_{RF} = -10dBm with W_{NW} = 470 nm and L_{NW} = 6.2 μm for both traces.

of MVA (20 kHz over a bias voltage range of 6V). The device shown in Fig. 10 was tested up to 10V so the quality factors of both peaks could not be extracted using the 3dB criteria used for MVA.

Figure 11 is the S_{21} transmission magnitude of the low velocity coupled device from Fig. 2B with (110) sidewalls, labeled here as LVA. In contrast to the maximum velocity coupled devices, the frequency span between the two resonant peaks of LVA was much smaller since the nanowire coupler was attached to stiffer regions of both MEMS resonators. It is more appropriate to equate the frequency span for this device to its 3dB bandwidth since LVA behaves more like a bandpass filter than did the maximum velocity coupled devices. The bandwidth was tuned using electrostatic springs coupling the drive and sense electrodes to the MEMS C-C resonators (Fig. 11). The electrostatic

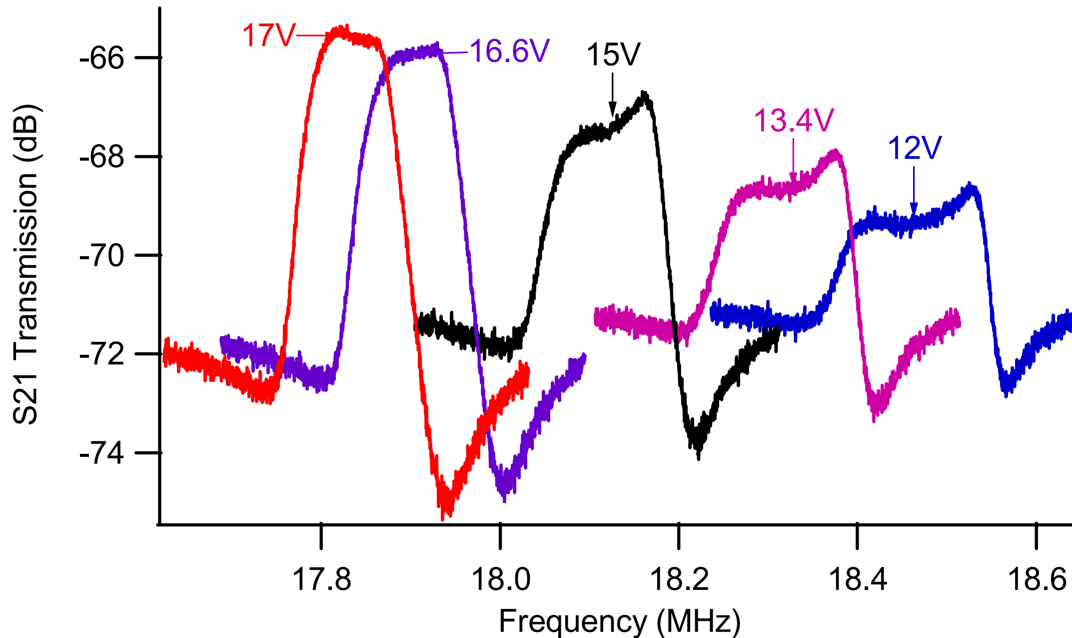

Figure 11. S_{21} transmission magnitude of device LVA with (110) sidewalls from Fig. 2B. P_{RF} = -11dBm with W_{NW} = 340 nm and L_{NW} = 6.2 μm for all traces shown.

springs compensated for resonant frequency differences between the two microresonators caused by variations in anchor stiffness and fabrication variations in resonator dimensions. The 3dB bandwidth for the device was 150 kHz at 15V and 110 kHz at 17V. Notches in the transmission magnitude appear before and after the pass band of LVA due to the parasitic capacitances, similar to the filter from [1].

The input RF power to LVA was varied while maintaining a constant DC bias of 17V to observe changes in the S_{21} transmission magnitude and phase responses (Fig. 12). Aside from the more noisy traces recorded at -25dBm, the shape of the passband changed and the 3dB bandwidth increased to 130 kHz (Fig. 12A). In contrast to the magnitude, two peaks were visible for the S_{21} phase response of LVA (Fig. 12B). The left and right phase peaks in Fig. 12B correspond to Mode 1 and Mode 2 respectively. The phase response shows similar nonlinear behavior for LVA at P_{RF} = -11dBm and -25dBm. Nonlinear operation of MEMS filters can increase the insertion loss of a MEMS filter [2]. This is one reason why linear bulk-mode resonators are currently used in state-of-the-art MEMS filters [4].

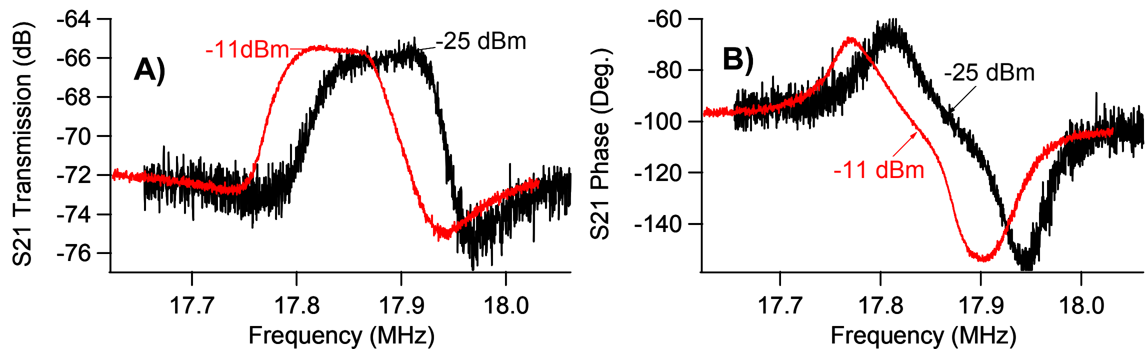

Figure 12. A) LVA S_{21} transmission magnitude and B) S_{21} transmission phase at 17V with P_{RF} = -11dBm or P_{RF} = -25dBm.

2.4.1 Contact Pad Parasitic Capacitance

As discussed in Section 2.3, parasitic capacitances create an RF conduction path from the drive electrode to the sense electrode. One maximum velocity device was accidentally damaged while the device was tested, severing one polysilicon electrode from its contact pad (Fig. 13). Originally the damage was limited to the area highlighted in red (Fig. 13), however, more damage was created left of the red oval when a GSG probe was placed directly onto the polysilicon lead in an attempt to continue testing the device. The measurement results, after the contact pad was severed, are shown in Fig. 14. Before it was damaged the feedthrough level was -75 dB, similar to MVA and the device shown in Fig. 10. The feedthrough dropped by 15dB to -90dB after it was damaged, effectively bypassing the parasitic capacitance contribution from the severed

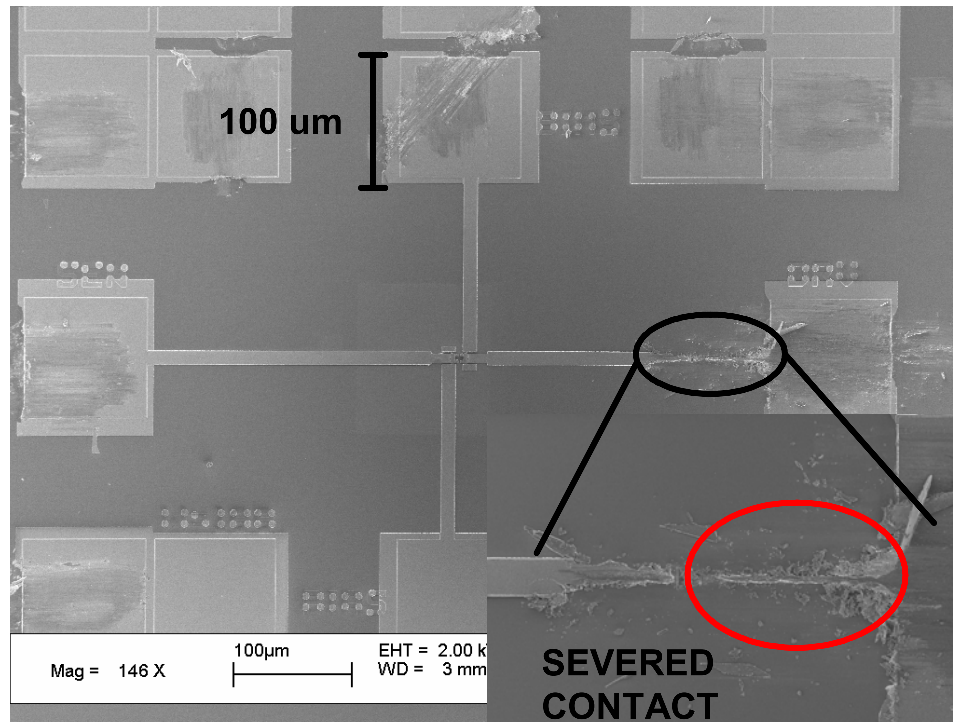

Figure 13. SEM of a (110) oriented maximum velocity coupled device with a polysilicon electrode severed from its contact 100 X 100 μm^2 contact pad.

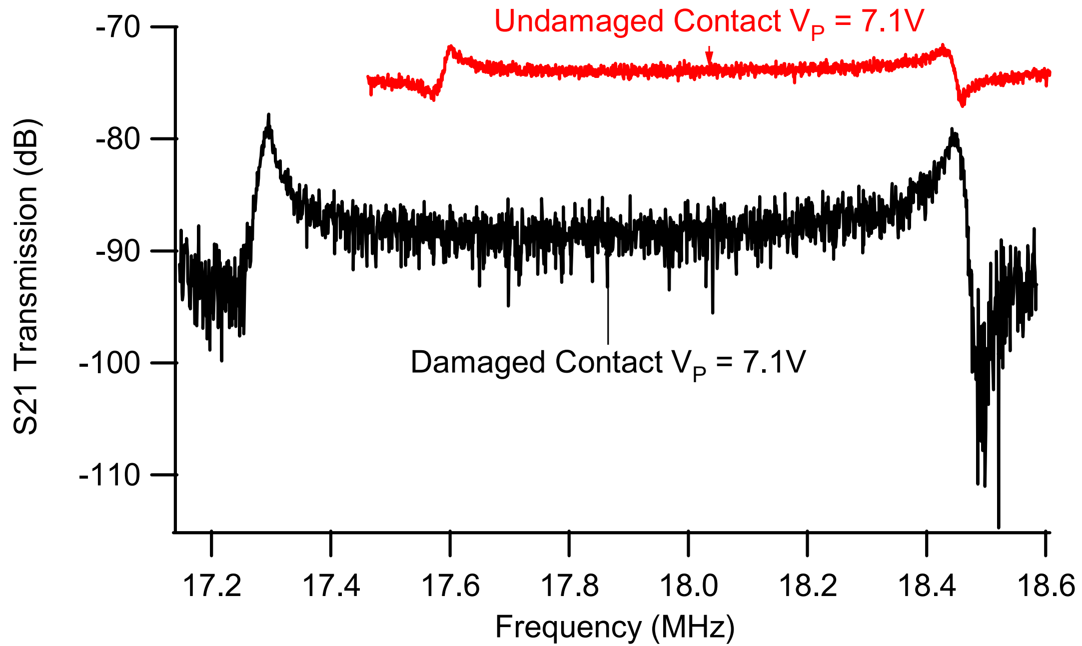

Figure 14. S_{21} transmission magnitude of the device shown in Fig. 13 before (red) and after (black) the polysilicon electrode was severed from the contact pad. The bias voltage was 7.1V and P_{RF} = -14dBm for both traces.

contact pad. This result confirmed the relationship between the capacitance of the large area contact pads and the large feedthrough levels measured for the devices from the previous section. Notches in the frequency response of the damaged device were still visible because all the parasitics were not completely eliminated from the system (black trace in Fig. 14). The red trace in Fig. 14 had a smaller frequency span than the black trace because the stiffness of the nanowire coupler was tuned before the device was damaged (this frequency span tuning technique is discussed in Sec. 2.5.2).

2.5 Coupled System Tuning

Individual maximum velocity and low velocity coupled devices were tuned by altering the stiffness of the nanowire coupler. A Gallium based Focused-Ion-Beam (FIB)

tool at the Stanford Nanocharacteriation Laboratory (SNL) was used to either remove material from the silicon nanowire coupler to decrease its stiffness or deposit Pt on the top surface of the nanowire coupler to increase the coupler stiffness. A fluorocarbon-based self assembled monolayer (SAM) was deposited on one device which increased the stiffness of the nanowire coupler resulting in a larger frequency span between the two resonant modes of the system. Finally, a thin film of high stress SiC was deposited on two released maximum velocity systems to increase the stiffness of nanowire couplers and the MEMS resonators.

2.5.1 FIB Nanowire Trimming

The FIB trimming technique, used to tune the frequency response of the coupled devices, was inspired by the FIB trimming work demonstrated on a polymer nanowire based vapor sensor [5]. In the work described here, the FIB was used to remove silicon from the nanowire coupler to decrease the frequency span between the in-phase and out-of-phase resonant modes of the coupled systems. Device MVA was the first device to undergo the trimming process, so low Ga ion currents were used to minimize damage to the nanowire. As a consequence, the nanowire was not completely trimmed near the FIB termination points because of the short exposure to low Ga ion currents (10 pA), Fig. 15B. Figure 15 shows the nanowire coupler before the nanowire of MVA was trimmed (A) and after the coupler was trimmed to a width of 232 nm (B). Figure 16 compares the S_{21} transmission magnitude for MVA with the original 380 nm wide coupler (black) and the trimmed 232 nm wide (grey) coupler. The frequency span for MVA decreased from 1.30 MHz to 0.85 MHz at a DC bias voltage of 11.1V and P_{RF} = -10dBm .

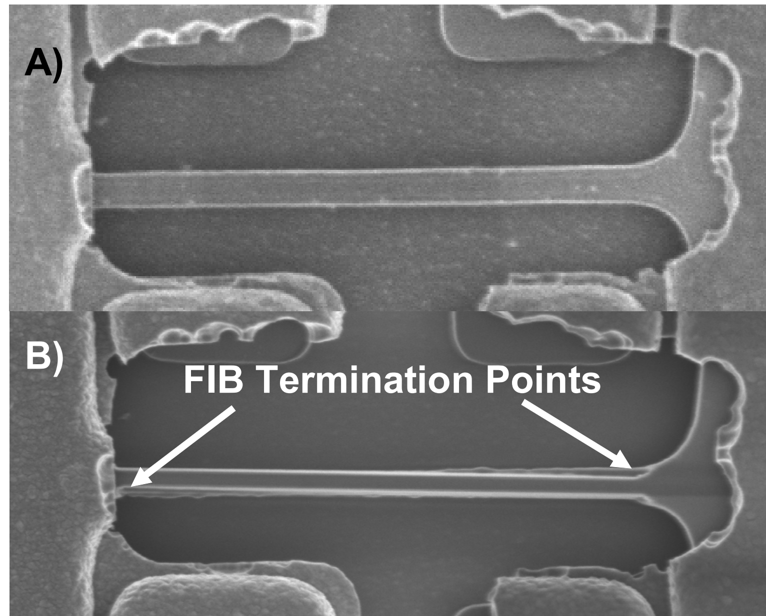

Figure 15. A) SEM of MVA nanowire coupler as fabricated W_{NW} = 380 nm). B) SEM of MVA nanowire coupler after FIB trim W_{NW} = 232 nm.

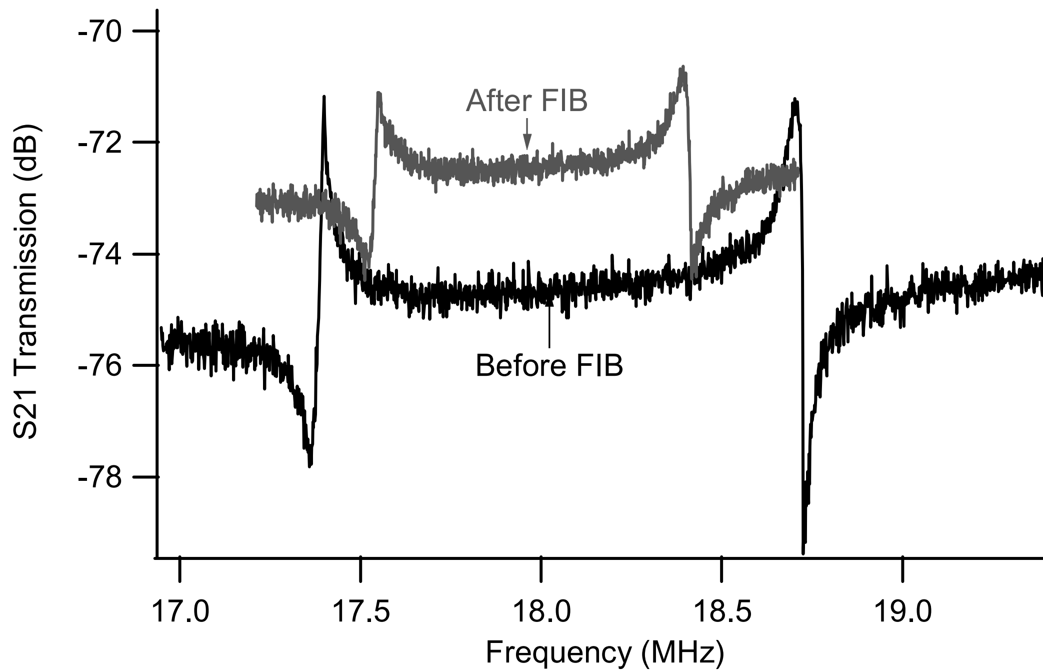

Figure 16. Frequency response of MVA at 11.1V and -10dBm. The black trace represents the 380nm wide nanowire and the grey trace represents the 232nm wide nanowire.

More aggressive cuts were made to push the limits of achievable nanowire widths by increasing the mill time at 10 pA Ga ion currents. However, the nanowires began to buckle at widths below 200 nm. Nanowire tethers, supporting a larger width island, were created to prevent the nanowires from buckling. In addition to the more aggressive trimming process, the FIB was used to create release holes in the polysilicon electrodes to decrease the time the nitride anchors were exposed to HF during the release process. The FIB release holes and sub 200 nm wide nanowire tethers were demonstrated on a device which was oriented parallel to the (100) plane (Fig. 17).

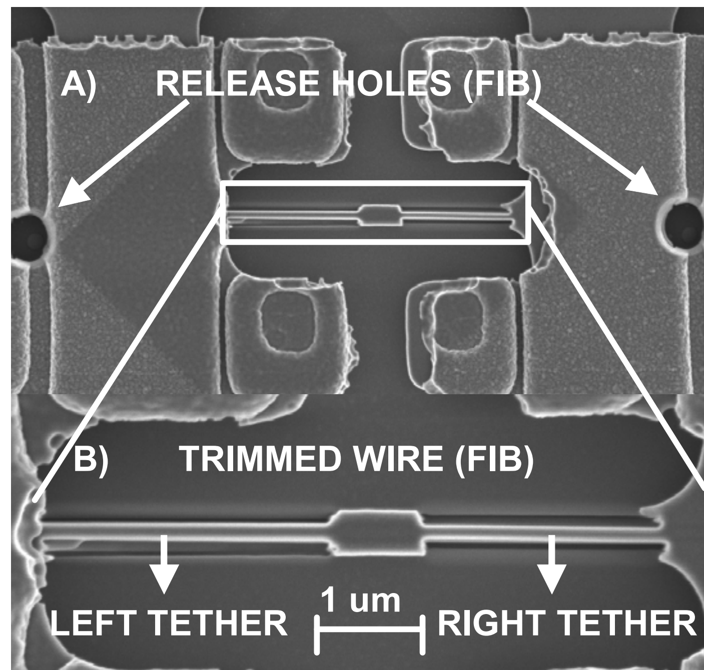

Figure 17. SEM of an aggressively trimmed device oriented parallel to (100). A) 1 μm diameter FIB machined release holes. B) Close up of FIB trimmed wire, the island was 1 μm long (L_{IS}) and 460 nm wide (original wire width), the left nanowire tether was 180 nm wide and 2.8 μm long (L_{LT}), the right nanowire tether is 160 nm wide and 2.6 μm long (L_{RT}).

Figure 18 highlights the change in the frequency response of the aggressively trimmed device, shown in Fig. 17, before (black) and after (grey) the nanowire was trimmed with the FIB. The release holes, milled into the polysilicon electrodes, minimized nitride anchor etching during the HF release process resulting in stiffer MEMS resonators and ultimately higher frequencies for Modes 1 and 2 (Fig. 18 black trace) relative to (100) oriented device shown in Fig. 10 from Sec. 2.4. After the nanowire coupler was trimmed the frequency span between the two resonant modes decreased from 1.45 MHz to 0.77 MHz (Fig. 18) for the device depicted in Fig. 17.

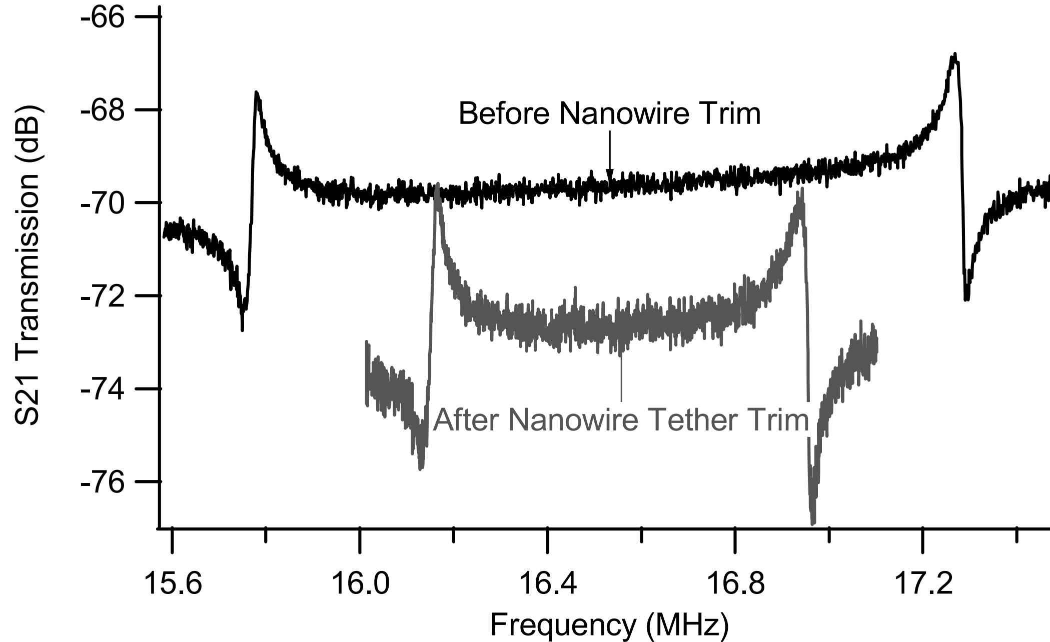

Figure 18. Frequency response of the device shown in Fig. 17 at 7V and -14dBm. Before the tethers were created with the FIB the nanowire was 460 nm wide and 6.2 μm long (black trace). After the nanowire tethers were milled the frequency span decreased (grey trace).

A 6 μm long segment of the nanowire coupler from device LVA was trimmed from a width of 340 nm to 260 nm (Fig. 19). The 3dB bandwidth of the low velocity coupled filter decreased from 130 kHz at 17V and P_{RF} = -25dBm (Fig. 12A) to 60 kHz at 8.8V and P_{RF} = -24dBm (see purple traces of Fig. 20). At a bias voltage of 5V and a RF input power of -11dBm the S_{21} transmission magnitude and phase were both nonlinear (black traces of Fig. 20). By decreasing the input RF power to -24dBm LVA operated as a linear filter (purple and red traces in Fig. 20). As the applied bias voltage was increased to tune the filter response, the 3dB bandwidth increased unlike the nonlinear filter response recorded for LVA before the nanowire was trimmed (Fig. 11). The data for the trimmed and untrimmed couplers indicate that the 340 nm wide, untrimmed, coupler damped the frequency response of LVA. Lower bias voltages and lower signal power were required to achieve the 3dB filter response of LVA after the nanowire was trimmed.

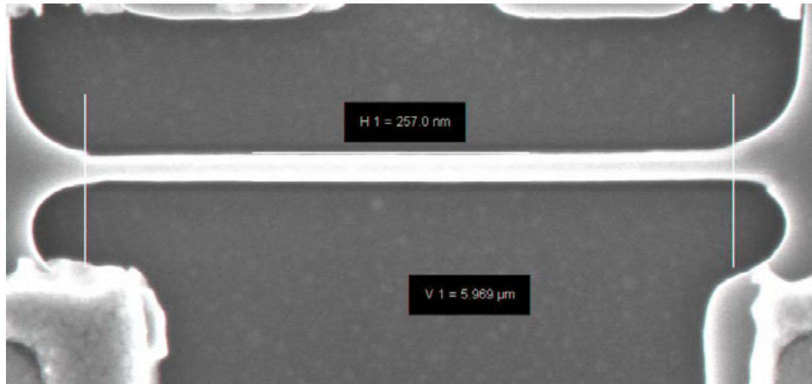

Figure 19. SEM of the FIB trimmed nanowire coupler of device LVA with W_{NW} = 260 nm and L_{NW} = 6 μm.

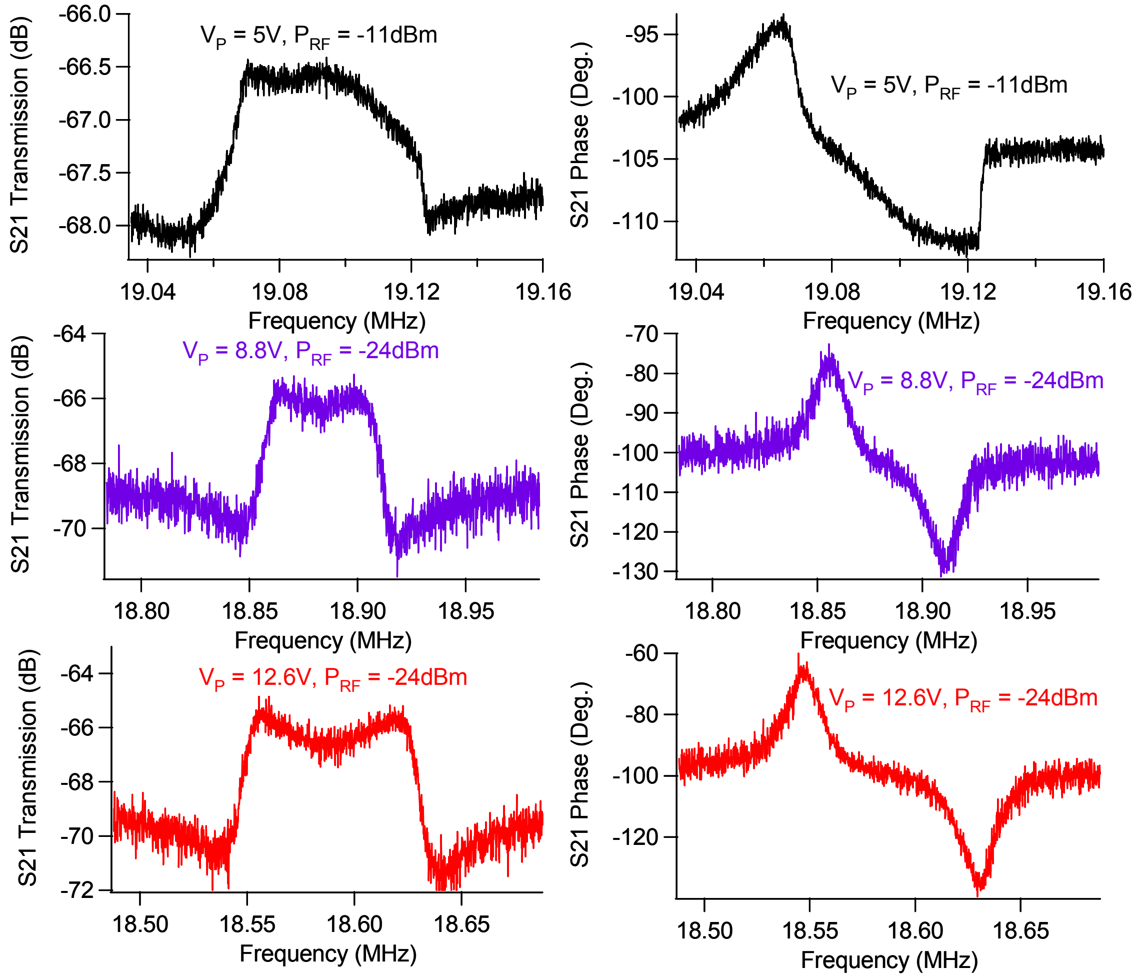

Figure 20. S_{21} transmission response of LVA after the nanowire was trimmed with the focused ion beam. V_P = 5V and P_{RF} = -11dBm (Black), V_P = 8.8V and P_{RF} = -24dBm (Purple), and V_P = 5V and P_{RF} = -24dBm (Red).

2.5.2 FIB Pt Deposition on Nanowire Coupler

The FIB tool at the SNL is equipped with a metal organic Pt gas precursor which is used to selectively deposit Pt films where the ion beam scans the sample surface. Before the polysilicon electrode was accidentally damaged on the device shown in Fig. 13, the 480 nm wide coupler was trimmed (Fig. 21) and a 40 nm thick Pt film was

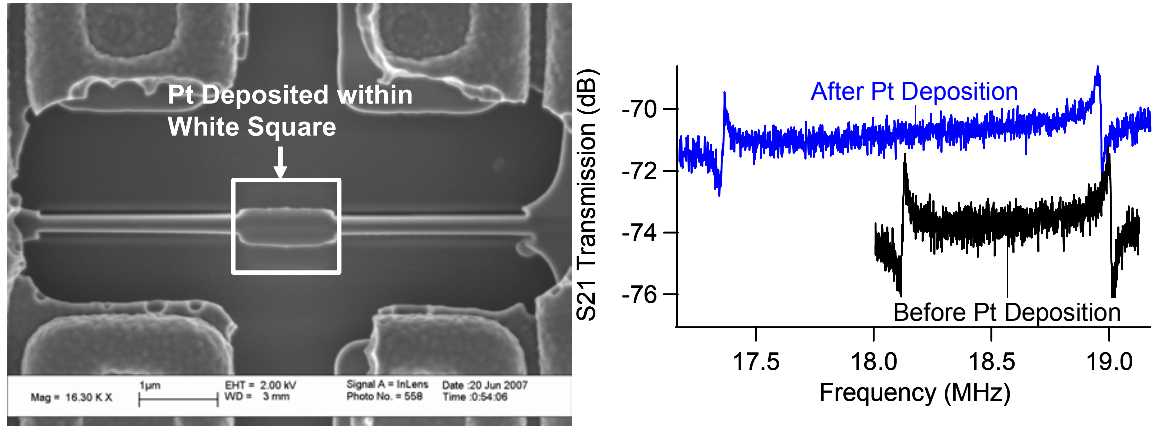

Figure 21. SEM of the nanowire coupler from the device shown in Fig. 13 with Pt deposited on top of the island. The left tether was 210 nm wide and the right tether was 225 nm wide. The S_{21} transimission magnitude was measured at 4.7V with an input RF power of -17dBm.

deposited on the top surface of the 1.3 μm long and 480 nm wide island. The Pt film increased the stiffness of the trimmed nanowire coupler (Figs. 21 and 14), primarily shifting the resonant peak of Mode 1 to a lower frequency. The frequency span of the device before Pt deposition was 0.87 MHz and increased to 1.58 MHz after the Pt was deposited on the island (Fig. 21). Two mechanisms are thought to be responsible for the increase in coupler stiffness: 1) the thermal expansion coefficient difference between the Pt and the silicon nanowire generated a stress on the nanowire coupler and 2) the effective rigidity $(EI)_{EFF}$ of the nanowire coupler was increased due to the larger Young's modulus of Pt and the thickness of the Pt film [8].

The experiment was repeated on another maximum velocity coupled device. In this case a 15 nm thick film of Pt was deposited along the length of the nanowire coupling the device shown in Fig. 22. The frequency span, of the device shown in Fig.

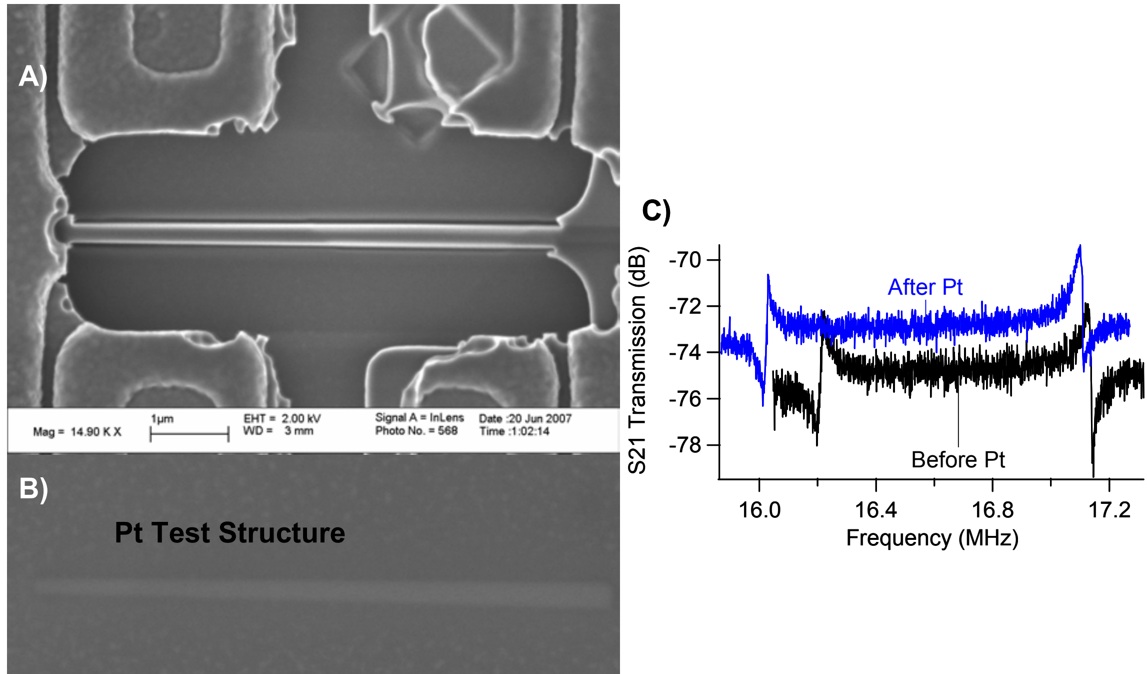

Figure 22. A) SEM of nanowire coupler of a (100) device. B) Pt was deposited along the length of the wire from A) with the exact dimensions of a Pt test structure deposited near the device. AFM scans were performed on the test structure to determine the thickness of the deposited Pt. C) S_{21} transmission magnitude of MVE before and after Pt deposition V_P = 5V and P_{RF} = -17dBm

22A, increased from 0.91 MHz, before the Pt was deposited, to 1.07 MHz after Pt deposition (Fig. 22C). Similar to the maximum velocity coupled device shown in Fig. 21, Mode 1 experienced a larger shift in resonant frequency compared to Mode 2. The deposited Pt film seems to affect the coupler bending motion associated with Mode 1 (Fig.1A), which is similar to the bending motion of a clamped-clamped beam. Mode 2 seems to be less susceptible to the Pt film since the center of the nanowire coupler does not displace or bend (Fig. 4).

2.5.3 Frequency Span Tuning with a Self Assembled Monolayer (SAM)

The Applied MicroStructure molecular vapor tool in the Microlab was used to deposit a 1H, 1H, 2H, 2H-Perfluorooctyltrichlorosilane (FOTS) SAM (Fig. 23) on device MVA after the nanowire was trimmed with the FIB (Figs. 2A and 15). OH-terminated silicon surfaces were created by the AMST tool with a five minute O_2 plasma treatment to facilitate SAM deposition. A dummy piece of silicon was placed in the AMST chamber, along with MVA, to measure the water contact angle of the deposited FOTS SAM (109° near the typical 110° estimated for the process). The FOTS SAM deposits on all surfaces oxide coated surfaces including the nanowire coupler, whereas the Pt was only deposited on the top nanowire surface. MVA was tested immediately after SAM deposition (Fig. 24A) at 11.1V and -10dBm. The SAM was then stripped with a ten minute UV O_3 treatment and tested once more (Fig. 24B).

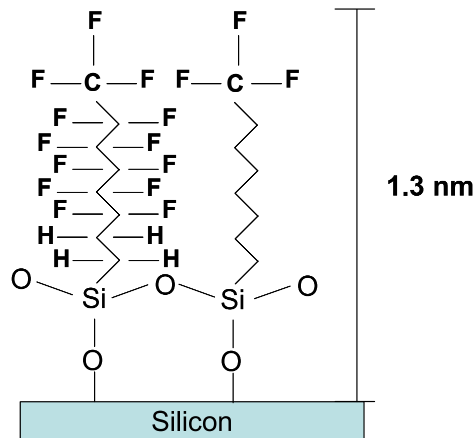

Figure 23. General structure of the FOTS SAM. F is a fluorine atom and H is a hydrogen atom. Each kink in the chain on the left hand side above the Si atom corresponds to a carbon atom. The chain on the right side of the figure is the short hand representation of the structure. The Silicon surface must be OH terminated in order to deposit the vapor phase SAM.

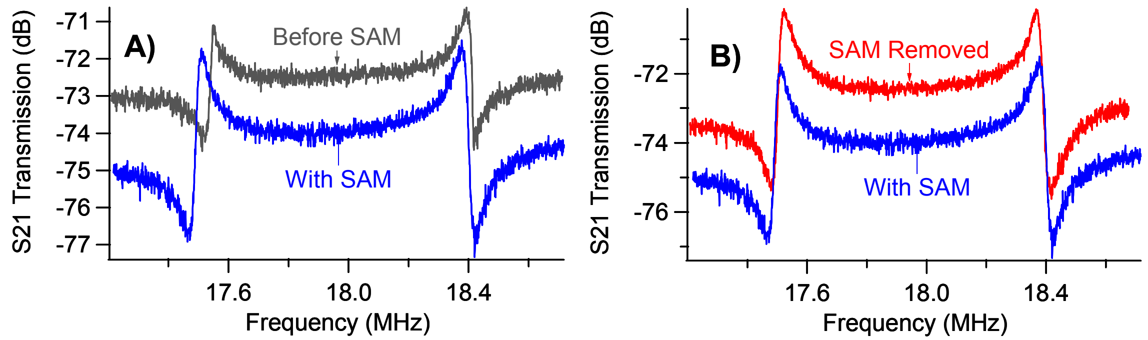

Figure 24. A) Comparison of MVA S_{21} transmission magnitude before SAM deposition (grey) and after SAM deposition (blue). B) Comparison of MVA S_{21} transmission magnitude with the SAM coating (blue), same as Fig. 23A, and after the SAM was removed (red).

In Fig. 24A, the frequency span increased from 0.85 MHz to 0.87 MHz upon SAM deposition. The O-Si-O bonds and the bulky CF_3 end groups (Fig. 23) are thought to hinder the bending motion of the nanowire for both resonant modes increasing the effective stiffness of the nanowire coupler. Not only did the frequency span increase after the SAM was deposited but both resonant peaks shifted to lower frequencies (Fig. 24A). The shift in center frequency may be the result of a oxide created on the nitride anchors during theO_2 plasma step, which slightly decreased the stiffness of the MEMS C-C resonators.

UV O_3 attacks the carbon atoms of the SAM leaving behind the O-Si-O bonds on the silicon surface. After the SAM was removed, the span decreased from 0.87 MHz back to the original span of 0.85 MHz (Fig. 24B).

The frequency span of MVA was measured at different bias voltages before SAM deposition (Table 1), after SAM deposition (Table 2) and after SAM removal (Table 3) to

add statistical significance to the SAM measurements of Fig. 24. The input RF power was held constant at -10dBm for all the data in Tables 1-3. The extracted frequency span was relatively stable for all three cases (before SAM, with SAM, and after SAM removal).

Bias Voltage (V)	Mode 1 (MHz)	Mode 2 (MHz)	**Span (MHz)**
8.5	17.67	18.52	**0.85**
9	17.65	18.5	**0.85**
9.5	17.62	18.46	**0.84**
10	17.58	18.43	**0.85**
10.5	17.56	18.4	**0.84**
11	17.55	18.4	**0.85**
11.1	17.55	18.39	**0.84**
11.5	17.53	18.38	**0.85**
12	17.51	18.35	**0.84**

Table 1. MVA data before SAM deposition. The column labeled Mode 1 refers to the resonant frequency of Mode 1. Span = Mode 2 – Mode 1. The average span was 0.85 MHz and the standard deviation was 5 kHz.

Bias Voltage (V)	Mode 1 (MHz)	Mode 2 (MHz)	**Span (MHz)**
8.6	17.59	18.47	**0.88**
9	17.59	18.46	**0.87**
9.5	17.57	18.45	**0.88**
10	17.56	18.43	**0.87**
11.1	17.51	18.38	**0.87**

Table 2. MVA data after SAM was deposited. The average span was 0.87 MHz and the standard deviation was 6 kHz.

Bias Voltage (V)	Mode 1 (MHz)	Mode 2 (MHz)	**Span (MHz)**
9	17.63	18.48	**0.85**
9.5	17.6	18.46	**0.86**
10.1	17.57	18.42	**0.85**
10.5	17.55	18.4	**0.85**
11.1	17.52	18.37	**0.85**

Table 3. MVA data after the SAM was removed with UV O_3 . The average span was 0.85 MHz and the standard deviation was 5 kHz.

2.5.4 Frequency Span Tuning with High Stress SiC

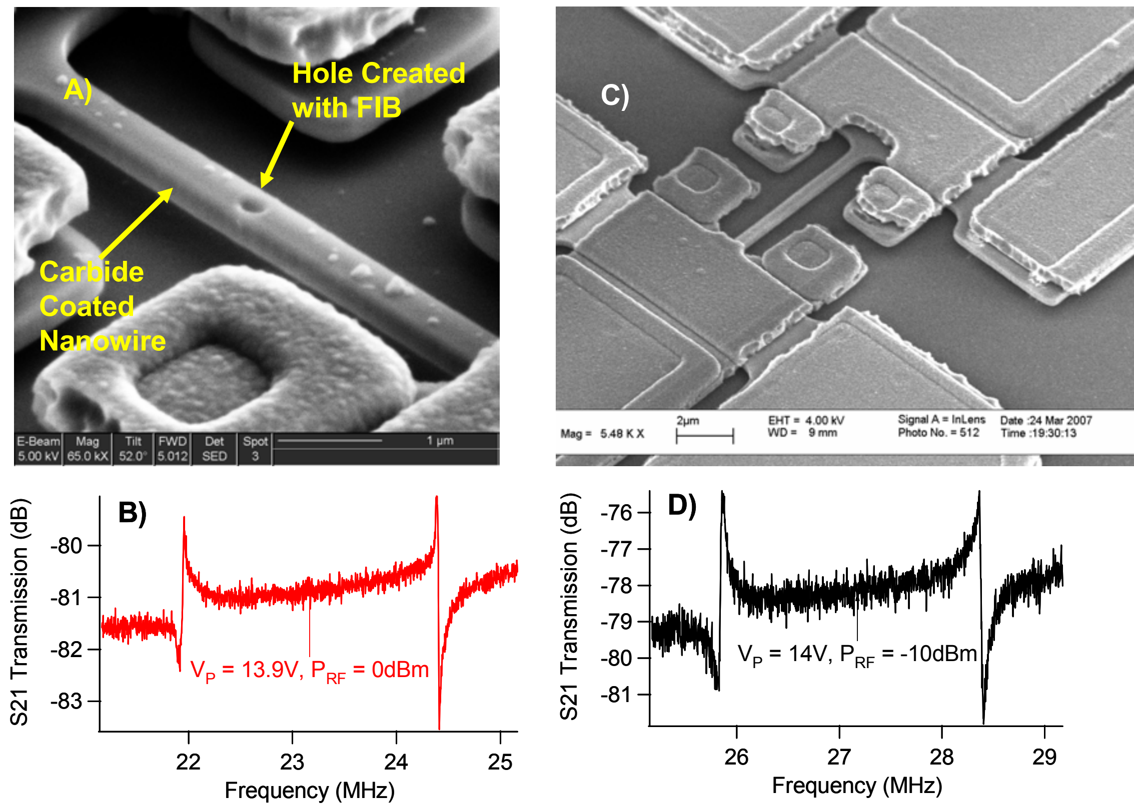

Figure 25. A) SEM of a FIB machined SiC coated nanowire coupler. B) Measured S_{21} transmission magnitude of device shown in A) with V_P = 13.6V and P_{RF} = 0dBm. C) SEM of SiC coated device which was not trimmed with the FIB. D) Measured S_{21} transmission magnitude for the device shown in C) with V_P = 14V and P_{RF} = -10dBm.

An undoped SiC film, 40 nm thick was deposited in a low pressure chemical vapor desposition reactor (Tystar 15) on maximum velocity coupled devices immediately after they were released (see Fig. 25). The measured stress of the deposited film was slightly above 1 TPa. The devices shown in Fig. 25A and 25C were not tested or imaged with the SEM before SiC deposition in order to follow LPCVD furnace cleanliness rules

developed by the Microlab. Figure 25A shows a FIB etched hole in the nanowire coupler. It was created in the hopes of etching the silicon core to yield a hollow nanobeam coupler, however, the attempt failed because the XeF_2 etcher also attacked the contact pads severing them from the polysilicon electrodes.

The resonant frequencies for both modes increased significantly relative to previous maximum velocity coupled systems measured below 20 MHz (Fig. 25B and 25D). The frequency spans were 2.53 MHz and 2.44 MHz for the devices shown in Fig. 25C and Fig. 25A respectively. The combination of high film stress and large SiC Young's modulus contributed to the shift in the resonant frequencies of both systems as well as the large frequency spans between the two resonant modes.

2.6 Coupled System Frequency Span Models

An empirical model was developed to predict the frequency spans of the coupled resonator systems. Each coupled system behaved in a unique manner because of variations in nanowire widths and MEMS resonator stiffness variations. The lack of nitride anchor reproducibility was thought to be responsible for the resonator frequency variations.

2.6.1 Maximum Velocity Coupled System Frequency Span Model

The center frequencies of the systems were first calculated from the S_{21} transmission magnitude measurements recorded at several voltages, V_P:

$$f_0(V_P) = f_1(V_P) + \frac{f_2(V_P) - f_1(V_P)}{2} \tag{11}$$

where $f_1(V_P)$ and $f_2(V_P)$ are the resonant frequency of the first and second modes respectively at a particular bias voltage V_P.

Before the nanowire was trimmed, the data for MVA was recorded on two days, two weeks apart. The calculated center frequencies for MVA are plotted versus V_P in Fig. 26. Origin 6.1 software was used to calculate a second order polynomial function to fit the data measured on the first day of testing:

$$f_0(V_P) = a + bV_P + cV_P^2 \tag{12}$$

where a = 18.22 MHz, b = 0.01 MHz/V, and c = -3X10^{-3} MHz/V^2 with a correlation coefficient of R^2 = .982. The center frequency dependence on V_P, from the Day 2 data (Fig. 26), was overestimated by the polynomial function, Eq. (12). The largest deviation occurred at V_P = 10.1V where the extracted center frequency was 60 kHz larger than the corresponding value associated with the Origin fit, Eq. (12), giving a maximum center frequency error of 0.3%. The unbiased center frequency, f_0, for MVA was defined as the maximum center frequency predicted with Eq. (12). Using this condition, the center frequency was estimated to be 18.23 MHz at V_P = 2V.

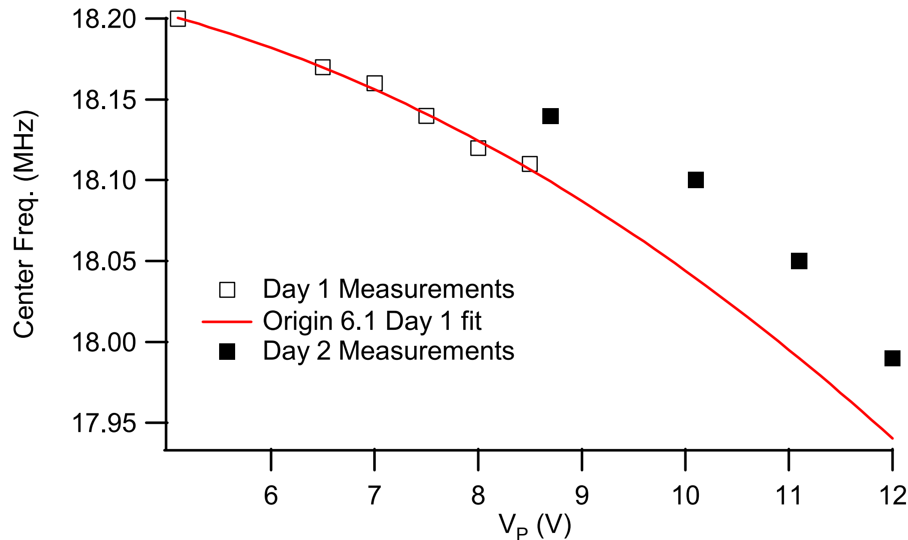

Figure 26. Center frequencies of MVA versus applied voltage before the 380nm was trimmed with the FIB. The red fitting curve was generated in Origin using a second order polynomial.

The effective mass of a single MEMS C-C resonator was calculated at x = 5 μm, or the maximum displacement point of the resonator, using Eqs. (3)-(5) with L_R = 10 μm, W_R = 3.1 μm, and H_R = 275 nm. The effective mass along with the estimated 18.23 MHz center frequency were used to calculate the effective stiffness of a MEMS C-C resonator using Eq. (6). Assuming m_{EFF} did not change when MVA was tested, the effective stiffness, k_{EFF}, of the resonator was tuned by an electrostatic spring k_E:

$$k_E = \frac{\varepsilon_0 A_E V_P^2}{d^3} \tag{13}$$

where ε_0 is the permittivity of free space (8.85X10^{-12} F/m), A_E is the area of the forcing electrode (2.48X10^{-11} m^2) and d is the vertical electrostatic gap 100 nm, assuming small displacements. The center frequency of the MEMS C-C resonator should now be:

$$f_0(V_P) = \frac{1}{2\pi}\sqrt{\frac{k_{EFF} - k_E(V_P)}{m_{EFF}}} . \tag{14}$$

Equations (13) and (14) were used to calculate the center frequencies of MVA using the effective mass and stiffness calculated at f_0 = 18.23 MHz, represented by the black asterisks shown in Fig. 27. It is suspected that the soft nitride anchors, attacked during the HF vapor release step, were also misaligned; the nitride anchors reduced the electrostatic spring softening effect on the resonant systems predicted by Eqs. (13) and (14) (see Fig. 27).

An effective voltage, V_{EFF}, was introduced to model the relatively stable center frequency of MVA. The center frequency data from Fig. 26 was used, along with m_{EFF} and k_{EFF} at 18.23 MHz, to calculate the k_E term by rearranging Eq. (14):

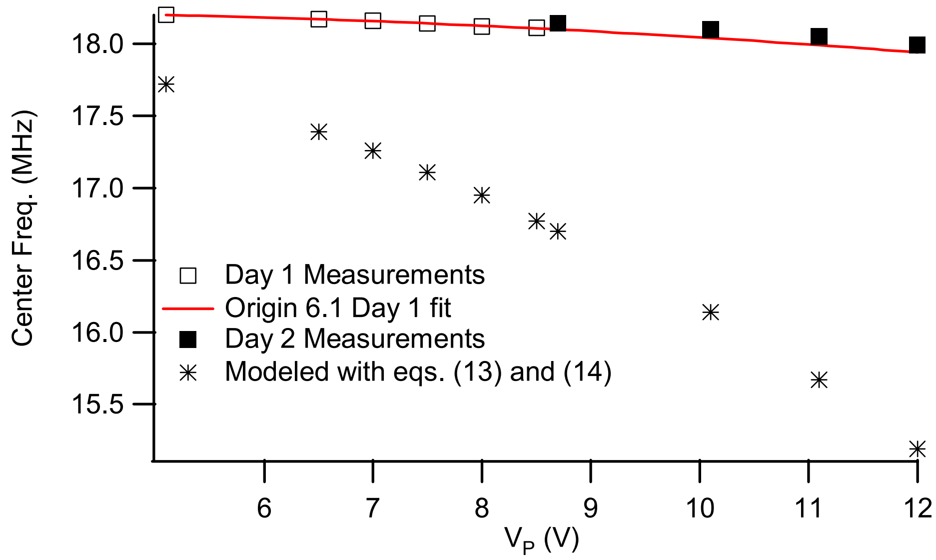

Figure 27. Center frequencies versus V_P extracted from data for MVA (380 nm wide nanowire) along with center frequencies modeled using Eqs. (13) and (14) (black asterisks)

$$k_E(V_P) = k_{EFF} - (2\pi f_0(V_P))^2 m_{EFF} . \qquad (15)$$

Using the results from Eq. (15) the effective voltage was calculated as:

$$V_{EFF}(V_P) = \sqrt{\frac{k_E(V_P) d^3}{\varepsilon_0 A_E}} \qquad (16)$$

and rounded to the nearest tenth of a volt. Origin was then used to determine an empirical fitting function for V_{EFF} versus V_P within the 5.1 to 12V range:

$$V_{EFF}(V_P) = a + bV_P + cV_P^2 \qquad (17)$$

where a = -0.77 V, b = 0.39, and c = -6E-4 /V with R^2 = 0.994 (see Fig. 28). Equation (17) was used to replace V_P in Eqs. (13) and (14) to calculate $k_{EFF} - k_E$ and ultimately estimate the frequency span between the two modes of MVA.

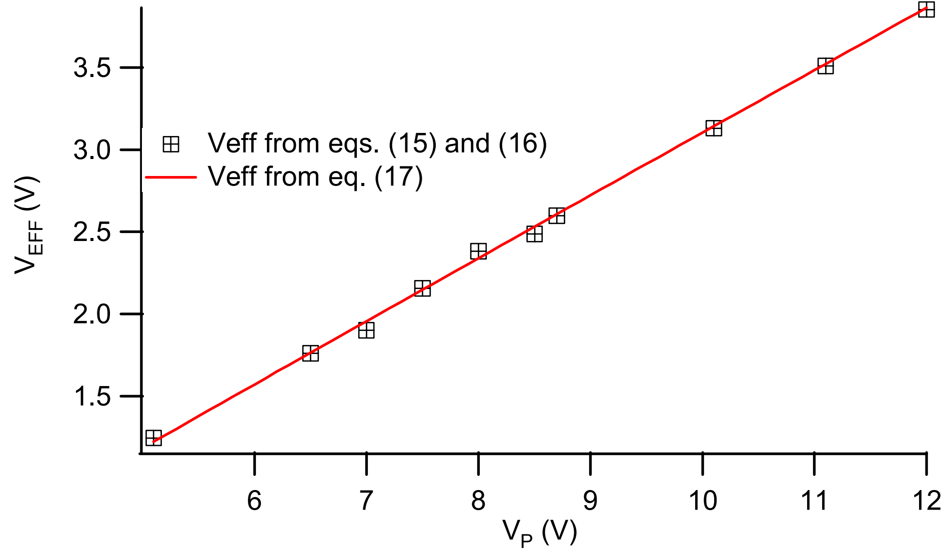

Figure 28. V_{EFF} calculated using Eqs. (15) and (16) given as discrete points and the Origin derived function from Eq. (17) (red trace).

Although the nanowire coupler of MVA was about 1 μm longer than a true quarter wavelength coupler with W_{NW} = 380 nm and H_{NW} = 275 nm, the stiffness of the nanowire coupler was calculated using Eqs. (7) and (8).

The final frequency span was then calculated as:

$$\Delta F = BW \approx \left(\frac{k_{NW}}{k_{EFF} - k_E(V_{EFF})} \right) f_0(V_{EFF}) \tag{18}$$

where $f_0(V_{EFF})$ was calculated using Eq. (14) with V_{EFF} replacing V_P. The frequencies of Modes 1 and 2 were estimated by:

$$f_1(V_{EFF}) = \frac{1}{2\pi} \sqrt{\frac{k_{EFF} - k_E(V_{EFF})}{m_{EFF}}} - \frac{\Delta F}{2}, \tag{19}$$

$$f_2(V_{EFF}) = \frac{1}{2\pi} \sqrt{\frac{k_{EFF} - k_E(V_{EFF})}{m_{EFF}}} + \frac{\Delta F}{2}. \tag{20}$$

Table 4 lists the data extracted from the S_{21} transmission magnitude measurements. Table 5 list the results of the model outlined in this section. Not only was the center frequency of MVA stable over the 6V range, but the frequency span

Bias Voltage (V)	Mode 1 (MHz)	Mode 2 (MHz)	Center Freq. (MHz)	Freq. Span (MHz)
5.1	17.54	18.86	18.20	1.32
6.5	17.51	18.83	18.17	1.32
7	17.50	18.82	18.16	1.32
7.5	17.48	18.80	18.14	1.32
8	17.46	18.78	18.12	1.32
8.5	17.45	18.77	18.11	1.32
8.7	17.48	18.80	18.14	1.32
10.1	17.44	18.75	18.10	1.31
11.1	17.40	18.70	18.05	1.30
12	17.34	18.64	17.99	1.30

Table 4. Recorded data for device MVA (380 nm wide nanowire) on Day 1 (grey cells) and Day 2 (white cells) along with extracted center frequencies and extracted frequency spans. The average span was 1.32 MHz with a standard deviation of 8 kHz.

Bias Voltage (V)	Mode 1 (MHz)	Mode 2 (MHz)	Center Freq. (MHz)	Freq. Span (MHz)
5.1	17.56	18.84	18.20	1.28
6.5	17.53	18.81	18.17	1.28
7	17.52	18.80	18.16	1.28
7.5	17.50	18.78	18.14	1.28
8	17.49	18.76	18.13	1.28
8.5	17.47	18.75	18.11	1.28
8.7	17.46	18.74	18.10	1.28
10.1	17.40	18.68	18.04	1.28
11.1	17.36	18.63	18.00	1.28
12	17.31	18.59	17.95	1.28

Table 5. Model results for device MVA (380 nm wide nanowire).

between the two resonant modes varied by only 20 kHz over the same range (Table 4). As expected the model estimates the resonant frequencies of Modes 1 and 2 reasonably well for the Day 1 data, but begins to deviate from the data recorded on Day 2. Comparing Table 4 and Table 5, at 10.1V and 11.1V, the model underestimates Mode 1 by 40kHz and underestimates Mode 2 by 70 kHz. The modeled frequency span was a constant 1.28 MHz over the entire voltage range which was off by a maximum of 3% relative to 1.32 MHz measured frequency span measured for MVA.

The modeling procedure was repeated for MVA, with the FIB trimmed coupler (232 nm wide), and the (100) oriented device with the FIB trimmed nanowire shown in Fig. 17, (a model was not created for the (100) oriented device before the coupler was trimmed because it was only tested at three bias voltages). The complete modeling results for both devices are given in Appendix A. Briefly summarizing, the modeled span of MVA (with the 232 nm wide coupler) was calculated to be 0.78 MHz compared to the average 0.85 MHz span measured for the device yielding an error of 8%. For the device shown in Fig. 17, the coupler was modeled with an average width weighted by the length of each tether and the island:

$$W_{AVE_NW} = \frac{160(L_{LT}) + 460(L_{IS}) + 180(L_{RT})}{L_{LT} + L_{IS} + L_{RT}} \quad [nm] \tag{22}$$

where L_{LT}, L_{IS}, and L_{RT} are the lengths of the left tether (2.8 μm), island (1 μm), and right tether (2.6 μm) respectively. The modeled span for this device, with W_{AVE_NW} = 216 nm from Eq. (22), was 0.7 MHz which was 80 kHz or 10% smaller than the average measured span of 0.78 MHz.

2.6.2 Low Velocity Coupled System Frequency Span Model

In contrast to the maximum velocity coupled devices, the coupling point for LVA is x = 1.5 μm, altering the effective mass and stiffness of the MEMS C-C resonators relative to the maximum velocity devices, Eqs. (3) and (6). The center frequencies were extracted from the 3dB bandwidth data of LVA, after the coupler was trimmed to 260 nm (Table 6). Similar to the maximum velocity model procedure described earlier in this section, Origin was used to create a fitting function to the data and estimate f_0 (19.00 MHz) using Eq. (12) with a = 18.90 MHz, b = 0.05 MHz/V, and c = -0.006 MHz/V^2 with R^2 = .998. The effective mass was calculated with L_R = 10 μm, W_R = 3.1 μm, and H_R = 275 nm at x = 1.5 μm. Next the effective stiffness was calculated with the estimated center frequency (19.00 MHz). Equations (13) and (14) were then used to calculate the center frequency of LVA as a function of the applied bias voltage, V_P, and graphed in Fig. 29 (black asterisks). In contrast to MVA (Fig. 27), the center frequencies of LVA calculated with Eqs. (13) and (14) underestimated the center frequency dependence on V_P

Bias Voltage (V)	Mode 1 (MHz)	Mode 2 (MHz)	Center Freq. (MHz)	3dB BW (MHz)
8.3	18.89	18.95	18.92	0.06
8.8	18.85	18.91	18.88	0.06
9.2	18.82	18.89	18.86	0.07
9.6	18.80	18.87	18.84	0.07
10.7	18.72	18.79	18.76	0.07
12.6	18.54	18.63	18.59	0.10
14.5	18.31	18.43	18.37	0.12

Table 6. Measured data from LVA with a FIB trimmed 260 nm wide coupler with P_{RF} = -24dBm. The average span was 0.08 MHz with a standard deviation of 20 kHz due to the larger bandwidths measured above 10.7V.

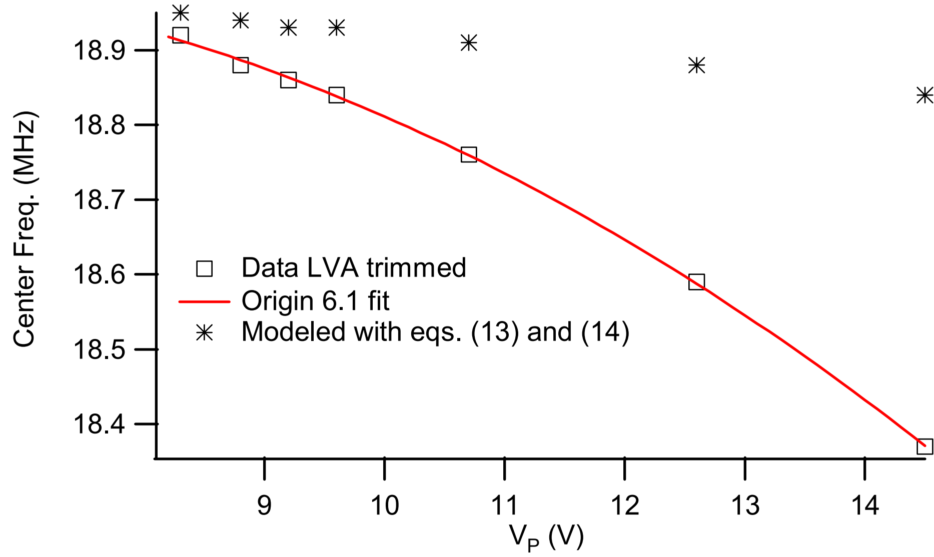

Figure 29. Center frequency data of LVA from Table 6. The unbiased center frequency (f_0 = 19.00 MHz) was extracted using the Origin polynomial fit (red trace). The black asterisks represent the theoretical response calculated using f_0 with Eqs. (13) and (14).

(Fig. 29). The effective voltage correction term was not used for the LVA frequency span (3dB bandwidth) model because the maximum deviation between the empirically modeled center frequency and the extracted frequency was only 3% (at a bias voltage of 14.5V).

A 6 μm long segment of the LVA nanowire coupler was trimmed to a width of 260 nm (Fig. 19), so L_{NW} = 6 μm, W_{NW} = 260 nm were used to calculate the nanowire stiffness using the quarter wavelength expressions, Eqs. (7) and (8). The 3 dB bandwidth was estimated with:

$$\Delta F = BW \approx \left(\frac{k_{NW}}{k_{EFF} - k_E(V_P)} \right) f_0(V_P) \tag{23}$$

where $f_0(V_P)$ was calculated using Eq. (14). The frequencies of Mode 1 and Mode 2 were calculated using:

$$f_1(V_P) = \frac{1}{2\pi}\sqrt{\frac{k_{EFF} - k_E(V_P)}{m_{EFF}}} - \frac{BW}{2} \tag{24}$$

$$f_2(V_P) = \frac{1}{2\pi}\sqrt{\frac{k_{EFF} - k_E(V_P)}{m_{EFF}}} + \frac{BW}{2}. \tag{25}$$

The results of the empirical model for LVA are given in Table 7. The modeled frequencies for Mode 1 and Mode 2 differ by 3% at 14.5V compared to the measured frequencies of LVA, however, the bandwidth proved to be significantly more difficult to predict. The measured bandwidth of LVA varied from 60 kHz to 120 kHz as V_P was increased from 8.3V to 14.5V (Table 6). The MEMS C-C resonators may not have been matched resulting in different resonant frequencies for each resonator. However, at low bias voltages, 8.3V and 8.8V, the bandwidth was predicted to within 10 kHz, or 17% of the measured LVA bandwidth.

Bias Voltage (V)	Mode 1 (MHz)	Mode 2 (MHz)	Center Freq. (MHz)	3dB BW (MHz)
8.3	18.92	18.97	18.95	0.05
8.8	18.91	18.97	18.94	0.06
9.2	18.91	18.96	18.94	0.05
9.6	18.90	18.96	18.93	0.05
10.7	18.88	18.94	18.91	0.06
12.6	18.85	18.90	18.88	0.05
14.5	18.81	18.86	18.84	0.05

Table 7. Modeling results for LVA using f_0 = 19.00 MHz and Eqs. (23) and (25). The predicted 3dB bandwidth varies by 10 kHz since the modeled frequencies for Mode 1 and Mode 2 were rounded to the nearest 10 kHz resulting in an rounding error for the 3dB bandwidth.

2.6.3 Coupled System Frequency Span Model Limitations

The max velocity and low velocity models assumed that the MEMS C-C resonators were matched, however, the testing results from the trimmed LVA device seem to indicate that the coupled microresonators may not have the same resonant frequency. The fabrication process, which will be described in the following chapter, created variations not only in MEMS C-C dimensions, but in the stiffness of each resonator due to the silicon nitride anchoring material and anchor misalignment. In addition, the nanowires were modeled as quarter wavelength couplers, but their lengths were usually 1 μm longer than the lengths required to satisfy the quarter wavelength criteria given by Eq. (9). Mass loading of the MEMS resonators may still be significant for these coupled systems because the length and height of the couplers were similar to those of the microresonators. However, mass loading was implicitly accounted for by the extraction of the unbiased center frequencies using empirical expressions generated by Origin to fit the measured center frequency data. In spite of the fact that mismatching MEMS resonators were not modeled, the empirical models produced reasonable frequency span estimates.

2.7 Chapter Summary

Silicon nanowires were demonstrated as flexural coupling elements tethering two MEMS clamped-clamped resonators. Empirical models were developed to describe the behavior of the coupled devices. The ratio of the nanowire coupler stiffness to the effective stiffness of the MEMS resonators was tuned by attaching the nanowire coupler at two different locations along the length of the MEMS resonators, trimming the width

of the nanowire coupler with a focused ion beam, or depositing films on the nanowire coupler.

The nanowire-coupled MEMS resonators described in this chapter have low quality factors making them unsuitable for MEMS filter applications. In general, high-Q resonators are required to create low insertion loss MEMS filters [1,2,4]. However, these devices may be used as nanometrology instruments given the demonstrated frequency span dependence on nanowire stiffness.

2.8 References

[1] F. D. Bannon, J. R. Clark, and C. T.-C. Nguyen, "High-Q Microelectromechanical Filters", *IEEE Journal of Solid-State Circuits*, Vol. 35, 2000, pp. 512-526.

[2] S.–S. Li, M. U. Demirci, Y.-W. Lin, Z. Ren, and C. T.-C. Nguyen, "Bridged Micromechanical Filters", *Proceedings of the 2004 IEEE International Frequency Control Symposium and Exposition*, Montreal, Canada Aug. 23-27, 2004 pp.280-286.

[3] K. Wang, C. T.-C. Nguyen, "High-Order Medium Frequency Micromechanical Electronic Filters", *IEEE Journal of Microelectromechanical Systems*, Vol. 8, 1999, pp.534-556.

[4] S.-S. Li, Y.-W. Lin, Z. Ren, and C. T.-C. Nguyen, "An MSI Micromechanical Differential Disk-Array Filter", *Proceedings of the 14th International Conference on Solid-State Sensors, Actuators and Microsystems* (*Transducers 2007*), Lyon, France, June 10-14, 2007 pp.307-311.

[5] S. Boussand and N. J. Tao, “Polymer Wire Chemical Sensor Using a Microfabricated Tuning Fork,” *Nano Letters*, Vol. 3, No. 8, 2003, pp.1173-1176.

[6] F. Torres, et al., “Coupling Resonant Micro and Nanocantilevers to Improve Mass Responsivity by Detectability Product”, *Proceedings of the 14th International Conference on Solid-State Sensors, Actuators and Microsystems* (*Transducers 2007*), Lyon, France, June 10-14, 2007, pp.237-240.

[7] R. A. Johnson, *Mechanical Filters in Electronics*, Wiley, New York, NY, 1983

[8] J. Gaspar, V. Chu, and J. P. Conde, “Electrostatic actuation of thin-film microelectromechanical structures,” *Journal of Applied Physics*, Vol. 93, No. 12, 2003, pp.10018-10029.

Chapter 3. Silicon Nanowire and Coupled MEMS Fabrication

3.1 Introduction

Microfabrication and assembly processes have been used successfully to integrate top-down fabricated silicon microstructures with synthetic bottom-up nanowires to create nanowire resonators [1,2] and hybrid MEMS/nanowire structures [3,4]; however, absolute control over the location of nanowire attachment points to contact pads or MEMS structures has not yet been demonstrated. Furthermore, the various metal catalysts required for Vapor-Liquid-Solid (VLS) synthesis of silicon nanowires restricts the thermal budget of any subsequent post-synthetic processing steps and in the case of gold catalyst particles can contaminate microfabrication tools used to process transistor-grade silicon wafers. To avoid the problems associated with VLS nanowires, a top-down fabrication process was designed to create the nanowire coupled resonator devices described in Chapter 2 and the nanowire resonators discussed in Chapter 4. To mimic the single crystalline structure of synthetic nanowires, (100) silicon-on-insulator (SOI) wafers were used as the starting material for the fabrication process.

3.2 Top-Down Process Flow

Six inch (100) SOI wafers, with a 275 nm thick device layer and 400 nm thick buried oxide (BOX), were used as the substrates for this fabrication process. Cross-sections will be used to describe the fabrication process of a maximum velocity coupled device (Fig. 1). Critical processing steps will be discussed in detail in four subsections following the initial process-flow overview.

The process began with a phosphorus implant and activation anneal at 1000 °C for 30 minutes. The resulting phosphorus concentration was $8X10^{18}/cm^3$. Next a 100 nm

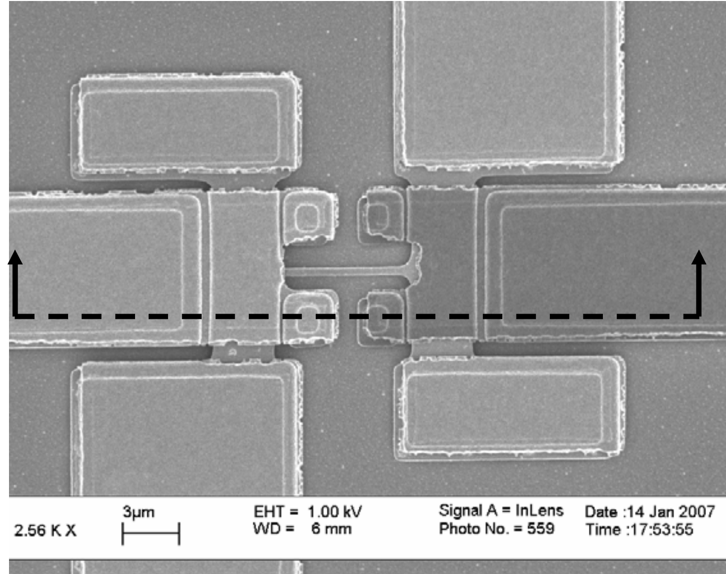

Figure 1. Released max velocity coupled device. Process flow schematics were drawn representing the cross-section highlighted in the image.

pad oxide was deposited to serve as a hard mask and etch stop for a hot phosphoric acid etching step.

Holes were patterned and etched through the pad oxide, silicon device layer, BOX, and finally etched 200 nm into the handle wafer, see Fig. 2. A 1.4 μm thick low stress nitride film was deposited using a low pressure chemical vapor deposition process to fill the holes etched into the film stack. Hot phosphoric acid (160 °C) was used to

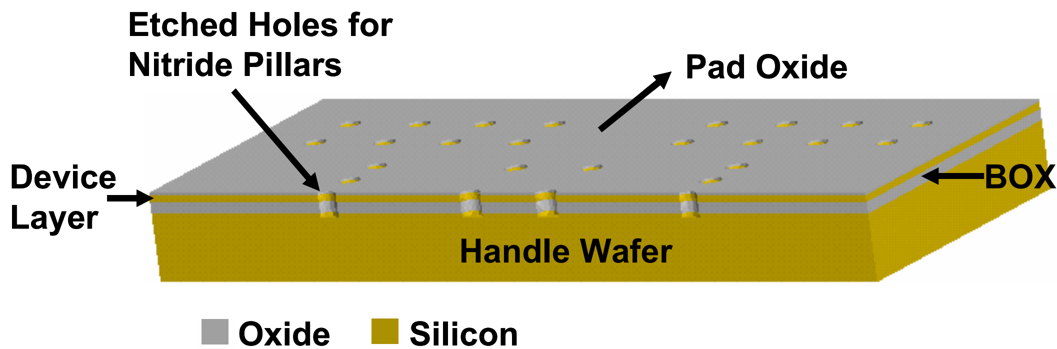

Figure 2. Holes have been etched into the film stack for nitride pillar creation

remove the nitride from the top surface of the pad oxide, while leaving the nitride pillar anchors intact (Fig. 3).

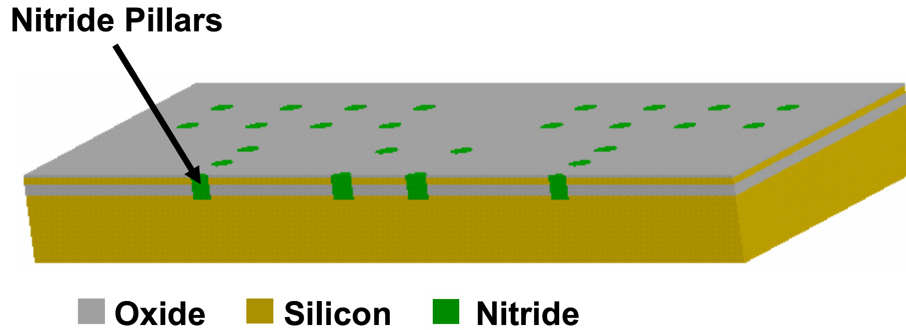

Figure 3. Nitride pillars remain after nitride deposition and hot phosphoric acid etch back process.

The max velocity device was then patterned using i-line photoresist. The i-line pattern was ashed using a parallel plate Technics PE II-A plasma etcher at 50 Watts for 1.5 minute cycles (Fig. 4). A scanning electron microscope was used to observe the width of the nanowires in between ashing cycles. Once the desired nanowire widths were achieved the ashed pattern was etched into the pad oxide and silicon device layer using reactive ion etch processes.

After the maximum velocity device structure was etched into the device layer, a sacrificial oxide was deposited to define the vertical and lateral electrostatic gaps. Windows in the sacrificial oxide were patterned and etched to anchor the polysilicon electrodes and cover the nitride anchor pillars with a polysilicon film, as shown in Fig. 5. A 400 nm thick n^+ doped polysilicon film was deposited and etched forming the RF drive and sense electrodes. Finally the system was released using a vapor hydrofluoric acid (HF) etching tool (Fig. 6). The process for NEMS resonator fabrication was identical to the process described for the maximum velocity coupled resonant system.

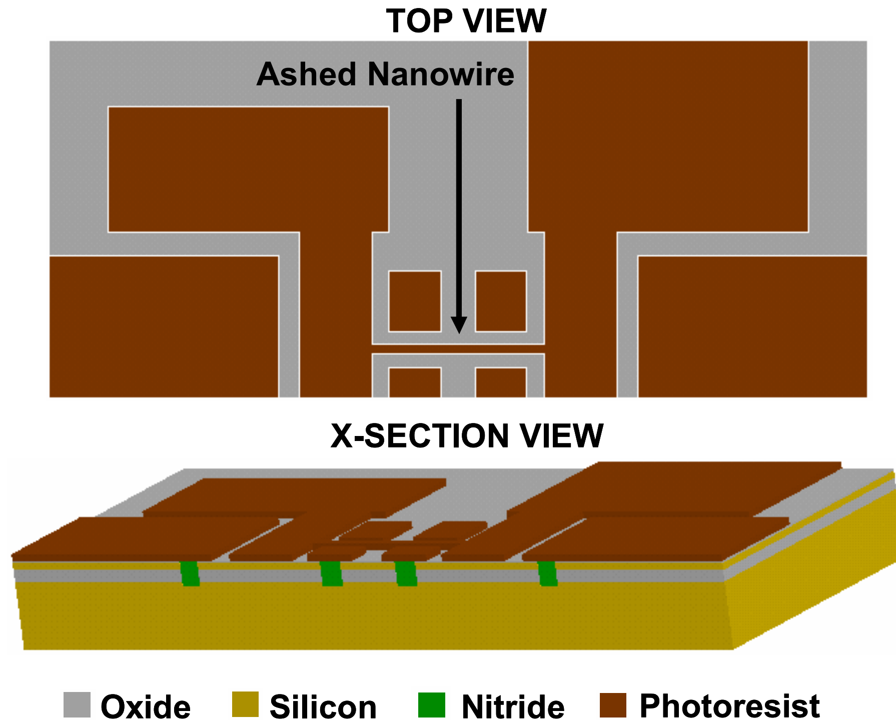

Figure 4. I-line photoresist device pattern after ashing.

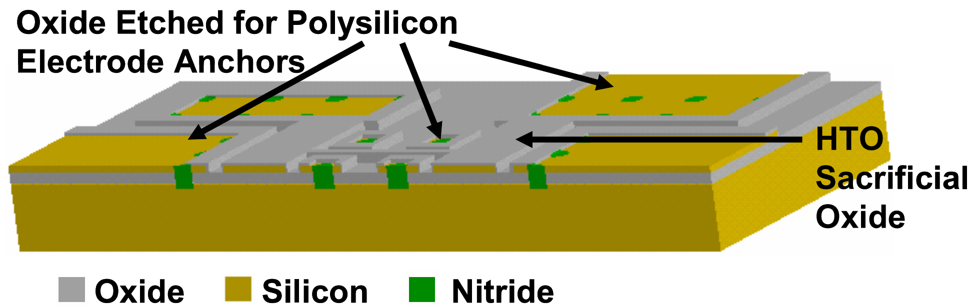

Figure 5. The sacrificial HTO was etched to anchor the polysilicon electrodes and protect the top surfaces of the nitride pillars.

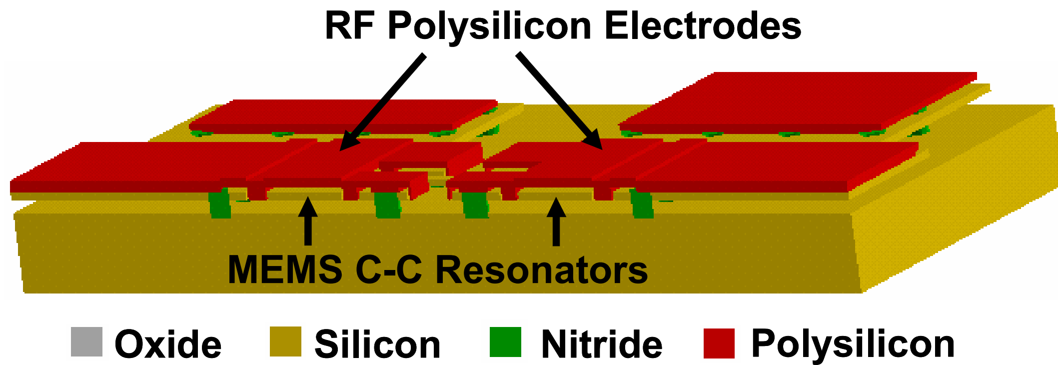

Figure 6. Released maximum velocity system with RF polysilicon electrodes.

3.2.1 Nitride Anchors

Non-conductive anchors were required for the resonant devices to prevent the electrodes from shorting through the lightly doped handle wafer. For SOI NEMS [5] or MEMS [6] devices the buried oxide (BOX) layer is typically used to fix the devices to the handle wafer. However, the buried oxide is also a sacrificial layer which must be removed for proper electromechanical device operation. Therefore, large-area anchor blocks must be etched into the device layer to avoid consuming the entire BOX anchor beneath the device layer after a timed wet HF etching process, while ensuring that the electromechanical devices are completely released. Large area BOX anchors are not used for the SOI resonant devices in order to minimize parasitic capacitances coupling the RF electrodes and to minimize the distance between clamped-clamped MEMS resonators, which dictates the length of the nanowire coupler.

Low stress silicon nitride pillars were used to minimize the anchor foot print for the MEMS and nanowire devices (Fig. 7). Nitride pillars were also used to suspend the polysilicon drive and sense electrodes above the devices. Silicon rich nitride films were attacked by HF at a slower rate than the oxide sacrificial films, however, the release process was still timed to avoid completely etching the nitride pillars (Fig. 8). Polysilicon was used as an anchor cap to prevent HF from attacking the top surfaces of the nitride pillar anchors.

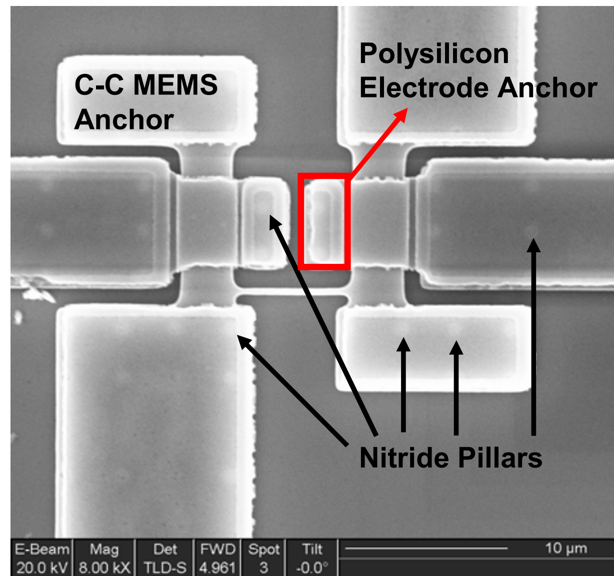

Figure 7. High voltage (20kV) SEM of a low velocity coupled device. The nitride pillars are the round light colored features. The red rectangle highlights the small size of the polysilicon electrode anchors made possible by the use of nitride pillars.

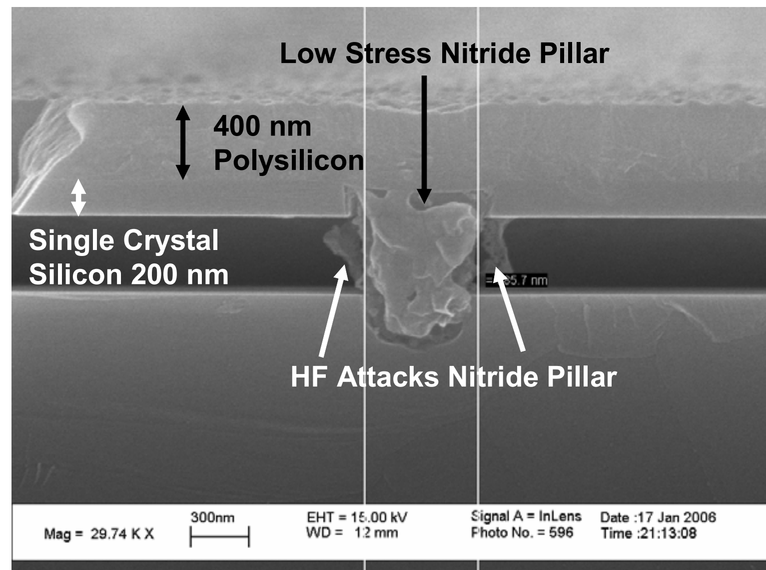

Figure 8. Cross-sectional view of a nitride pillar from the first fabrication run (the device layer was 275 nm for the final run). Polysilicon protects the top nitride anchor surface. HF attacks the 600 nm diameter pillar during the release process.

3.2.2 Nanowire Patterning

Electron beam lithography was not used to define the nanowires because the throughput would be too small to pattern nanowires over the entire surface area of a six inch SOI wafer. Instead i-line photolithography was used to define the nanowires with a minimum width of 600 nm. An oxygen plasma was then used to ash the photoresist to decrease the width of the patterned nanowire similar to work presented in [7] for deep submicron gate patterning. The ashing process attacks the lateral and top surfaces of the photoresist feature at the same rate [8] (see Fig. 9). Because the nanowires and the clamped-clamped MEMS resonators are defined at the same time, the widths of the MEMS resonators were increased on the reticle in anticipation of the lateral photoresist consumption. The contact pads and leads, connecting the pads to the devices, were also patterned at the same time as the nanowires; however, their widths were large enough such that the removal of 200 to 300 nm from the photoresist pattern had minimal impact

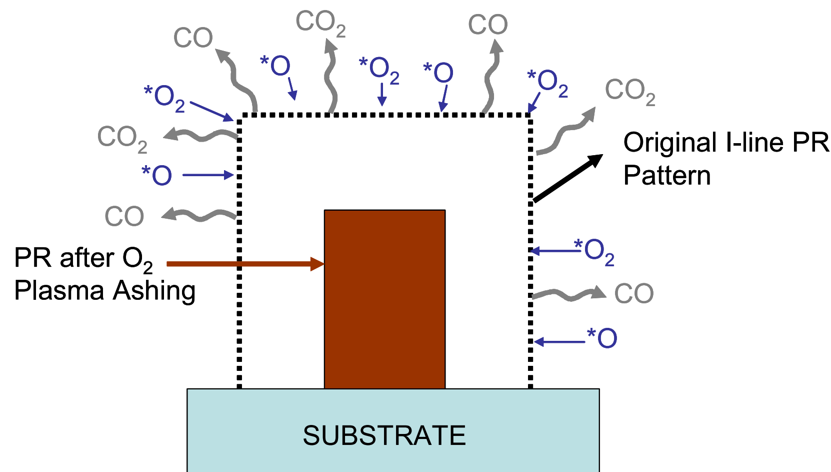

*Figure 9. Cross-sectional view of an I-line patterned feature before (dashed outline) and after (brown feature) photoresist ashing. *O and *O_2 represent the reactive species created by the O_2 plasma. CO and CO_2 are the main byproducts of the ashing process.*

on these features (Fig. 10).

The ashing rates varied when other photoresist features were patterned in close proximity to the nanowires (Fig. 11). Presumably these extra photoresist features deplete

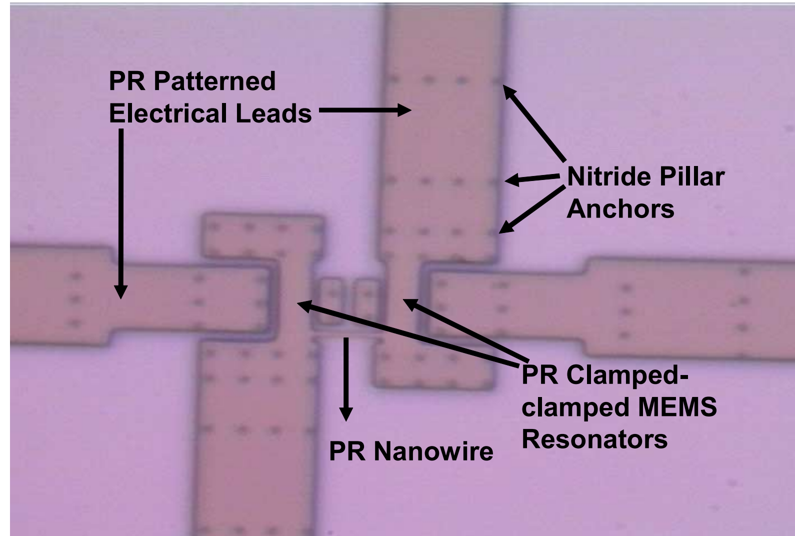

Figure 10. Optical image of I-line photoresist pattern on an SOI wafer before the ashing process. The nanowire, clamped-clamped MEMS resonators and electrical leads were patterned at the same time.

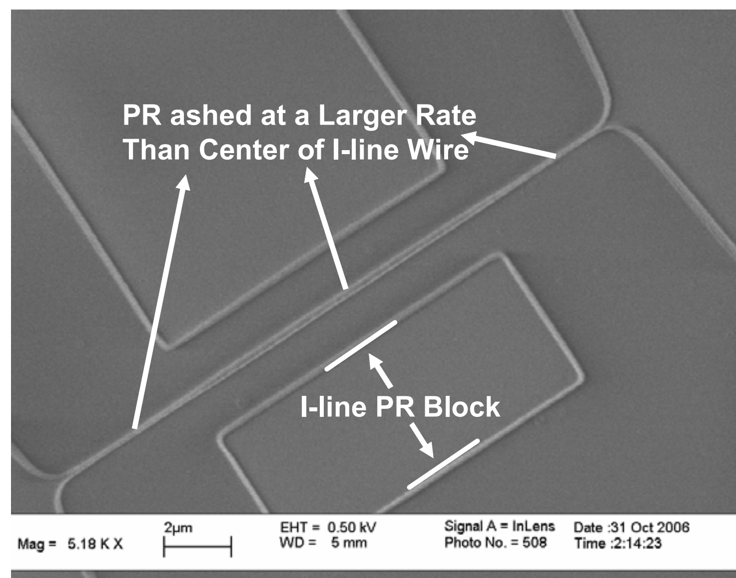

Figure 11. The I-line nanowire ashes faster where it is not in close proximity to other photoresist features.

the amount of reactive oxygen available to ash the nanowire. For long ashing times, the line edge roughness of the resist patterned wires increases, as shown in Fig. 12.

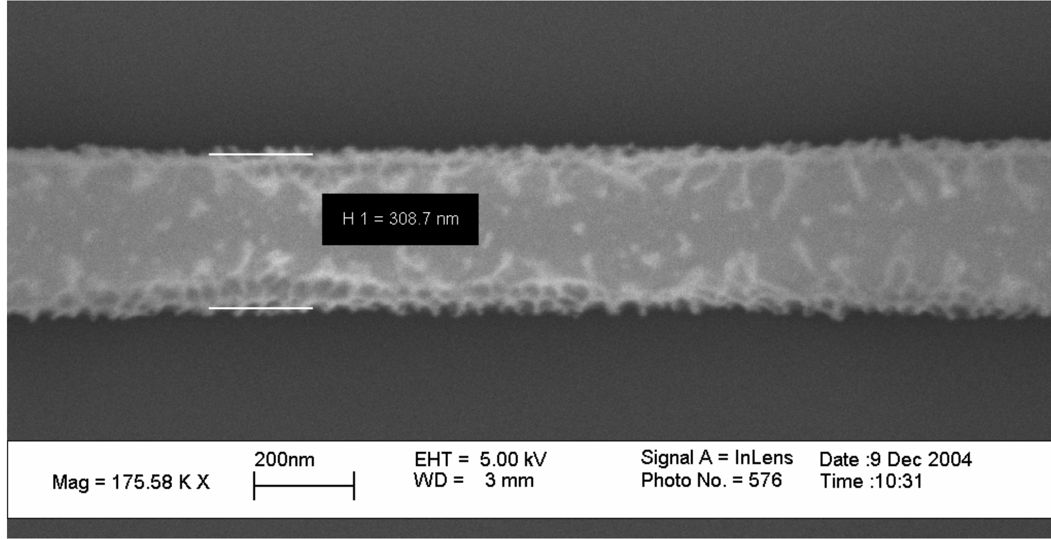

Figure 12. Line edge roughness of an ashed photoresist feature.

3.2.3 Electrostatic Gap Formation

Either large surface areas or small electrostatic gaps are required for capacitive actuation of micro and nano resonators. Electrostatic forces, F_{res}, driving a resonator at its natural frequency are inversely proportional to the electrostatic gap for voltage controlled devices:

$$F_{res} = \frac{V_P \varepsilon_0 L_E W_E v_{IN}}{d^2} \tag{1}$$

where V_P is the DC biasing voltage, ϵ_0 is the permittivity of free space, L_E and W_E are the length and width of the forcing electrode, v_{IN} is amplitude of the AC forcing signal, and d is the electrostatic gap separating the forcing electrode from the resonator. Traditionally a sacrificial silicon dioxide is used to define the electrostatic gap for MEMS resonators because of its relatively large etch selectivity with respect to poly and single crystalline

silicon in hydrofluoric acid. Control over the thickness of the sacrificial silicon dioxide is very important for electrostatically driven resonators. Both vertical and lateral electrostatic gaps are created using the top-down fabrication process. The vertical gaps are used for electrostatic actuation of micro and nanoresonators. Lateral electrostatic gaps are created to control charge carriers transiting through the nanowire resonators (described in Chapter 4).

Three sacrificial oxide films were investigated for electrostatic gap formation. Each oxide film was judged on conformality and deposition or growth rate. As shown in Fig. 13, the contact pads were cleaved and the edges of the pads were used to characterize the nanogaps, created by the sacrificial oxides, with cross-sectional SEMs. HF was used to remove the oxide from the gaps to improve the SEM contrast of the nanogap images.

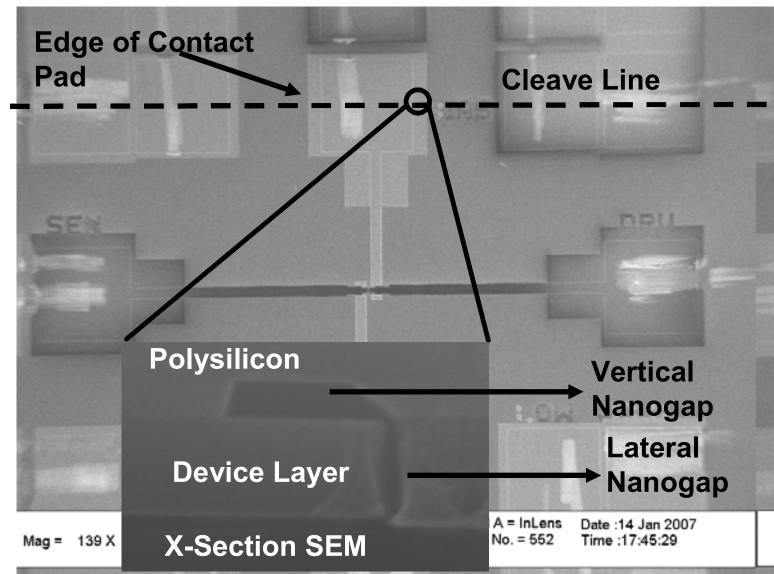

Figure 13. Die were cleaved at the large area contact pads. HF was used to etch sacrificial oxide to characterize the nanogaps formed by the three deposition/growth methods (inset cross-sectional SEM).

The first film investigated was a thermally grown silicon dioxide because precise control over oxide film thickness has been demonstrated for advanced three dimensional finFET devices [8]. A dry O_2 silicon dioxide was grown at 950°C after the device layer was etched (see Fig. 14). The desired lateral oxide thickness was 60 nm, however, the compressive stress of the growing oxide hindered growth at the base of the device layer. A pad oxide was already present on the top surface of the device layer before the wafers were oxidized resulting in a thicker oxide on the top surface of the device layer than the lateral surface (Fig. 14). If the oxidation was performed at 1100 °C, oxide reflow would have relieved the compressive stress [9]. However, at 1100 °C the phosphorus diffusion profile within the silicon becomes harder to control since phosphorus would preferentially pile-up at the oxide-silicon interface. Lower thermal budget oxide deposition processes were investigated to minimize dopant pile-up at the silicon surfaces.

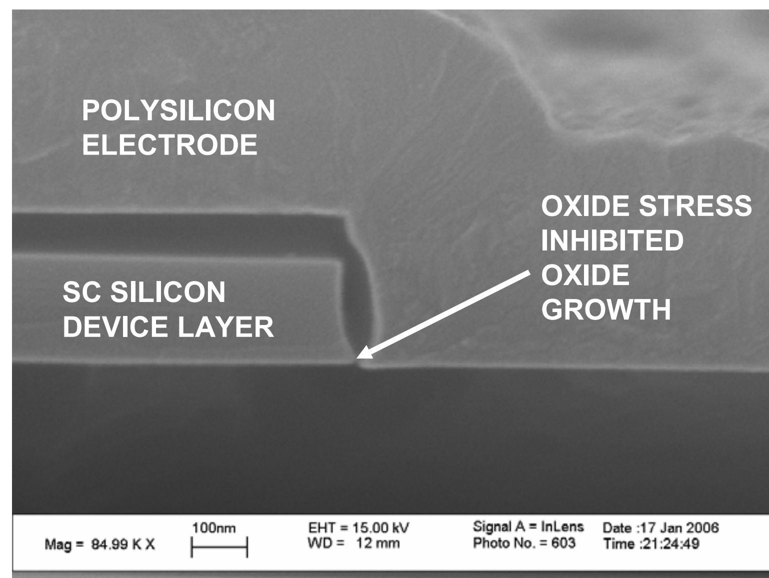

Figure 14. Electrostatic gaps were created by dry oxidation at 950 °C. The deposited polysilicon was very conformal.

Deposited oxide films were subsequently investigated, beginning with a plasma enhanced chemical vapor deposition (PECVD). A liquid tetraethooxysilane (TEOS) precursor containing silicon and oxygen was used for the deposition process. The TEOS precursor has a low sticking coefficient compared to the silane based low temperature oxide (LTO) chemistry, which in theory should favor conformal oxide deposition [9]. PECVD TEOS based oxides deposit rapidly making thickness control for sub 100 nm gaps difficult. Figure 15 shows the results of a 9 sec PECVD oxide deposition on a patterned polysilicon wafer. The deposited oxide was thicker at the top surface of the polysilicon test structure than on the polysilicon sidewall.

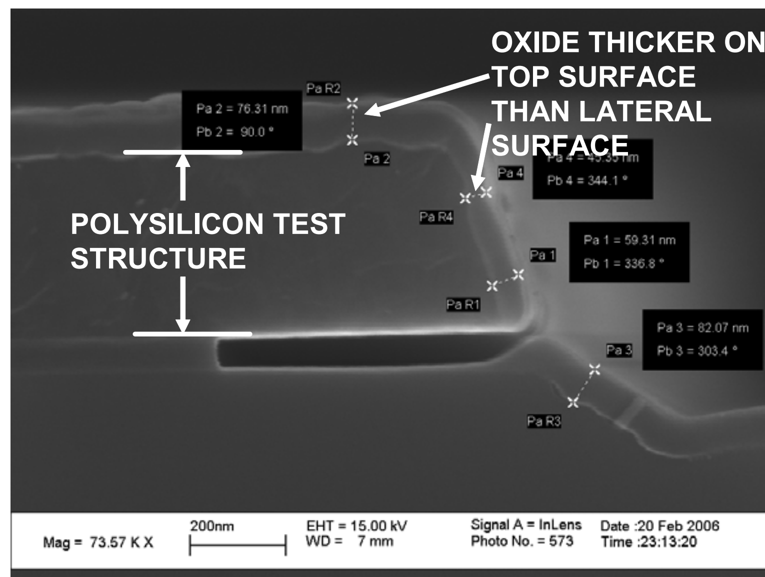

Figure 15. PECVD TEOS oxide deposited on a polysilicon test structure. The oxide deposited on the lateral surface was thinner than the oxide deposited on the top surface of the test structure.

Finally, a high temperature oxide (HTO) was investigated. A HTO film is created when dichlorosilane and nitrous oxide decompose at temperatures above 800 ℃ in low pressure furnaces. Conformal HTO deposits at relatively low deposition rates (depending on the pressure of the tube). Typical deposition rates at 835 ℃ and 300 mTorr varied from a minimum of 0.8 nm/min to a maximum of 1.4 nm/min. The oxide film used to create the gaps depicted in Fig. 16 was deposited for an hour and was more conformal than the PECVD deposited oxide.

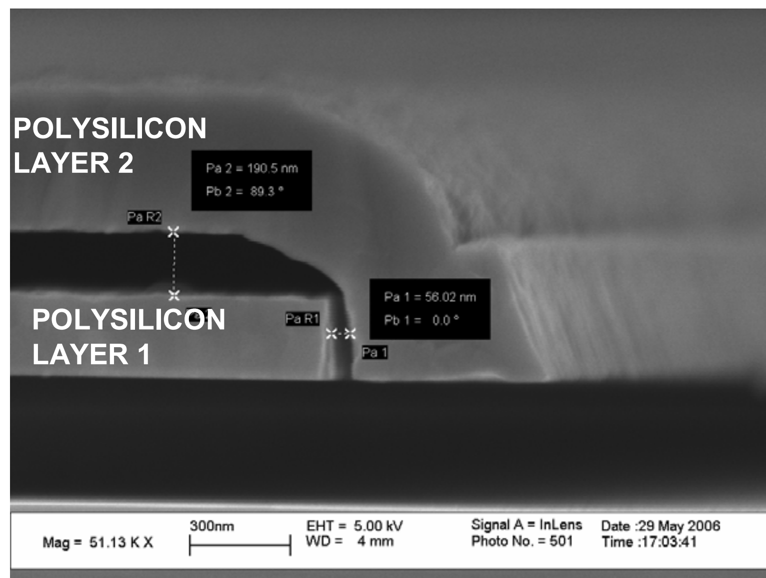

Figure 16. Electrostatic gaps created with a conformal high temperature oxide. The vertical and lateral gaps for this structure were 190 nm and 56 nm respectively (a 130 nm pad was on the surface of Polysilicon Layer 1 before the 60 nm HTO was deposited) .

3.2.4 Vapor HF Release

Vapor phase HF was used to release the fabricated devices because the standard wet HF release process followed by a critical point drying step damaged the nanowire resonator devices, see Fig. 17. The paddle heater of the Idonus vapor HF etcher was set

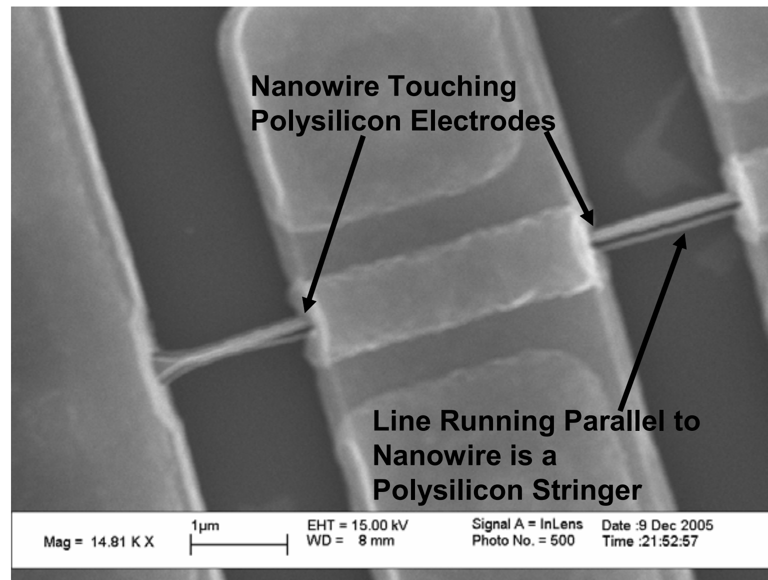

Figure 17. Nanowire device released in liquid HF and dried with a critical point drying process. The nanowire has been bent and makes contact with the polysilicon electrode.

to 40 °C and the 49% HF reservoir remained at room temperature since no temperature control for the bath or reservoir was available at the time. Water is thought to be the initiator of the vapor phase etch [10], the Idonus etcher scavenges water from the ambient and the chuck temperature controls the amount of water on the sample surface which in turn determines the oxide etch rate.

The film stack composed of the silicon device layer, 275 nm thick, and polysilicon, 400 nm thick, was semi-transparent to white light. The release process was monitored by periodically removing the die from the vapor HF tool and observing the amount of BOX undercut with an optical microscope (Fig. 18).

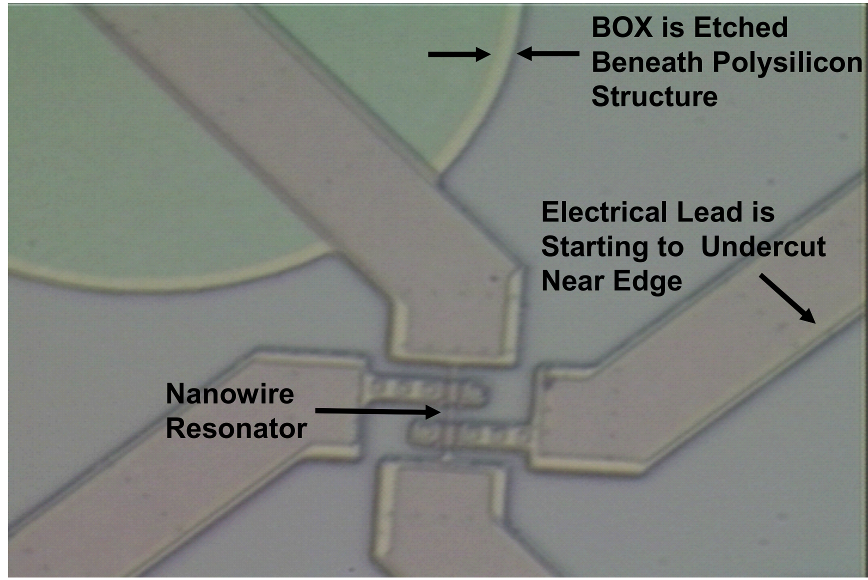

Figure 18. White light illuminated image taken with 20X objective of UVscope. The BOX was removed near the edge of the electrical lead and the polysilicon structure.

3.3 Focused Ion Beam Post Processing

A focused ion beam (FIB) is operated much like a scanning electron microscope, however unlike a SEM, ions generated by the FIB are used not only to image samples, but to mill or decompose precursor gases to form films of Pt on samples. Usually liquid phase gallium is used as the ion source [11]. As Ga wets a tungsten tip, a large voltage is used to extract ions from the tip. A series of apertures and electrostatic lenses are capable of focusing the ion current to a spot size below 10 nm [11].

FIB based fabrication processes have increased in popularity for: precision nanoscale patterning of electrostatic gaps for MEMS and NEMS devices [12,13], nanowire patterning [14], thin film deposition to create arbitrary three-dimensional micro and nanostructures [15], and implant Ga ions to dope silicon nanowire devices [16].

As discussed in Chapter 2, the FIB was used as a post-processing tool for the nanowire coupled MEMS resonators. Release holes were milled into the polysilicon electrodes to minimize nitride anchor damage during the HF release step, see Fig. 19.

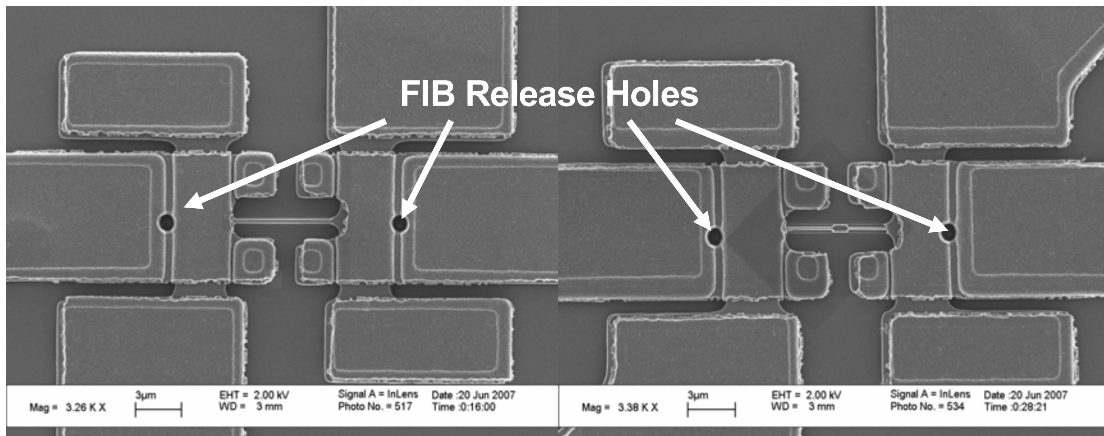

Figure 19. Release holes milled into the polysilicon electrodes with a focused ion beam.

After the nanowire devices were released and tested the nanowire couplers were milled to tune the frequency response of the system. The narrowest coupler created using the FIB milling process is shown in Fig. 20. A larger width segment, or island, at the center of the nanowire prevented the coupler from buckling during the milling process. Some nanowire couplers were milled into arbitrary shapes (Fig. 21), however, the devices shown in Fig. 21 no longer functioned because the stiffness of the nanowire coupler was substantially reduced.

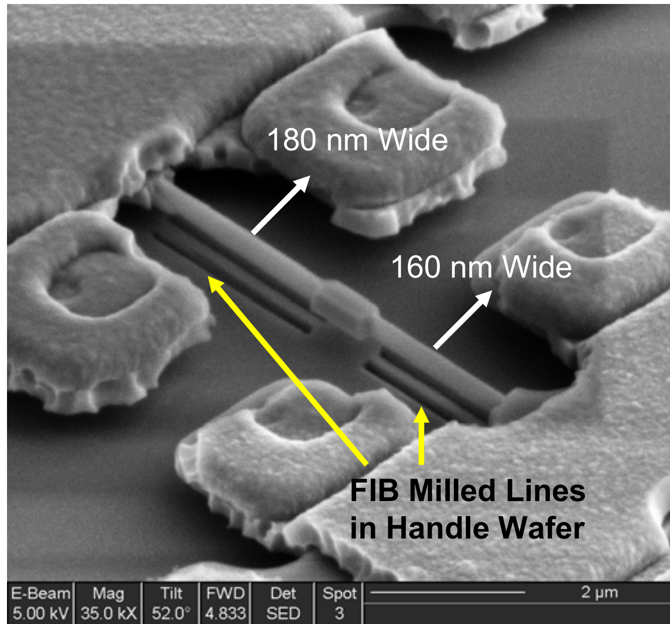

Figure 20. FIB trimmed nanowire coupler. The lines milled into the handle wafer were the result of an overetch step to ensure that the nanowire was completely milled.

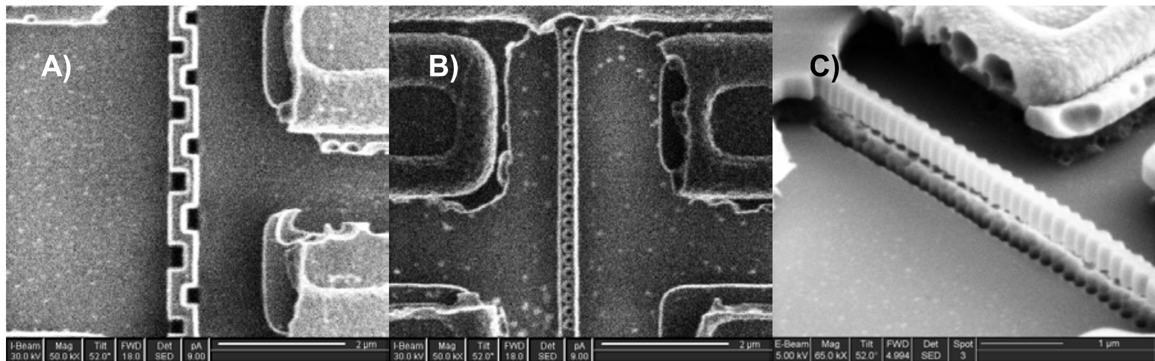

Figure 21. A) FIB milled meandering nanowire structure. B) FIB milled holes in nanowire coupler. C) FIB milled serrated nanowire coupler. Images A) and B) were generated with Ga ions, C) was taken with the electron beam optics of the FIB tool.

The FIB was also used to deposit Pt films on the nanowire couplers to increase the frequency span of the resonant systems (see Chapter 2). The FIB was not capable of depositing small area Pt films onto the nanowire couplers. The nanowire was electrically and thermally isolated from the handle wafer; consequently, ions impinging on the small areas of the nanowire ablated silicon from the nanowire instead of depositing Pt (Fig. 22A). When the deposition area was increased, Pt was deposited successfully on the nanowire surface (Fig. 22B).

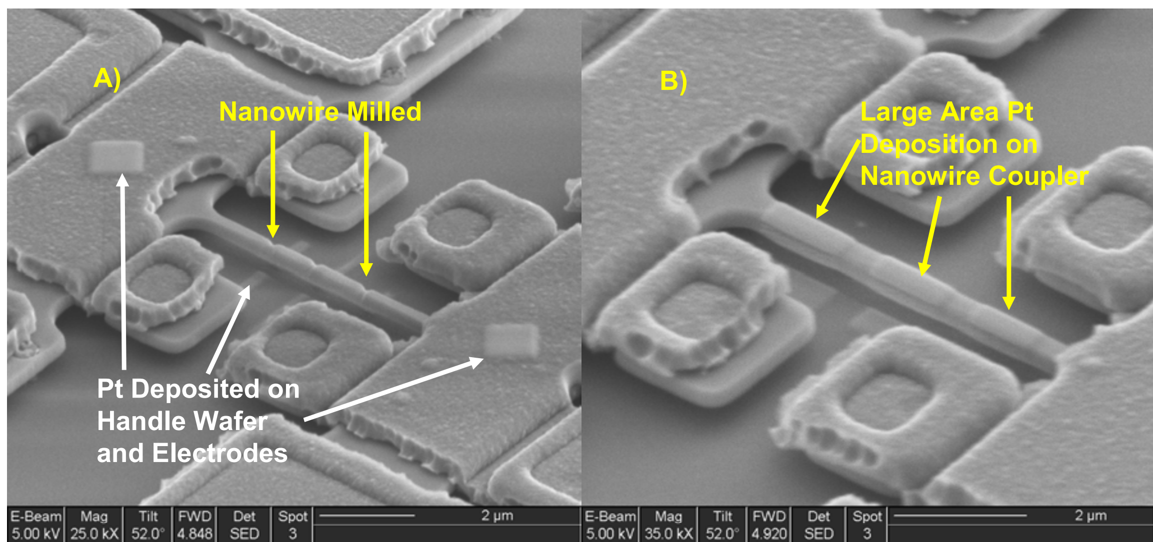

Figure 22. A) The FIB had difficulty depositing small area Pt films on the nanowires. B) Larger area films were deposited without incident.

The major drawback to using the FIB tuning technique was Ga ion implantation. Prior to silicon milling or Pt deposition, an ion image of the device was captured by the FIB tool in order to draw the desired milling or platinum deposition patterns. Before the image was captured, the ion beam was allowed to scan the device several times to make

sure the sample was in focus and the device did not charge. The ion image scans resulted in Ga implantation into the exposed silicon surfaces (see Fig. 23).

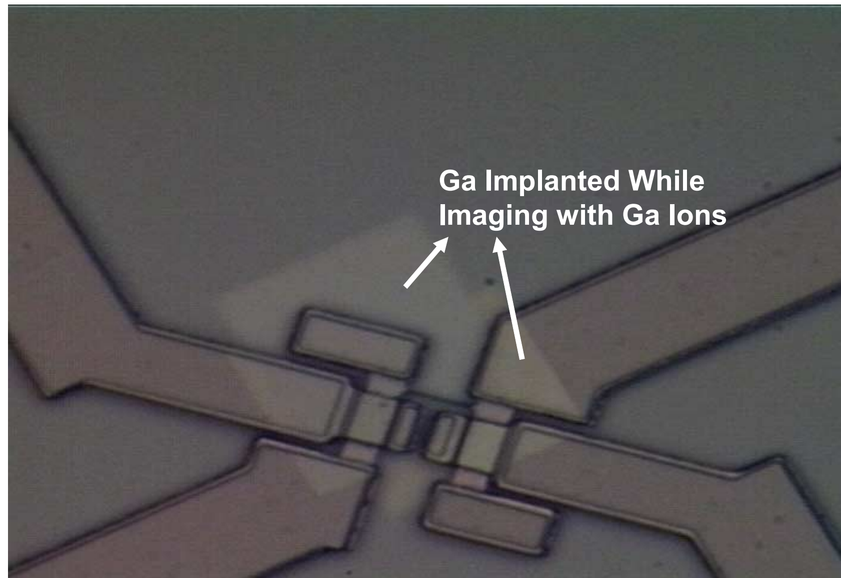

Figure 23. Microscope image of a (100) low velocity coupled device after a FIB post processing step was performed on the nanowire coupler. The Ga implanted areas are visible because the Ga changes the index of refraction of the silicon surface.

3.4 Chapter Summary

A top-down fabrication process was introduced which was used to create flexural mode MEMS resonators and nanowire resonators. Non-conductive silicon rich nitride pillars were used as anchors to reduce the footprint of the devices and decrease capacitive coupling between the device and the handle wafer. The nitride pillars were also used to suspend the polysilicon electrodes above the devices, enabling local electrostatic actuation of MEMS and NEMS resonators. i-line lithography was used to define the nanowires followed by an ashing process to reduce the line width of the nanowires.

Finally, a gallium-based focused ion beam tool was to tune the frequency response of coupled MEMS resonators after the devices were released.

3.5 References

[1] R. He, *Silicon Nanowires for Nanoelectromechanical Systems*, University of California, Berkeley Ph.D. Dissertation Fall 2006.

[2] M. Li, et al., "Bottom-up assembly of large-area nanowire resonator arrays," *Nature Nanotechnology*, Vol. 3 Feb. 2008 pp.88-92.

[3] O. Englander, *Localized Synthesis, Assembly and Integration of Silicon Nanowires*, University of California, Berkeley Ph.D. Dissertation Fall 2005.

[4] A. San Paulo, et al., "Suspended Mechanical Structures Based on Elastic Silicon Nanowire Arrays," *Nano Letters*, Vol. 7, No. 4, pp.1100-1104.

[5] M. K. Zalalutdinov, et al., "Arrays of Coupled Nanomechanical Resonators," *2006 Solid-State Sensors, Actuators, and Microsystems Workshop Hilton Head Island*, South Carolina, June 4-8, 2006, pp.216-219.

[6] S. Pourkamali, Z. Hao, and F. Ayazi, "VHF Single Crystal Silicon Capacitive Elliptic Bulk-Mode Disk Resonators – Part II: Implementation and Characterization," *Journal of Microelectromechanical Systems*, Vol. 13, No. 16, December 2004, pp.1054-1062.

[7] J. Chung, et al., "Deep-submicrometer MOS device fabrication using a photoresist-ashing technique," *IEEE Electron Device Letters*, Vol. 9, 1988 pp.186-188.

[8] Y. K. Choi, *Nanofabrication Technologies and Novel Device Structures for Nanoscale CMOS*, University of California, Berkeley Ph.D. Dissertation Fall 2001.

[9] J. D. Plummer, M. D. Deal, and P. B. Griffin, *Silicon VLSI Technology: Fundamentals, Practice, and Modeling*, Prentice Hall, New Jersey, 2000.

[10] N. Miki, et al., "Gas-Phase Selective Etching of Native Oxide," *IEEE Transactions on Electron Devices*, Vol. 37, No. 1, Jan. 1990, pp.107-115.

[11] S. Reyntjens and R. Puers, "A review of focused ion beam applications in microsystem technology," *Journal of Micromechanics and Microengineering*, Vol. 11, 2001, pp.287-300.

[12] J. H. Daniel and D. F. Moore, "A microaccelerometer structure fabricated in silicon-on-insulator using a focused ion beam process," *Sensors and Actuators A*, Vol. 73, 1999, pp.201-209.

[13] D. Grogg, D. Tsamados, N. D. Badila and A. M. Ionescu, "Integration of Mosfet Transistors in MEMS Resonators for Improved Output Detection," *Proceedings of the 14th International Conference on Solid-State Sensors, Actuators and Micro-systems (Transducers 2007)* Lyon, France June 10-14, 2007, pp.1709-1712.

[14] G. M. Kim, et al., "Nanomechanical structures with 91 MHz resonance frequency fabricated by local deposition and dry etching," *Journal of Vacuum Science and Technology B*, Vol. 22, No. 4, Aug. 2004, pp.1658-1661.

[15] S. Reyntjens and R. Puers, "Focused ion beam induced deposition: fabrication of three-dimensional microstructures and Young's modulus of the deposited material," *Journal of Micromechanics and Microengineering*, Vol. 10, 2000, pp.181-188.

[16] D. V. Scheible, et al., "Fabrication of doped nano-electromechanical systems," *Physica Status Solidi Rapid Research Letters*, Vol. 1, No. 5, 2007, pp.205-207.

Chapter 4. Silicon Nanowire Resonators

4.1 Introduction

As mentioned in the introduction chapter individual silicon nanowire resonators have been proposed for signal processing and nanomechanical computation. An actuation and detection scheme must be developed for NEMS resonators to overcome limitations presented by their small dimensions, while facilitating NEMS integration with complementary metal-oxide-semiconductor (CMOS) electronics in order to create integrated systems. Large resistances and small surface areas both limit capacitive coupling to the nanostructure and result from the small nanowire dimensions. For these small-area and highly resistive structures, parasitic noise from on-chip electronics or external environmental sources may drown out the diminutive signals generated by a vibrating nanowire resonator. This chapter will introduce a new field-effect detection mechanism for silicon nanowire resonators. The technique has been demonstrated to be effective in the presence of large parasitic capacitances. Furthermore, it is potentially CMOS-compatible through an interleaved fabrication sequence. In contrast to vibrating-gate transistor-resonator devices [13,17], where vibrating gate electrodes modulate the resistance of a stationary charge-inverted silicon channels, this new field-effect detection scheme modulates the resistance of the vibrating silicon nanowire resistor by depleting charge carriers from three nanowire surfaces.

4.2 Driving and Detection Techniques Overview

This chapter begins with an overview of several actuation and detection schemes that have been successfully demonstrated for nanowire-based or nanotube-based NEMS

resonators. Optical detection schemes will not be reviewed in this section, since electrical sense signals are better suited for CMOS system integration.

4.2.1 Capacitive Drive and Sense

NEMS resonators can be driven using capacitive actuation, because electrostatic forces can be scaled by increasing signal power or DC bias voltages to generate sufficient electrostatic force to drive a NEMS resonator, compensating for small nanowire surface areas. However, capacitive sensing of NEMS resonator motion is much more difficult. Capacitance scales linearly with area. As device dimensions decrease, capacitive coupling between NEMS resonators and capacitive electrodes also decreases. Parasitic capacitances become quite large relative to the small capacitive currents from nanowire resonators [2]. To increase capacitance between the nanowire and forcing electrodes the electrostatic gaps can be made smaller. In [1], electrostatic gaps were defined using e-beam lithography to push the lateral gap dimensions below 100 nm. Figure 1 depicts the capacitive one port sensing scheme successfully used in [1] to measure signals directly from silicon nanowire resonators at pressures of 140 Torr and below. The devices were fabricated at an eight inch STMicroelectronics facility with the aim of creating large quantities of NEMS-based timing references integrated with CMOS electronics. In spite of the sub 100 nm electrostatic gaps, DC bias voltages in the range of 13-20V were used to actuate and detect the resonant motion of the devices, which are a factor of ten higher than the supply voltages required for CMOS. More work is required to determine the ultimate limit of the capacitive sense technique for silicon nanowire resonators and to reduce the DC bias voltages required for this technique.

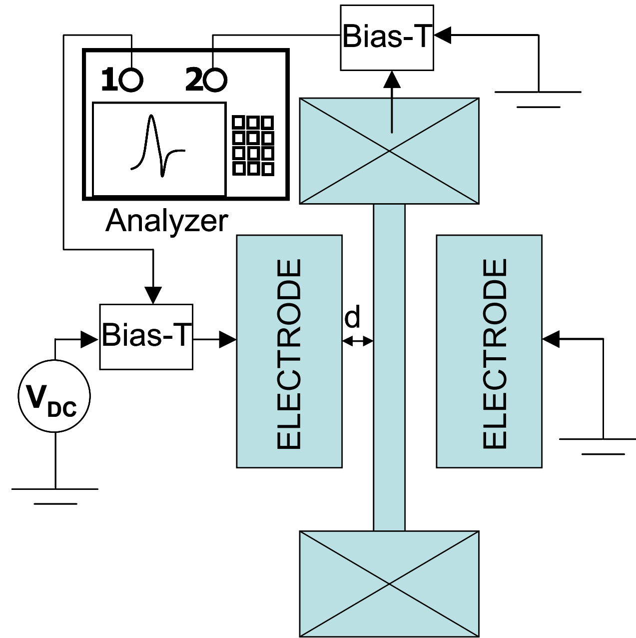

Figure 1. A NEMS double clamped beam resonator depicting one port capacitive drive and sense from [1].

4.2.2 Magnetomotive Transduction

The magnetomotive drive and sense approach was first demonstrated on NEMS resonators by Michael Roukes's group at the California Institute of Technology [3]. A metallic layer, deposited on top of the nanowire, was used to overcome the large resistance of the silicon nanowire and to achieve a better impedance match to a network analyzer. This drive and sense approach is depicted in Fig. 2. A time varying electric current was passed along the length of the wire (z direction). A magnetic field was applied perpendicular to the current flow (x direction), which generated an oscillating Lorentz force on the nanowire (y direction according to the right hand rule). The device vibrated when the frequency of the current signal matched the resonant frequency of the nanowire. The Lorentz force generated is given by:

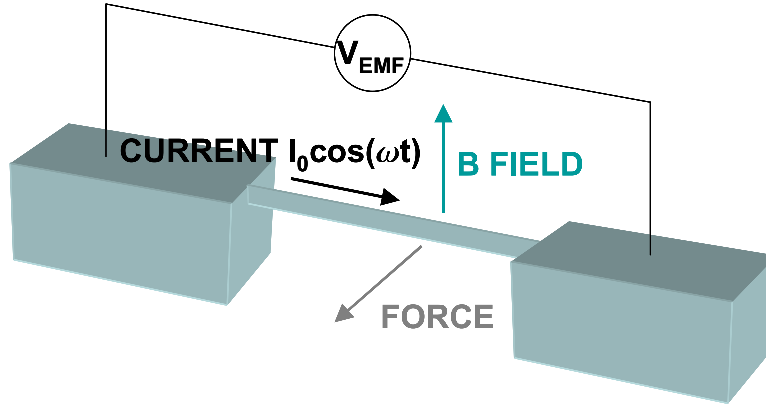

Figure 2. The magnetomotive drive and sense measurement schematic.

$$f_{\omega}(t) = LBI_{0}cos(\omega t) \qquad (1)$$

where f_{ω} is the Lorentz force at frequency ω, L is the length of the beam, B is the magnitude of the magnetic field and $I_0\cos(\omega t)$ is the RF current applied to the structure.

The resonant motion in the presence of the applied magnetic field induced an AC voltage V_{EMF}, which was measured with a network analyzer by monitoring the reflected power S_{11}. The electromotive force depends on the rate of change of the magnetic flux Φ as the beam bends [4]:

$$V_{EMF}(\omega) = \frac{d\Phi}{dt} = B\int_{0}^{L} \frac{\partial u(z,t)}{\partial t}(z)dz \propto I_{0}B^{2} \qquad (2)$$

where *u(z,t)* is the beam displacement along the length of the nanowire in the z direction at a time t.

For this transduction scheme, nanowire resonators must be probed at cryogenic temperatures to minimize thermal noise and to facilitate the use of superconducting magnets for the biasing DC magnetic fields. Magnetic fields on the order of a few Tesla are used to actuate and sense these nanowire resonators. The high magnetic fields

ultimately limit the environment in which magnetomotive nanowire resonators may operate. However, this technique is flexible enough to actuate and sense NEMS resonators created from various materials like SiC, Si, GaAs, Pt and AlN [4,5,6]. In addition, zeptogram mass sensors have been demonstrated using the magnetomotive detection method supplemented with signal mixing to further minimize the influence of parasitic signals [7].

4.2.3 Capacitive Drive and Conductivity Modulation Sense

The conductivity modulation sense technique was first demonstrated for carbon nanotubes by McEuen's group at Cornell University [8]. A metal source and drain were used to anchor a one-dimensional semiconducting carbon nanotube (CNT) above a conductive silicon substrate (see Fig. 3). The gap between the CNT and the gate was on the order of 1 μm for the demonstrated device. A polarization voltage, V_{DC}, and high frequency signal, v_{HI}, were applied via a bias T to the highly doped substrate gate to capacitively drive the nanotube. At resonance the CNT vibrated vertically, which varied the capacitance, C_G, coupling it to the gate electrode. The resonating CNT was used as a mixer, exploiting the nonlinear relationship between CNT conductivity and the gate

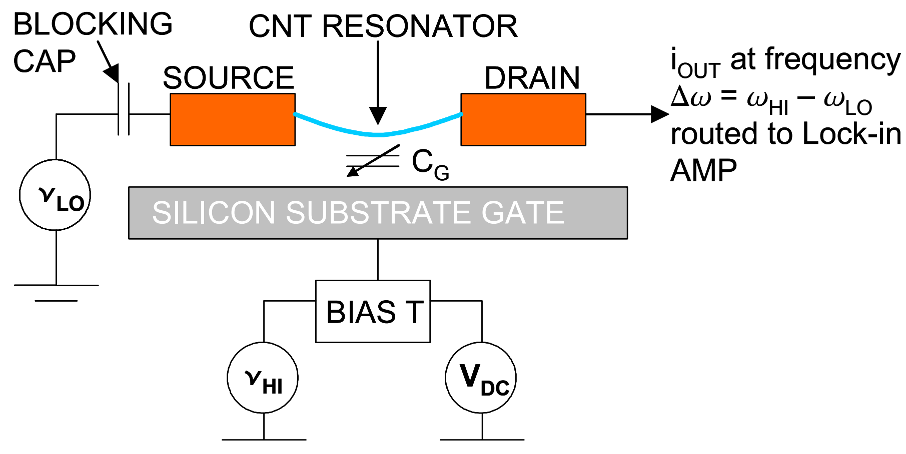

Figure 3. Test setup for a room temperature carbon nanotube resonator. From [8]

capacitance C_G [9]. A low frequency signal, v_{LO}, was applied to the source contact which mixed the output signal, i_{OUT}, to a lower frequency determined by the frequency difference between the gate and source signals ($\Delta\omega = \omega_{HI} - \omega_{LO}$). The output signal was mixed to a lower frequency in order to increase the signal to feedthrough level [9]. The nanotube output current was routed out of the drain contact to a lock-in amplifier. The high frequency signal on the gate modulated the charge on the nanotube surface. At resonance the modulated charge on the CNT surface is given by [8]:

$$\partial q = \partial(C_G V_{\boldsymbol{G}}) = C_G \partial V_G + \partial C_G V_G \tag{3}$$

where V_G is the total voltage applied to the gate, including both the DC bias voltage and the small signal.

The CNT resonator was tested in vacuum at room temperature [8], which was quite an accomplishment at the time since most NEMS resonators, up to that point, were tested at cryogenic temperatures using the magnetomotive scheme described earlier. The limits of the technique were pushed further by Alex Zettl's group at the University of California, Berkeley. They demonstrated two CNT resonators; one with a fundamental frequency of 1.3 GHz which operated at room temperature in air and another vibrating at 4 GHz [10, 11]. They used a similar test setup however the signal applied to the source had a frequency of $2\omega_{HI} + 7\,\text{kHz}$, or two times the forcing frequency, since the electrostatic force on the CNT resonator is proportional to the square of the small signal applied to the gate the output signal can be detected at 7 kHz [10].

It is speculated that the signals measured by the lock-in amplifier were due to the strain induced at the metal CNT contacts at resonance [10]. It has been shown that the contact resistance can dominate the conductive properties of one-dimensional CNT field

effect devices [12]. The single-walled CNT resonant devices described in this section were assumed to be ballistic. Charge carriers on ballistic CNTs do not experience very many scattering events as they travel along the length of the tube from the source to the drain [9]. Consequently the resistances of the CNTs were on the order of tens to hundreds of kiloOhms, enabling the use of this detection method [9,10].

The only detrimental aspect of this approach is the complexity of the detection scheme. Two high frequency signal sources and many discrete circuits, not shown in Fig. 3, are required for the mixing methods used in [8] and [10]. However, the demonstrated operation in air is promising for future NEMS resonator-based signal processing and computation systems.

4.2.4 Field-Effect Detection of MEMS Resonators

The first demonstrated resonating gate transistor (RGT) consisted of a cantilevered metal gate electrode suspended above a lightly doped transistor channel coupling the source and drain terminals (Fig. 4). The device was originally designed as a high-Q bandpass filter for frequency domain signal processing [13]. At the time, stable high-Q tuned circuits were difficult to implement because of the variability in discrete components, such as inductors and capacitors, used to create active feedback networks [14]. The RGT was an attractive alternative to discrete component based circuit topologies because a high-Q micromechanical component could be fabricated on chip with corresponding active circuitry enabling batch fabrication of integrated tuned circuits.

For the device shown in Fig. 4, the metal gate was actuated electrostatically with a dedicated metal electrode beneath the cantilevered gate. At resonance the vertical motion of the gate altered the capacitance coupling the mechanical gate to the fixed silicon

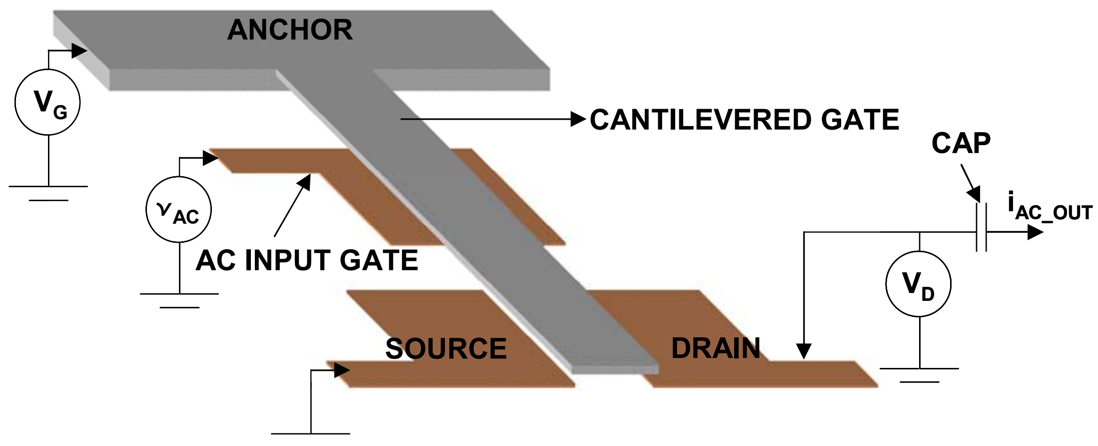

Figure 4. Schematic of the resonant-gate silicon surface transistor along with biasing scheme for resonant motion detection. From [13].

channel, thereby modulating the conductance of the transistor. The change in conduction was monitored by observing the AC component of the current flowing from the source to the drain at resonance on an oscilloscope. A capacitor was used to block the DC drain voltage and extract the AC current signal out of the drain terminal (Fig. 4). Depending on the biasing conditions of the field-effect transistor [15], along with careful design of transistor dimensions, length and width, the RGT is capable of amplifying the AC current signal due to gate displacement at resonance [16, 17]. Therefore, the RGT provides a built-in advantage over the capacitive readout method typically used to sense microresonator motion [15]. Resonating gate transistors have been demonstrated within the past two years, using modern CMOS-compatible materials and processes [17].

Field-effect transistor (FET) readout capability is not limited to bending mode resonators suspended above fixed semiconducting channels. A resonant body transistor (RBT), a configuration in which a channel vibrates while the gate electrode remains

stationary, was demonstrated on a bulk-mode silicon resonator [18]. A lightly doped FET channel was built into the sidewall of a lamé-mode microresonator with highly doped anchors serving as the source and drain terminals of the device. The device did not operate as expected due to the rather low subthreshold slope (10V/decade) of the transistor. The RBT lacked a smooth lateral surface, a result of the RIE etching used to create the device, and also lacked a passivation layer which would limit the charge trap density at the channel surface. The quoted threshold voltage V_T for this device was 100V, even with electrostatic gaps on the order of 60nm.

RBT readout has been proposed by researchers [19,20] to enable silicon nanowire resonator detection at room temperature without relying on the electrical signal mixing techniques described earlier in the chapter. The built-in amplification capability of a vibrating transistor would facilitate nanoelectromechanical signal propagation for downstream electrical domain circuit operations. The expected low bias voltage operation is especially attractive for integration with CMOS electronics. However, like the bulk-mode RBT, surface charge traps can degrade the response of a nanowire resonant body device. The increased surface-to-volume ratio of silicon nanowires can be exploited to increase gate control over the three dimensional nanowire channel compared to two dimensional microscale surface channels. In addition, nanoscale electrostatic gaps can help maximize control over the nanowire channel. Moreover, if depletion mode nanowire devices were developed, analogous to the junction field-effect transistor (JFET) where current is passed through a three-dimensional channel as opposed to a two-dimensional surface channel, charge carriers would be forced away from the surface charge traps. Since charge carriers do not interact with the nanowire surface in depletion

mode devices, surface scattering would decrease resulting in larger charge mobility. For depletion mode devices the surface of the silicon nanowires is not inverted, so the DC bias voltages applied to small-area electrodes can be reduced compared to vibrating field-effect transistor devices with equivalent electrostatic gaps [24].

4.3 Field-Effect Detection of Silicon Nanowire Resonators

The remainder of this chapter will describe a new field-effect detection scheme for silicon nanowire resonators which may enable future CMOS-integrated NEMS signal processing and computation systems. This detection method has been demonstrated on single nanowire resonators and on mechanically coupled nanowires at room temperature in a vacuum chamber maintained at 1 mTorr.

4.3.1 Silicon Nanowire Resonator Design

The silicon nanowire resonators described here were fabricated using the process described in the previous chapter on 275 nm thick silicon-on-insulator wafers. Polysilicon electrodes were designed to actuate higher-order nanowire bending modes to reach frequencies above 30 MHz, eliminating the need to aggressively scale the length of the nanowires for fundamental mode operation at similar frequencies. The nanowire resonators were either aligned with the wafer flat, for (110) nanowire sidewalls, or rotated 45 degrees with respect to the flat for (100) nanowire sidewalls. Two classes of nanowire resonators were designed. The first design consisted of single 2nd bending mode nanowires with lengths of 11 μm and 16 μm (Fig. 5A,B). The second resonator design consisted of a pair of parallel 3rd mode nanowires, 10 μm long, mechanically coupled by a third orthogonal nanowire, 7.8 μm long, similar in structure to the devices described in [21]. ANSYS 8 was used to determine the minimum length of the coupling

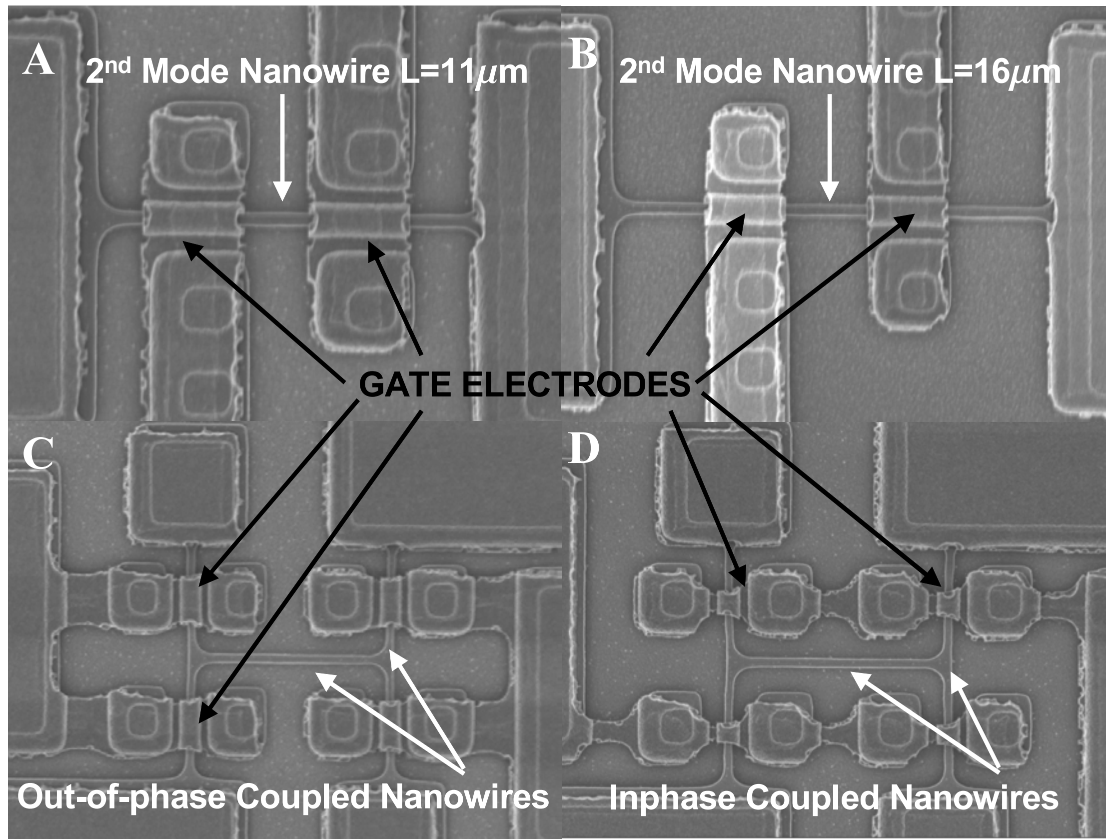

Figure 5. SEMS of the nanowire resonators. A) 11μm long 2nd mode single nanowire resonator. B) 16μm long 2nd mode single nanowire resonator. C) Out-of-Phase gate configuration for mechanically coupled nanowire resonators. D) In-phase gate configuration for the coupled nanowire resonators.

nanowire to satisfy the electrode spacing design rules developed for the fabrication process and to find the ideal locations for the gate electrodes. Two actuation configurations were designed for the mechanically coupled systems. Two pairs of polysilicon gate electrodes were shorted to induce either an out-of-phase (Fig. 5C) or an in-phase (Fig. 5D) vibration mode. Figure 6 shows the expected mode shapes for the coupled resonator systems depicted in Fig. 5.

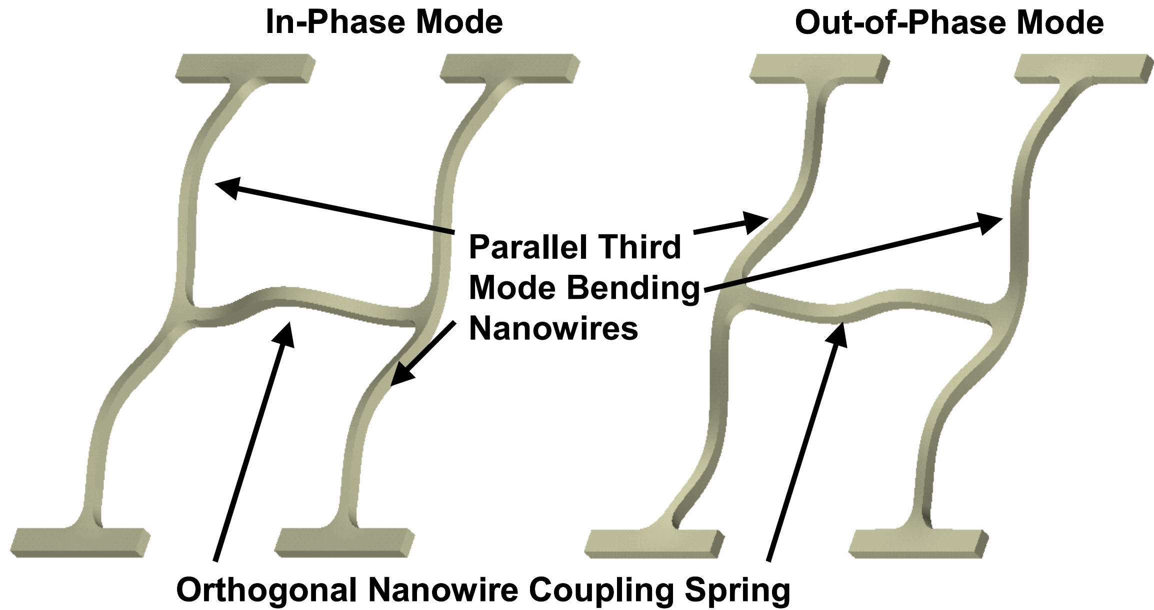

Figure 6. Expected mode shapes for the mechanically coupled nanowire resonators. For the in-phase mode (left) the parallel nanowires vibrate in phase and for the out-of –phase mode (right) the parallel nanowire vibrate out of phase which each other. The in-phase mode has a lower resonant frequency than the out-of-phase mode.

4.3.2 Polysilicon Gate Electrode Design and Device Operation

The gate electrodes surrounded the nanowire on three sides similar to the tri-gate electrode configuration reported in scaled field effect transistor papers [22,23]. If viewed in cross section, the polysilicon gate electrodes, highlighted in Fig. 5, partially overlap the lateral surfaces of the nanowire while completely overlapping the top surface of the nanowires (see Fig. 7). A conformal high temperature oxide (HTO) was deposited to create the lateral gaps resulting in a height mismatch between the nanowire and the adjacent regions of the gate (circled feature of Fig 7A). The vertical and lateral electrostatic gaps were 100 nm and 60 nm respectively.

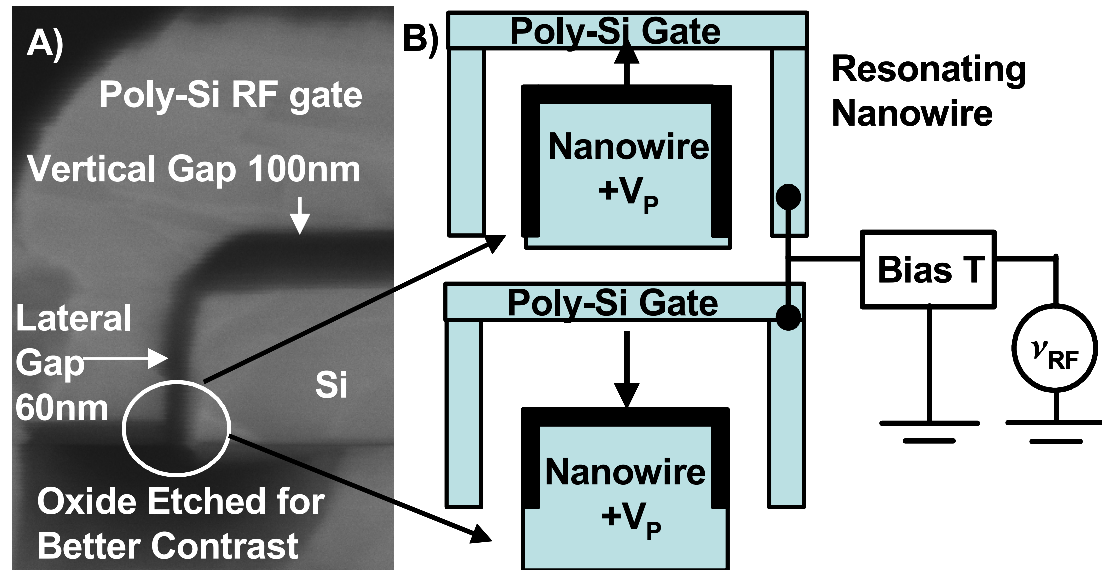

Figure 7. A) Cross-sectional SEM of a test structure depicting the dimensions of the air gaps between the silicon nanowires and the gate electrodes. Due to the conformal nature of the deposited sacrificial oxide the lateral regions of the gap do not line up with the bottom of the nanowire (circled feature). B) As the nanowire displaces the depletion region on the lateral surfaces of the nanowire grows (top) or shrinks (bottom) modulating the electrical cross-section of the nanowire resulting in a change in resistance. The arrows above the nanowire depict the direction of displacement towards the gate (top) and away from the gate (bottom).

When the nanowire is biased with a positive DC voltage, relative to the gate electrode, the surfaces of the n^+ doped nanowire deplete. The depletion regions are depicted in Fig. 7B by the black regions on the nanowire surface. When an RF signal, ν_{RF}, is applied to the polysilicon gate electrode the vertical region of the gate forces the nanowires into resonance while the lateral regions of the gate control the resistance of the nanowire. At

resonance the vertical displacement alters the electrical cross section of the nanowire resistor with advancing or receding depletion regions at both lateral surfaces of the wire (see Fig. 7B).

4.3.3 Measurement Equipment and Testing Approach

All of the resonant nanowire devices were tested at 1 mTorr in a Janis Research Probe Station. The probe station had one functional DC probe which was used to apply an RF signal and bias voltage to the one gate contact pad. The two functional RF GSG probes were used to bias the source and drain contacts while routing the RF current signal out from the resonating nanowires (see Fig. 8). For the device shown in Fig. 8, the gate contact on the right hand side of the figure was left floating since no other Janis probes were available to route an electrical signal or bias voltage to the remaining pad.

An Agilent Technologies E5071B Network Analyzer was used in the transmission measurement mode (S_{21}) to supply the RF forcing signal from port 1 to the gate electrode and detect the output signal directly from the nanowire resonator at port 2. The sensed output signals were averaged 16 times and saved.

Three wideband bias Ts, ZFBT-4R2GW from Minicircuits, Inc., along with three DC power supplies were used to bias the gate, source and drain terminals. The bias T at the source terminal was also used extract the output RF signal through the internal DC blocking capacitor.

An HP 4145B Semiconductor Parameter Analyzer equipped with Metrics ICS v. 3.7.0 software was used for DC characterization to demonstrate the depletion operation of released nanowires. An Andeen-Hagerling 2700A Capacitance Bridge, was used by Yu-Chih Tseng to measure the capacitance coupling the gate to source contact. The DC

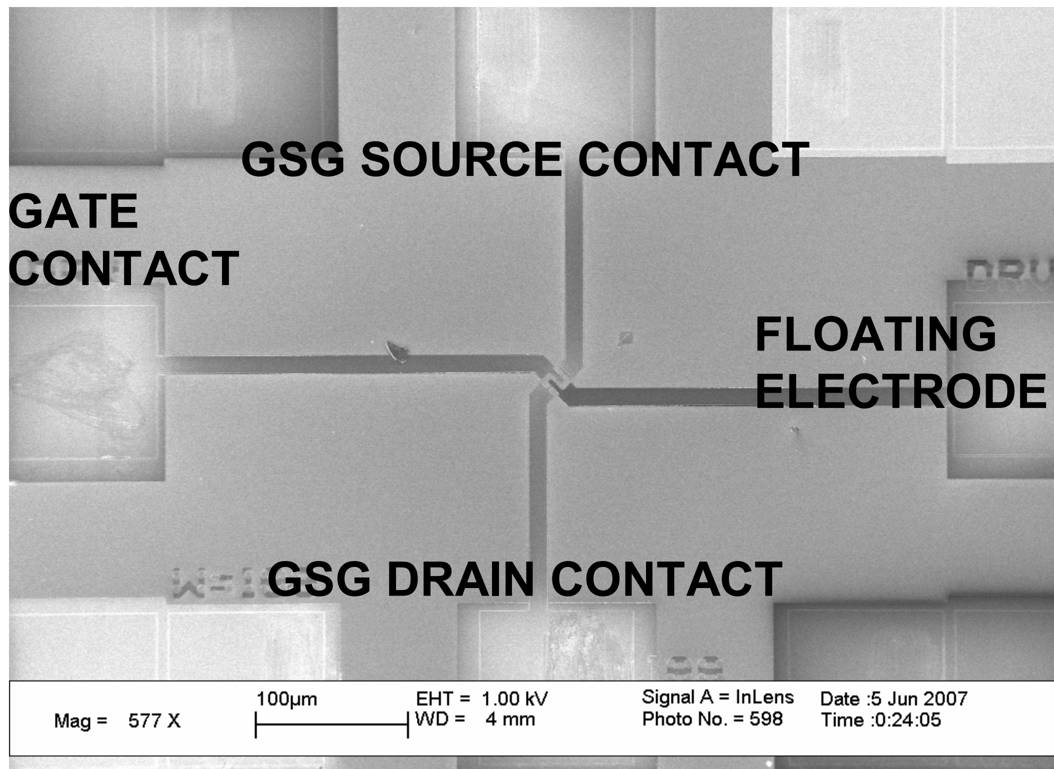

Figure 8. SEM of a (100) 16µm long 2nd mode nanowire resonator with GSG contacts. Note the gate contact on the left has a solitary scratch from the DC probe of the Janis probe station. GSG probes were used to make contact with the source and drain while the right gate contact was left floating.

measurements were performed in air at room temperature.

The devices were tested using both the field-effect configuration and the one-port capacitive sensing techniques. Figure 9 illustrates the field-effect testing approach. DC bias voltages were applied to both the source and drain pads through RF bias Ts to force a current through the nanowires. An RF signal, v_{RF}, from port one of a network analyzer was applied to the poly electrodes closest to the source contact. The RF current signal, due to resistance modulation, was detected out of the source contact and fed into the

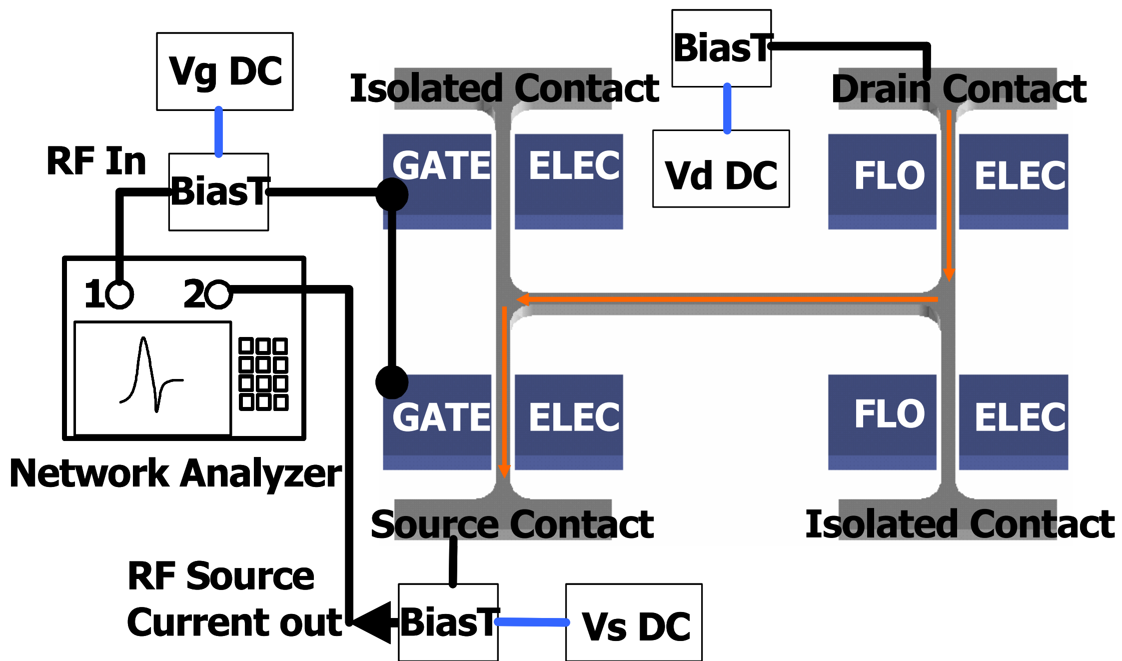

Figure 9. Testing configuration demonstrated on an out-of-phase mechanically coupled resonator shown in Fig. 5C. The region of gate covering wire is not depicted in the schematic. The gates labeled Flo Elec are left floating during the measurements. Electric current flows from the drain contact through the orthogonal wire and out of the source contact (orange arrows).

second port of a network analyzer. This is the same configuration used to probe the single nanowire resonators where one gate electrode is left floating (Fig. 8). Devices were tested as one-port capacitive resonators by disconnecting the bias from the drain contact, leaving the rest of the circuit intact, to confirm that the RF current signal detected at the source was due to a bulk nanowire resistance change and not due to a RF electrical current passing from the gate electrode to the resonating device.

4.4 Linear Out-of-Phase Resonator

The single nanowire resonators were the first devices tested using the field-effect sensing scheme, however, the S_{21} transmission measurements for the 2nd mode resonators were nonlinear. Attempts were made to extract the linear behavior of these devices by reducing the RF signal power and reducing the bias voltages applied to the electrodes, however, the linear behavior of the devices was never measured. On the other hand, the majority of the coupled nanowire resonators tested behaved linearly, enabling the estimation of quality factor and the creation of a model from first principles. The measured transmission signals (S_{21}) for the linear devices were fractions of a decibel due to the large capacitance coupling the source and gate contacts through the substrate. Figure 10 illustrates just how small the measured signals were for the out-of-phase

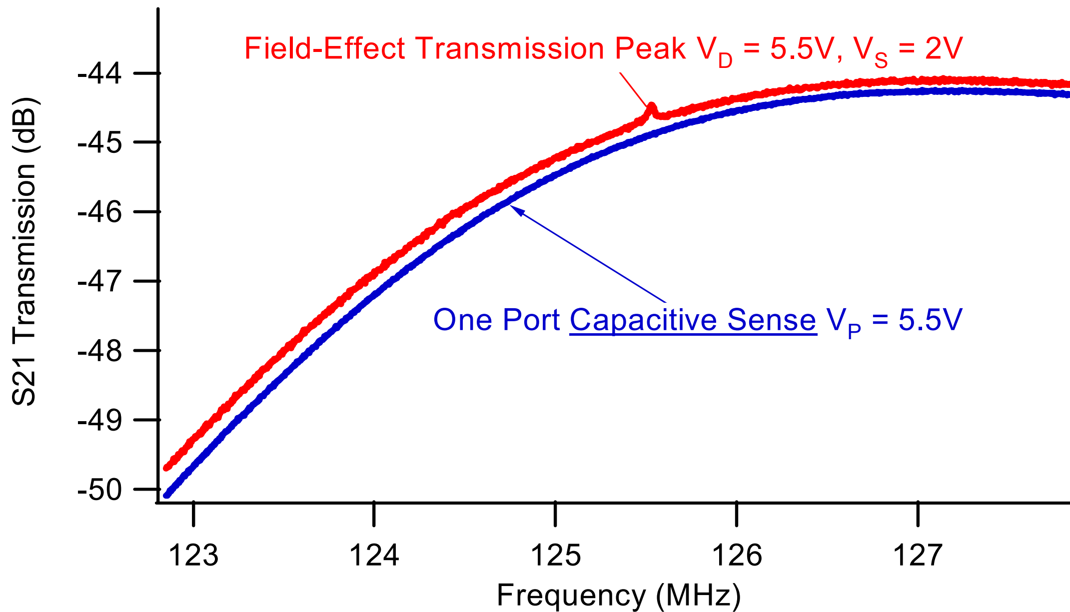

Figure 10. Example of the S_{21} transmission signal measured with the network analyzer with a frequency span of 5MHz. The input power for both the field-effect and one port capacitve sense measurements was -14dBm. V_G = 0V for both the field-effect and capacitive sense traces.

coupled devices.

Figure 11 is an SEM of the best performing out-of-phase coupled nanowire resonator (OP-A) tested which was aligned to the flat (110 sidewalls). The constituent nanowires of OP-A had widths of 280 nm and the gate electrodes were 2 μm long. The measured magnitude response for device OP-A is shown in Fig. 12. The field-effect testing technique produced a resonant peak at 124.14 MHz. The one-port capacitive measurement did not produce a detectable signal. For the one-port measurement, the frequency was scanned at 200 kHz intervals over a 20 MHz span centered at the resonant frequency of the field-effect measurement. The corresponding linear phase response for OP-A is shown in Fig. 13.

Since the field-effect resonant peaks were so small the quality factor was estimated by curve fitting the linear transmission response of OP-A using Origin 6.1 with a modified lorentzian function function given by:

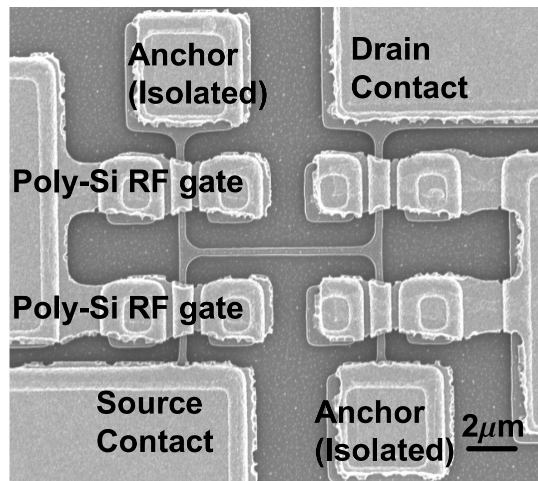

Figure 11. SEM of device labeled OP-A (out-of-phase A) with 280 nm wide nanowires.

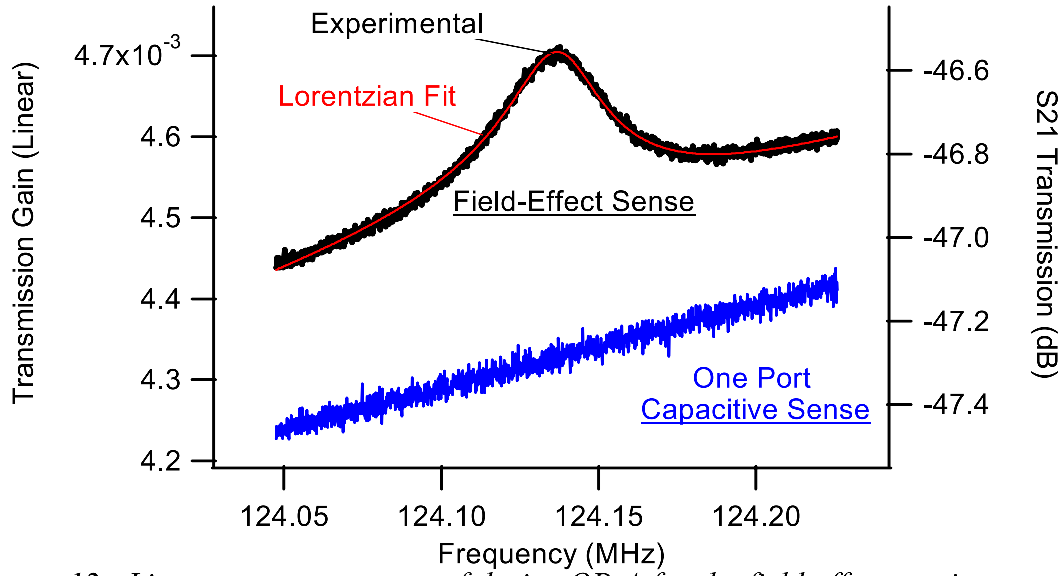

*Figure 12. Linear system response of device OP-A for the field-effect sensing approach with V_D=6.4V, V_S=2V, V_G=0V and P_{RF} = -14dBm and response for one port capacitive measurement with V_S = 6.4V, No V_D applied to drain contact, V_G=0V, P_{RF} = -14dBm. The response is given as the linear ratio of V_{OUT}/V_{IN} (left axis) and 20*log(V_{OUT}/V_{IN}) in dB on the right axis.*

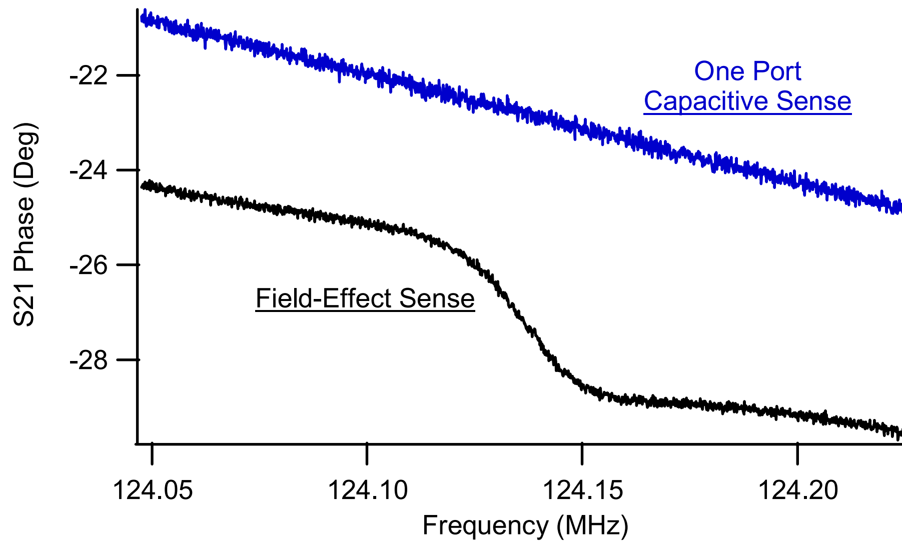

Figure 13. Measured phase response of OP-A for both the field-effect and capacitive testing approach under the same biasing conditions used for the magnitude measurements depicted in Fig. 12.

$$y = C_1 + C_2 f + \frac{(C_3 + C_4 f)}{\sqrt{\left(1 + 4\left(\frac{f - f_r}{w}\right)^2\right)}}$$

$$Q_f \approx \frac{f_r}{w}$$

where C_1, C_2, C_3, and C_4 are fitting constants which account for the y offset and sloping lorentzian curves, f is frequency, f_r is the resonant frequency corresponding to the maximum magnitude, and w is the width of the lorentzian. For the lorentzian fit shown in Fig. 12 the coefficients are: C_1 = -0.156, C_2 = 1.29E-9 /Hz, C_3 = 0.28, C_4 = -2.26E-9 /Hz, f_r = 124.14 MHz, and w = 30139 giving a correlation coefficient R^2 = 0.995, suggesting a good fit to the measured data. For device OP-A the fitted quality factor Q_f was estimated to be 4100.

4.4.1 Mode Verification

S_{21} transmission measurements were performed at the source and drain contacts to confirm the out of phase operation of device OP-A. When the device was tested using the exact configuration shown in Fig. 9, the black trace in Fig. 14 was recorded. Then the device was tested once more in the same configuration with one modification; the output RF signal was routed from the drain bias T to port 2 of the network analyzer (purple trace in Fig. 14). Figure 14 confirms that the two parallel nanowires of device OP-A vibrate out of phase relative to each other. Even though the polysilicon gate electrode closest to the drain was left floating for this measurement a resonant peak of 0.1 dB was detected by the network analyzer. It should be noted that the capacitive feedthrough from the source side gate electrodes to the drain contact pad was about 0.7 dB lower than the feedthrough coupling the source side gate electrodes to the source contact pad (Fig. 14).

The peak measured at the drain shifted to a slightly lower frequency due to the larger bias voltage applied to the drain terminal increasing the magnitude of the electrostatic spring.

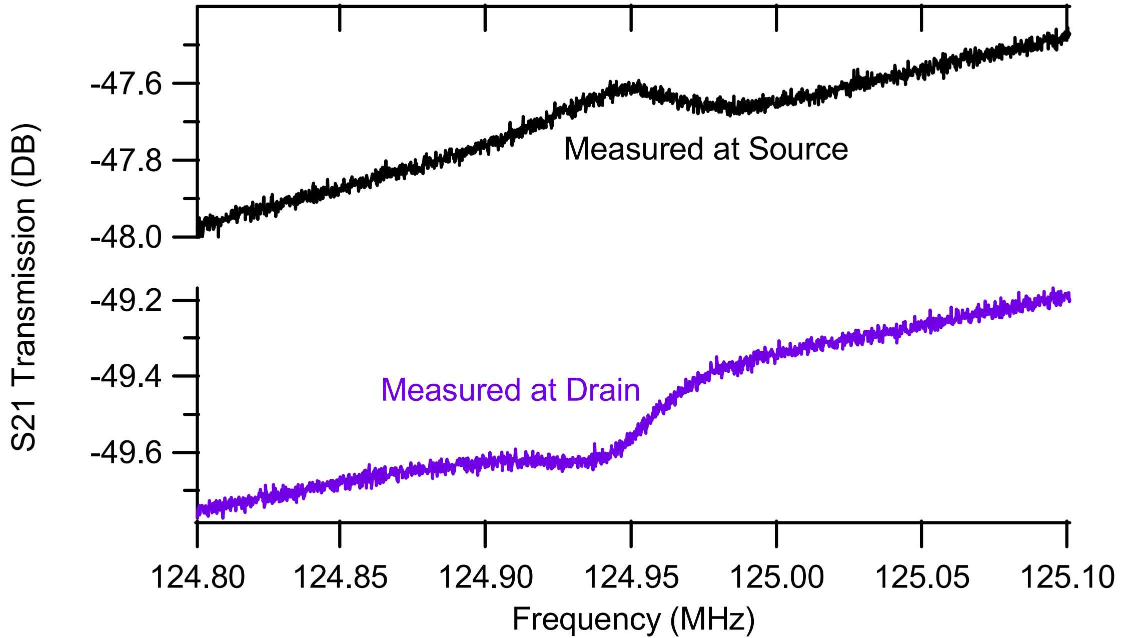

Figure 14. *Measured magnitude response of device OP-A using the resistance modulation technique.* V_D*=5.8V,* V_S*=2V,* V_G*=0V and* P_{RF} *= -14dBm for both traces.*

The measurements plotted in Fig. 14 were performed one week after the initial data, in Figs. 12 and 13 were recorded. The device was stored at room temperature in a hand pumped vacuum jar with anhydrous calcium sulfate to minimize moisture adsorption onto the device. However, compared to the initial measured response, it is obvious that the device response degraded in spite of the effort undertaken to minimize device exposure to air. Resonant peaks measured the week before at V_D = 5.5V were about 0.15 dB and sharper than the peaks recorded in Fig. 14.

4.4.2 Frequency Tuning

The resonant frequency can be tuned by either varying the DC bias voltage applied to the driving gate electrode, V_G (Fig. 15), or by varying the bias voltage applied to the drain, V_D (Fig. 16). At $V_G = +2.0V$ the resonant peak decreases in magnitude since $V_{GS} \approx 0V$, hence decreasing the driving force resulting in smaller nanowire displacement. At $V_G < 0V$, the resonance peak shifts to lower frequencies, due to electrostatic spring softening. The resonant frequency of the device changed by about 100 kHz/V for negative gate voltages (Fig. 15).

Only three distinct drain bias voltages were applied to device OP-A. The resonant frequency of OP-A decreased by about 1 MHz over $\Delta V_D = 1V$. More data points were taken on another device (OP-B) which was composed of 310 nm wide nanowires and had

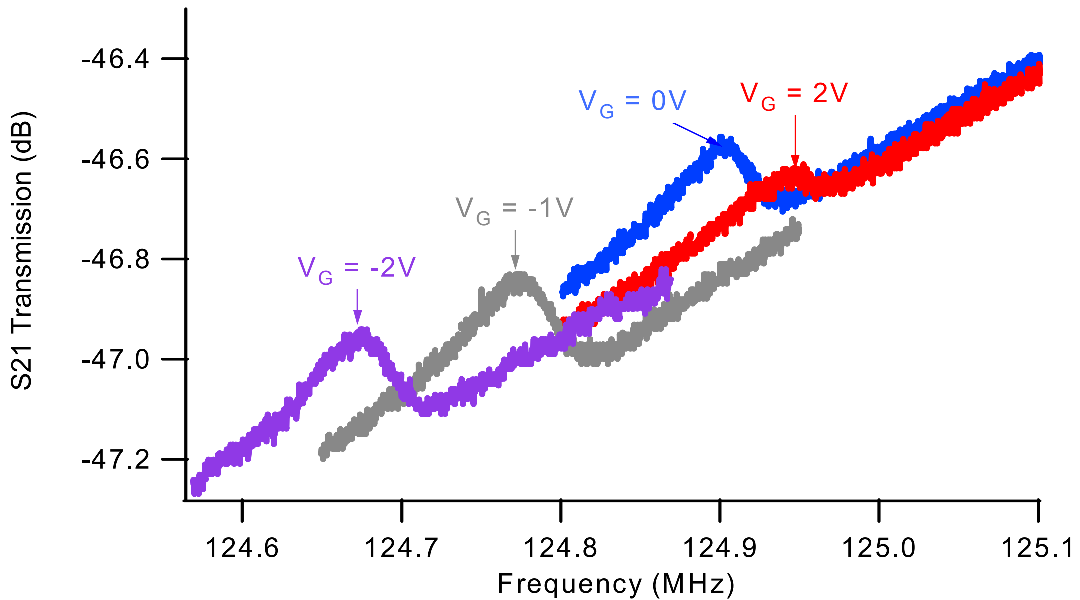

Figure 15. Resonant frequency tuning of nanowire system OP-A with $V_D = 5.8V$, $V_S = 2V$ for various values of V_G. At $V_G < 0V$, the resonant frequency of the device changed about 100 kHz/V.

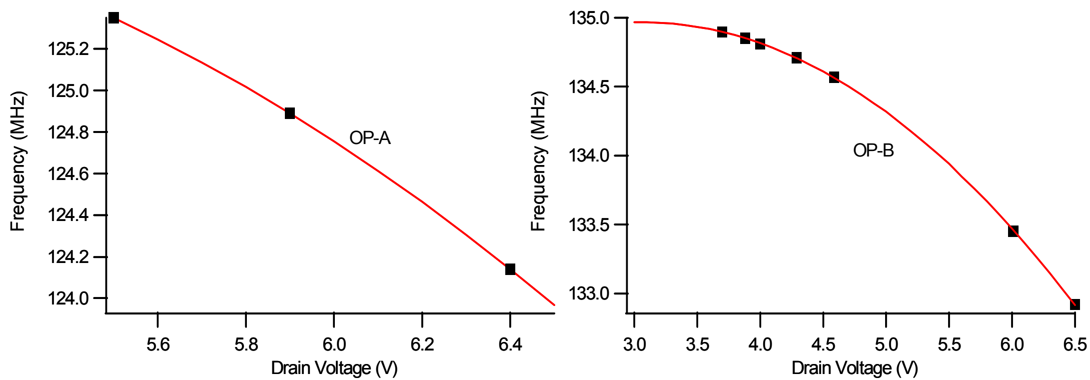

Figure 16. Resonant frequency tuning of nanowire systems OP-A (left) and OP-B (right). OP-B is composed of nanowires which are 310 nm wide. $V_S = 2V$*, and* $V_G = 0V$ *for both devices. Red traces are quadratic fitting curves for the data points (black).*

a larger resonant frequency than OP-A (see Fig.16). The results depicted in Fig. 16 give an idea of the variation in measured resonant frequencies from device to device. The lowest resonant frequency measured for an out-of-phase coupled system was 96 MHz.

4.4.3 DC Characterization

The coupled nanowire system, OP-A, was tested with DC bias voltages to extract the doping concentration within the wires and to demonstrate the depletion operation of the device (Fig. 17). The electric current was measured at the source, like the RF current signal, resulting in negative values for the DC current. The gate bias voltage, V_G, was applied to the pair of polysilicon electrodes on the left side of Fig. 11, while the electrodes on the right side of Fig. 11 were left floating similar to the RF measurement test setup shown in Fig. 8. As shown in Fig. 17, the gate tuned the resistance of the nanowire system. At $V_G = 0V$ and with $5V < V_D < 6.4V$ the resistance of the system was found to be 13.9 kΩ. Using the dimensions of the nanowires, the resistivity was

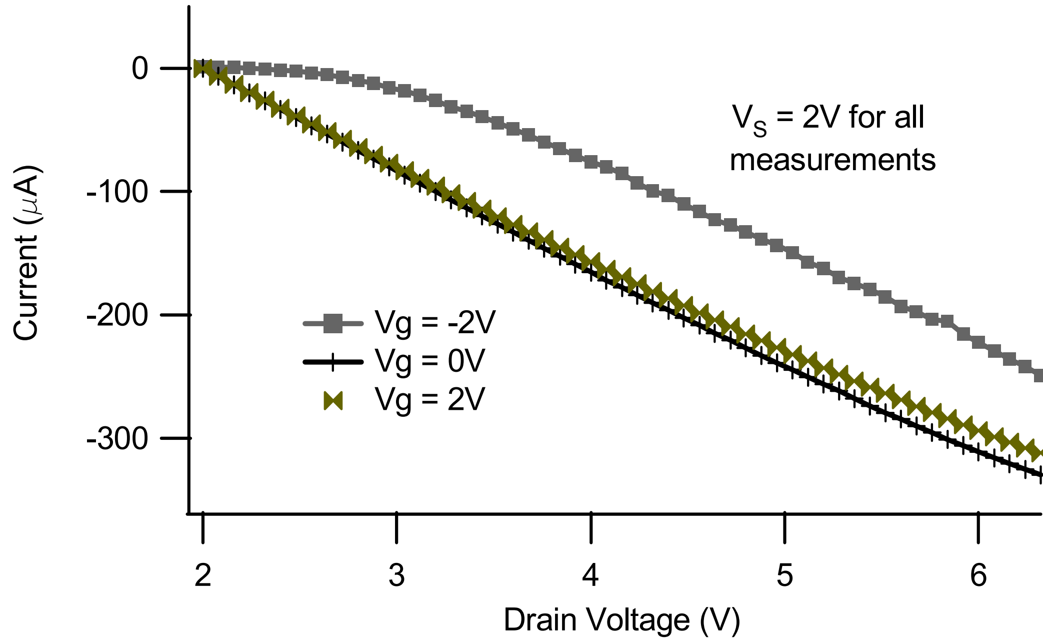

Figure 17. DC operation of the coupled wire system. The drain voltage was swept while V_S was held at a constant at 2V, to mimic the biasing conditions used for the field-effect RF testing scheme, and V_G was varied from -2V to 2V.

calculated, $6X10^{-3}$ Ω-cm, giving a phosphorus dopant concentration (N_d) of $8X10^{18}$ /cm^3.

CV measurements were performed to verify the depletion operation of OP-A. The bias voltages for these measurements were applied between the source contact and gate electrodes closest to the source. The source voltage was held constant at ground (V_S = 0V) while the gate voltage (V_G) was swept from negative to positive voltages at three frequencies. The capacitance bridge used to measure the CV characteristic of the device was limited to 20 kHz. The expected capacitance of OP-A is on the order of 10^{-16} F, however, the measured values were on the order of 10^{-12} F (Fig. 18). The CV response of OP-A was dominated by the capacitance coupling the source and gate contact pads through the lightly doped handle wafer. At V_{GS} = -2V, the average capacitance was

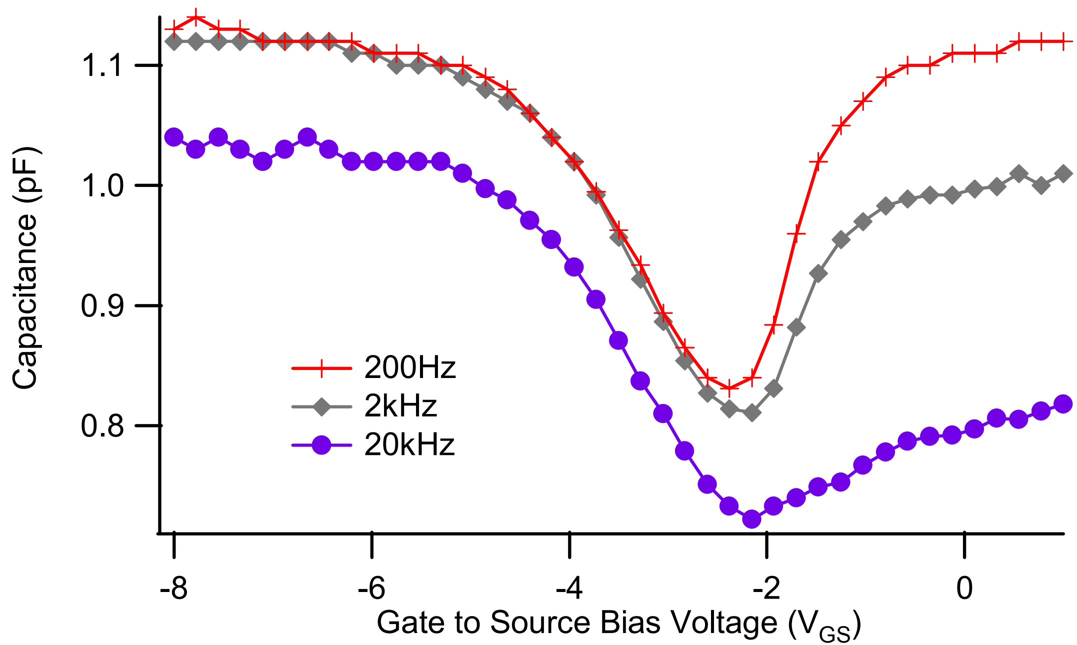

Figure 18. CV response of OP-A at 200 Hz (red), 2 kHz (grey), and 20 kHz (purple).

$8X10^{-13}$ F. The average capacitance was used to calculate an input resistance estimate of OP-A at 124 MHz to model the performance of the device, impedance = $1/(\omega_0 C)$. The impedance was then used to calculate the small signal RF voltage for -14dBm (500mV).

4.4.4 Model of Device OP-A

The resonant nanowire system was modeled in a quasi-static manner using the results from the resonant testing along with the resistance and capacitance of the system extracted from the DC measurements. First the system was analyzed in the mechanical domain by calculating the displacement of the nanowire system, at discrete L = 50 nm intervals, beneath the forcing gate electrode at resonance. The calculated displacement was then used in the electrical domain to determine the change in resistance as the

nanowire displaces up (towards the gate) and down (away from the gate) as shown in Fig. 7B.

4.4.4.1 Mechanical Domain Single 3rd Mode Nanowire Resonator

Ignoring the orthogonal coupling nanowire, the third bending mode of a single nanowire is described by the following expression:

$$\phi = \sin \beta x - \sinh \beta x + \alpha(\cosh \beta x - \cos \beta x) \quad (4)$$

$$\alpha = \frac{\sinh \beta_n L - \sin \beta_n L}{\cosh \beta_n L - \cos \beta_n L} \quad (5)$$

where ϕ is the modal displacement of the bending nanowire, $\beta_n L$ = 10.995 for the third bending mode, x is the location along the L = 10 μm nanowire. In this mode the left nanowire anchored at the source contact (Fig. 19) has maximum displacement points at 2.1 μm, 5 μm, and 7.9 μm relative to the source contact where x = 0 μm. The mechanical analysis will focus on the nanowire region between x = 1 μm to x = 3 μm where the gate

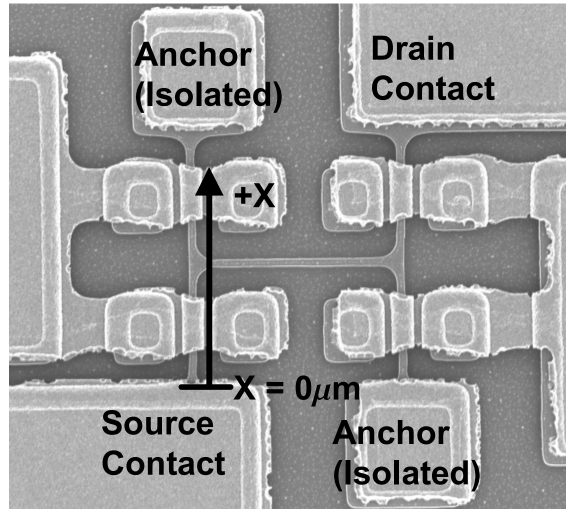

Figure 19. Reprinted from Fig. 11 with the position convention used for third mode mechanical model. x = 0 μm at the source contact.

electrode overlaps the region of the nanowire which was in the current path. The effective mass m_{eff} and the effective spring constant, k_{eff}, of a third mode beam at a given point x, along its length L, are:

$$m_{eff} = \frac{KE_{tot}}{\left(1/2\right)\dot{\phi}_X} = \rho W_{nw} H_{nw} \frac{\int_0^L \phi^2(x)dx}{\phi_X^2}, \quad k_{eff} = \omega_0^2 m_{eff} \tag{6-7}$$

where KE_{tot} is the kinetic energy of the bending nanowire, $\dot{\phi}_X$ is the modal velocity of the nanowire at particular point x along the length of the resonator, ϕ_X is the modal displacement of the nanowire at x, ρ is the density of silicon 2330 kg/m^3, W_{nw} (280 nm) and H_{nw} (275 nm) are the width and height of the silicon nanowire respectively, and ω_0 is the measured resonant frequency (124.14 MHz in Fig.12). Assuming the two lateral regions of the gate electrode are balanced electrostatically, the dynamic capacitive force applied by the gate electrode to the top surface of the nanowire at resonance, F_{res}, is:

$$F_{res} = \frac{V_{GS}\varepsilon_0 L_E W_{nw} v_{IN}}{d^2} \tag{8}$$

where V_{GS} is the dc bias voltage between the nanowire and the gate electrode, L_E is the length of the electrode (2 μm as fabricated), d is the dimension of the vertical gap between the electrode and the nanowire (100 nm from Fig. 7A), v_{IN} is the amplitude of the input RF voltage signal 500 mV, and ε_0 is the permittivity of free space. The harmonic displacement of the nanowire resonator, Y, is given by:

$$Y = \frac{QF_{res}}{k_{eff}} \tag{9}$$

where Q = 4100 from the lorenztian fit (Fig. 12). Since the nanowire system behaves as a linear resistor (Fig. 17), the average DC bias voltage at x = 2 μm is 2.5V under the

biasing conditions described in the caption of Fig. 12. V_{GS} = -2.5V, since the gate was grounded when the system was tested in the frequency domain. Using Eqs. (4)-(9) the displacement was calculated at 50 nm intervals from x = 1.00 μm to x = 2.95 μm. The maximum displacement of the third mode nanowire, calculated at x = 2.1 μm, was 5.3 nm.

4.4.4.2 Electrical Domain Single 3rd Mode Nanowire Resonator

In the electrical domain the gate electrode depletes the n^+ silicon under negative DC bias voltages, where $V_G < V_S$ (Fig. 20). The depletion region adds a second capacitor in series with the air gap capacitor, C_{gap}, separating the nanowire from the gate electrode (Fig. 20). The silicon depletion capacitance C_{De} is a function of the charge within the depletion region, Q_{De}, and the potential drop across it V_{De}. For the case shown in Fig. 20, the gate to source potential V_{GS} can be written as [24]:

$$V_{GS} = V_{gap} + V_{De} \tag{10}$$

where V_{gap} is the voltage drop across the gap between the electrode and the nanowire.

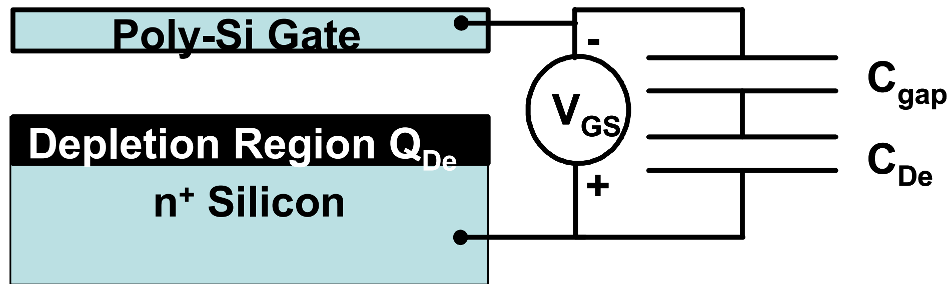

Figure 20. Adapted from [24] shows a generalized air-gap capacitor where the metallic polysilicon gate depletes n^+ doped silicon at negative bias voltages V_{GS}. The depletion region adds a second capacitor in series with the air gap capacitor separating the nanowire from the gate electrode.

The charge within the depletion region, Q_{De}, is now [24]:

$$Q_{De} = A\sqrt{2kT\varepsilon_0\varepsilon_{Si}F(V_{De})} \tag{11}$$

where A is the surface area of the capacitor, k is boltzmanns constant, ε_{Si} is the relative permittivity of silicon, T is temperature in Kelvin and

$$F(V_{De}) = p_0\left(\exp\left(\frac{-qV_{De}}{kT}\right) + \frac{qV_{De}}{kT} - 1\right) + N_d\left(\exp\left(\frac{-qV_{De}}{kT}\right) + \frac{qV_{De}}{kT} - 1\right) \tag{12}$$

where q is the charge of an electron, p_0 is the concentration of holes in the silicon assumed to be 10^{10} /cm^3, and N_d is the concentration of donors in the silicon [24]. The voltage drop across the gap can be rewritten as [24]:

$$V_{gap} = \frac{Q_{De}}{C_{gap}} = \frac{d}{\varepsilon_0}\sqrt{2kT\varepsilon_0\varepsilon_{Si}F(V_{De})} \tag{13}$$

which is substituted into Eq. (10) to arrive at an expression linking the voltage drop V_{GS} from gate to source to both V_{gap} and V_{De} [24]:

$$|V_{GS}| = |V_{De}| + \frac{d}{\varepsilon_0}\sqrt{2kT\varepsilon_0\varepsilon_{Si}F(V_{De})} \tag{14}$$

Equations (10), (12), and (14) were used to calculate V_{De} which was subsequently used to calculate the depletion length (X_{De}) from [24]:

$$X_{De} = \sqrt{\frac{2\varepsilon_0\varepsilon_{Si}V_{De}}{qN_d}} \quad . \tag{15}$$

As shown in Fig. 21, three regions of the polysilicon gate deplete the 2 μm long nanowire resistor segment, from x = 1 μm to x = 3 μm. Using N_d = 8X10^{18} /cm^3 and V_{GS} = -2.5V, the region of the gate above the nanowire depletes about 0.8 nm of the top nanowire surface, while the two lateral regions of the gate each deplete 1.0 nm of both lateral nanowire surfaces. At resonance the electrical cross-section of Resistor 1 and

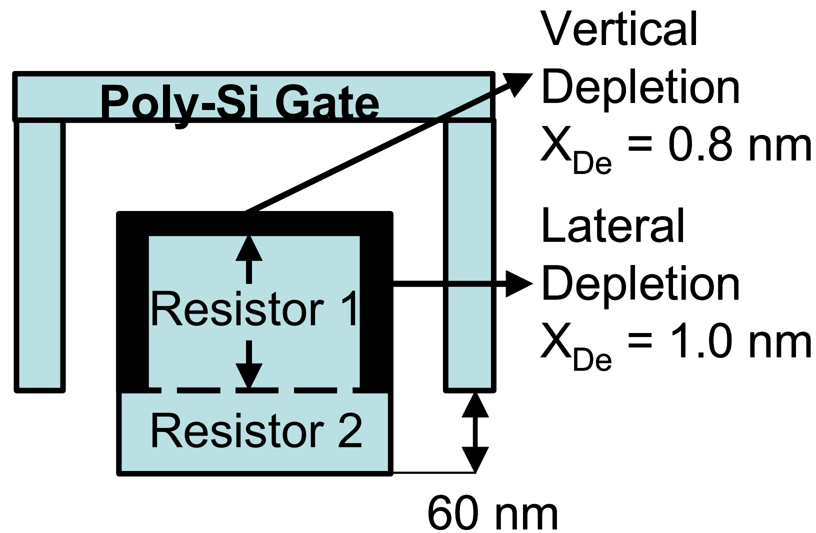

Figure 21. Cross-section of the nanowire resistor under the polysilicon gate electrode. Ignoring DC displacement due to V_{GS}, the top resistor (Resistor 1) has an electrical height of 214 nm and an electrical width of 278nm where the depletion dimensions were subtracted from the physical dimensions of the wire. The bottom resistor (Resistor 2) has an electrical height of 60nm and an electrical width of 280nm. Resistor 1 is in parallel with Resistor 2.

Resistor 2 change, as shown in Fig. 7B, modulating the resistance of the nanowire. The 2 μm long resistor was broken up into 50 nm long segments (Fig. 22) to match the displacement intervals used in the mechanical analysis, from x = 1.00 μm to x = 2.95 μm. For the first half cycle of resonance where the wire displaces up, towards the gate, the values of Resistor 1 and Resistor 2 were calculated to the nearest Ohm using the displacement from the mechanical domain analysis to adjust the electrical dimensions of Resistor 1 and 2. For example, if a 50 nm long segment was calculated to have a

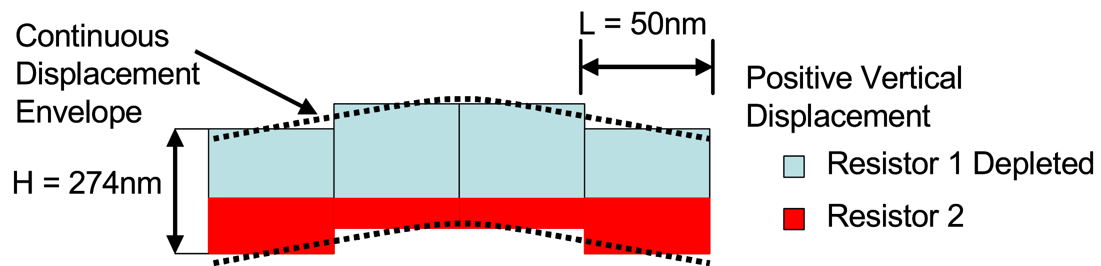

Figure 22. 2 μm long resistor depicted displacing up towards the gate broken up into 50 nm segments (not drawn to scale and vertical displacement is exaggerated). The blue regions represent Resistor 1 and the red regions represent Resistor 2. The dashed lines are the continuous displacement envelope of the nanowire resinator, using eqs. (4-9), for the 2 μm long region modeled. The heights of Resistor 1 and Resistor 2 vary along the length of the 2 μm resistor. The height given on the left of the figure is the physical height minus the vertical depletion region depicted at the top surface of Fig. 21.

displacement of 2 nm, towards the gate in the mechanical domain, the cross sectional area of Resistor 2 and Resistor 1 was calculated to be 58*280 nm^2 and 216*278 nm^2 respectively. The resistivity extracted from the DC characterization was used to calculate the value of each resistor:

$$R_{1,2} = \frac{\rho L_S}{Area_{1,2}} \tag{16}$$

where L_S = 50nm and $Area_{1,2}$ is the respective area of Resistor 1 and 2. For each 50 nm segment the total resistance was calculated as the parallel combination of Resistor 1 and Resistor 2 and rounded to the nearest Ohm. Finally all 50 nm long segments were added in series. This procedure was then repeated for next displacement half cycle (away from

the gate). The quasi-static resistance, for a single third mode wire, was found to be R_{TUP} = 1574 Ω, for up state, and R_{TDOWN} = 1579 Ω for the down state.

At V_D = 6.4 and V_S = 2V the voltage drop across the 2 μm nanowire segment, $V_{2\mu m}$, was calculated to be 0.5V using:

$$V_{2\mu m} = (2\,\mu m)\left(\frac{V_D - V_S}{17.8\,\mu m}\right) \tag{17}$$

assuming a linear resistor where 17.8 μm is the length of the path from drain to source. Employing the quasi-static approach the voltage drop, 0.5V, across the 2 μm long nanowire resistor was assumed to be constant for both resistor states (up and down). The RF signal current, i_{RF}, was calculated as the difference in current between the two resistance states:

$$i_{RF} = \left(\frac{V_{2\mu m}}{R_{TUP}}\right) - \left(\frac{V_{2\mu m}}{R_{TDOWN}}\right), \tag{18}$$

usually on the order of 1 μA. The RF signal current was then multiplied by the 50 Ω internal resistor found at the second port of the network analyzer (Fig. 23), to calculate the small signal voltage, v_{RF}. The small signal voltage was calculated to be 50μV for the

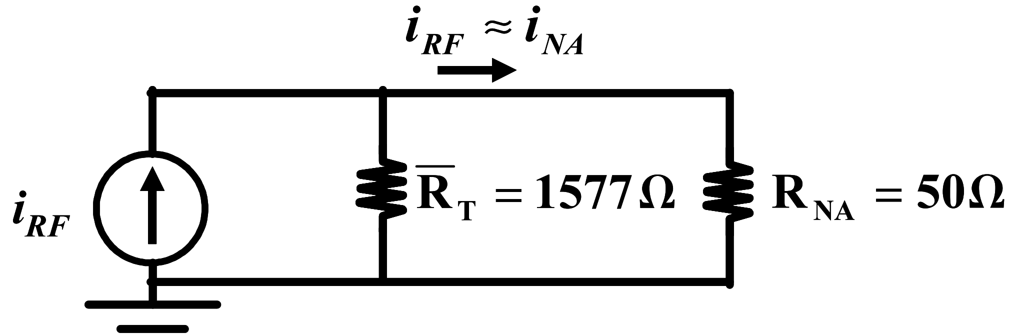

Figure 23. Small-signal circuit approximation of resonant nanowire resistor. $\overline{R}_T$ *is the average resistance of* R_{TUP} *and* R_{TDOWN}. R_{NA} *is the 50 Ω load resistor within port 2 of the network analyzer.*

single third mode wire model. The linear transmission gain, Fig. 12 along with the fitting function, were used to extract the output voltage measured by the network analyzer, estimated to be 79 μV. The RF voltage, v_{RF}, was underestimated by the model since the previous mechanical analysis ignores the stiffness contribution from the nanowire mechanically coupling the two resonators. To estimate this stiffness contribution a harmonic analysis was done using an ANSYS 11 finite element model.

4.4.4.3 ANSYS 11 Finite Element Mechanical Model for Device OP-A

The dimensions of the beams were extracted from SEM images. Solid structural elements 186 were used to construct the mechanical model. The silicon density was $2.333\text{X}10^{-15}$ kg/μm^3 in μMKS units and the stiffness matrix, C, for OP-A was calculated using the procedure outlined in [25] to orient X and Y as {110} surfaces while retaining Z as a {100} surface:

$$C = \begin{pmatrix} 19.5 & 3.5 & 6.4 & 0 & 0 & 0 \\ 3.5 & 19.5 & 6.4 & 0 & 0 & 0 \\ 6.4 & 6.4 & 16.6 & 0 & 0 & 0 \\ 0 & 0 & 0 & 8.0 & 0 & 0 \\ 0 & 0 & 0 & 0 & 8.0 & 0 \\ 0 & 0 & 0 & 0 & 0 & 5.1 \end{pmatrix}$$

each element in the matrix is multiplied by 10^4 yielding units of MPa for the μMKS scheme. Finally, a constant damping ratio (1/2Q) was used for the ANSYS model where Q = 4100 from the lorentzian fit (Fig. 11). F_{res} from Eq. (8) was applied to the top surface of the source nanowire from x = 1 μm to x = 3 μm (Fig. 24).

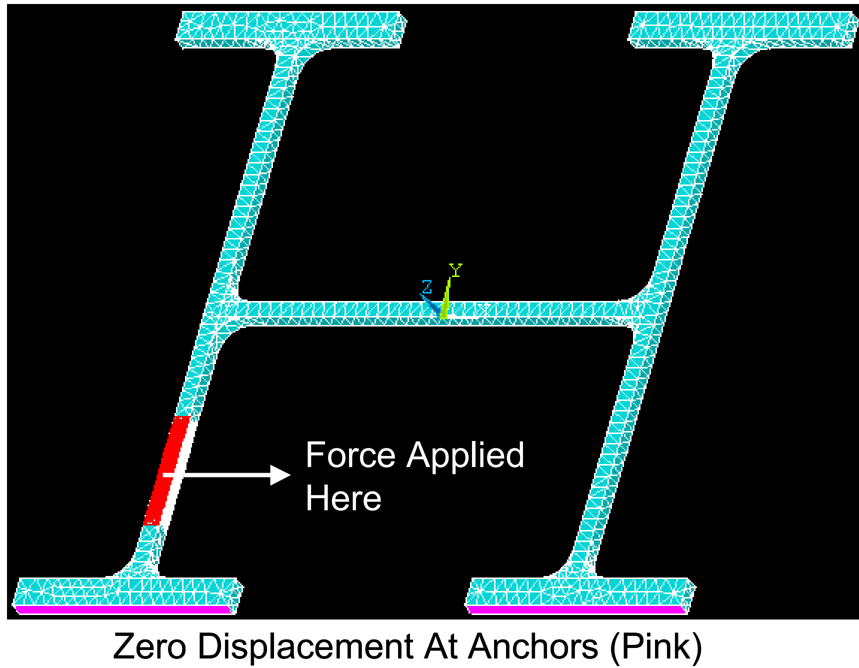

Zero Displacement At Anchors (Pink)

Figure 24. Captured image from ANSYS 11 depicting the loading scheme for the harmonic analysis. The pink colored features represent the anchor boundary condition applied to the model. The corresponding anchor boundary conditions on top side of the figure are symmetric.

The resonant frequency of the ANSYS simulated system was about 125.1 MHz. The mechanical displacements calculated by ANSYS were extracted at 50 nm intervals. The calculated ANSYS displacement for each 50 nm long segment was then corrected by a multiplication factor which modeled electrostatic spring contributions. Assuming equal effective masses for each data point of Fig. 16 the spring multiplication factor can be extracted by the ratio of resonant frequencies. For example:

$$f_1 = \sqrt{\frac{k_1}{m_{EFF}}},\ f_2 = \sqrt{\frac{k_2}{m_{EFF}}} \qquad (16\text{-}17)$$

$$\left(\frac{f_2}{f_1}\right)^2 = \frac{k_2}{k_1} \quad . \tag{18}$$

where $f_1 > f_2$, $k_1 > k_2$, $f_\#$ and $k_\#$ are the resonant frequency and effective spring constant for two distinct V_D bias points. For the data given in Fig. 16 the spring ratio ranged from 0.99 to 0.97 for device OP-B. The relative electrostatic spring correction factor increased the ANSYS calculated displacements by about 0.1 nm for each discrete 50 nm segment.

The maximum displacement at x = 2.1 μm was found to be 2 nm for the new ANSYS-based mechanical model as opposed to 5.3 nm using the third mode nanowire model. The total resistance calculated for both up and down states, based on the ANSYS mechanical model, were R_{TUP} = 1560 Ω and R_{TDOWN} = 1569 Ω. The calculated RF signal current, i_{RF}, was 1.8 μA yielding a RF signal voltage of 92 μV, which is 12 μV larger than the extracted 79 μV. The ANSYS model was then used to model OP-A at two more drain bias voltages. The results are summarized in Table 1.

V_D (V)	v_{RF} Extracted	R_{TUP} (Ω)	R_{TDOWN} (Ω)	$V_{2\mu m}$ (V)	Modeled v_{RF}
5.5	76 μV	1560	1572	0.4	98 μV
5.9	88 μV	1560	1571	0.44	99 μV
6.4	79 μV	1560	1569	0.5	92 μV
Average	81				96
STD	6.2				3.8

Table 1. Comparison of v_{RF} extracted from the measured transmission data and ANSYS based v_{RF} model results at three drain bias voltages.

4.4.4.4 OP-A Model Discussion and Limitations

The v_{RF}, extracted from the transmission data, was relatively stable with an average of 81 μV and a standard deviation of 6 μV (Table 1). The discrete ANSYS based model predicts an average v_{RF} of 96 μV with a standard deviation of 4 μV. The predicted RF signal differs from the measured RF signal by an average of +15 μV. The modeled RF output voltage, v_{RF}, is heavily dependent on resonator displacement since the 3rd mode mechanical model overestimated the displacement resulting in a v_{RF} = 50 μV and the ANSYS mechanical model underestimated resonator displacement producing a v_{RF} of 92 μV. The actual displacement for OP-A must be slightly higher than the ANSYS model predicts.

The electromechanical model used to describe the performance of OP-A has the following limitations:

1. The large parasitic capacitance negates the ability to directly measure quality factor from the measured signals using the 3dB requirement typically used for MEMS resonators.
2. The input resistance was estimated using the measured parasitic capacitance, shown in Fig. 18. The estimated input resistance was subsequently used to calculate the output voltage from the S_{21} transmission measurements.
3. The discrete modeling approach inevitably results in rounding errors for both displacement and resistance which may increase or decrease the modeled signal level.
4. Second order effects were ignored (e.g. resistivity gradients within nanowires, residual stress from the nitride anchors and high phosphorus doping levels).

However, the piecewise linear electromechanical model does provide a plausible explanation for the origin of the RF signal sensed with the network analyzer since the model results and the results from the data are on the same order of magnitude and only differ by an average of 15 microvolts.

4.4.5 OP-A Transconductance Calculation

The transconductance of device OP-A was calculated using only the measured S_{21} linear magnitude (Figs. 12 and 25) and phase (Figs. 13 and 26) because the other S parameters could be ignored (see Appendix B). Although OP-A did not operate as a transistor, the calculation procedure outlined in Appendix B was adapted from [27]. The transconductance of OP-A was calculated using Eqs. (B.2),(B.5),(B.7) and (B.9) from Appendix B. The absolute value of the peak transconductance calculated for OP-A was $7.2X10^{-6}$ S (Fig. 27).

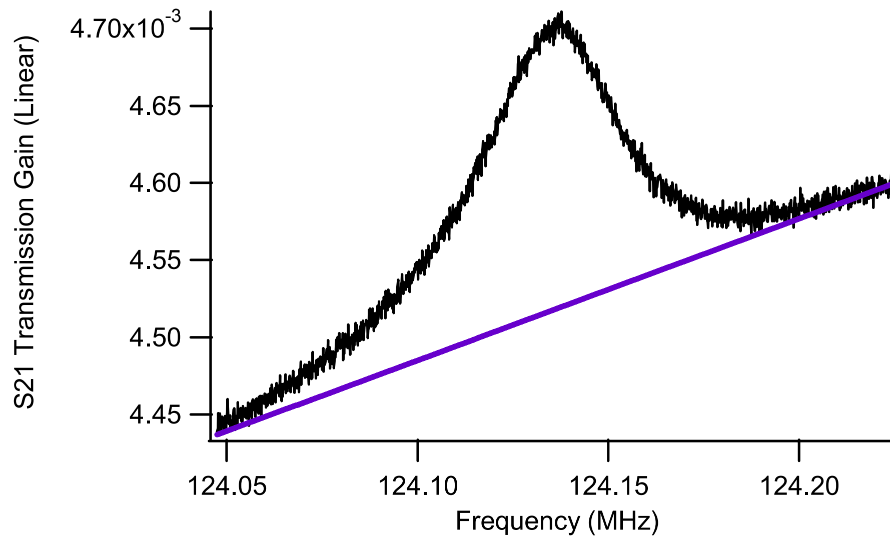

Figure 25. S_{21} linear magnitude of device OP-A (black trace) and estimated field-effect feedthrough magnitude (purple trace) from Fig. 12.

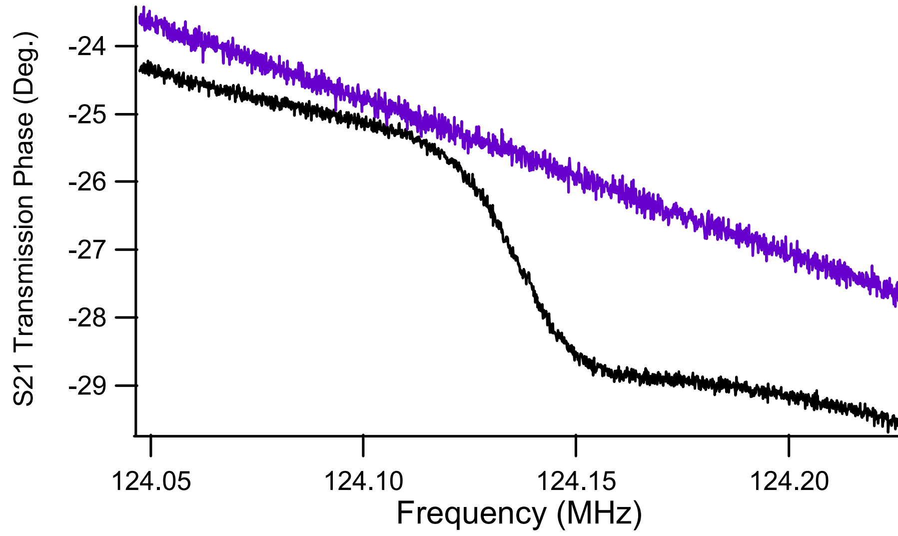

Figure 26. S_{21} phase of device OP-A (black trace) and estimated field-effect feedthrough phase (purple trace).

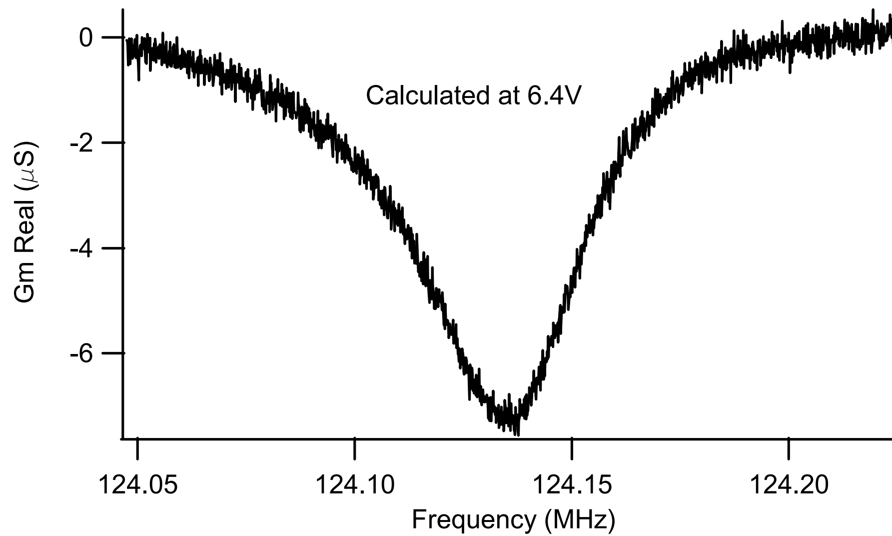

Figure 27. Calculated transconductance of device OP-A as a function of frequency. The transconductance is negative because of the definition used in Appendix B.

The calculated transconductance (Fig. 27) was about two times larger than the g_m estimated using the definition for solid-state devices:

$$g_m \equiv \frac{\partial I_D}{\partial V_G} \approx \frac{\partial I_S}{\partial V_G} \approx \frac{i_{RF}}{v_G} \tag{19}$$

where i_{RF} is the extracted or modeled small signal current from section 4.4.4 and v_G = 500mV. For V_D = 6.4V, V_S = 2V, V_G = 0V, and v_{RF} = 500mV Eq. (19) gives g_m = 1.6 μA/500mV or 3.2X10^{-6} S. The g_m for the ANSYS based model, for the same biasing conditions, was calculated to be 1.8 μA/500mV or 3.6X10^{-6} S. Equation (B.9) from Appendix B multiplied the real component of S_{21} by 2 accounting for the factor of two difference with respect to the results obtained from Eq. (19).

4.5 Nonlinear Nanowire Resonators

The remaining nanowire resonators tested were nonlinear, including the in-phase coupled nanowire resonators. Both the S_{21} transmission magnitude measurements and the corresponding phase measurements confirmed the nonlinear behavior of the devices.

4.5.1 (100) Nonlinear Coupled Resonators

The nonlinear response of both the in-phase and out-of-phase coupled nanowire resonators oriented at a 45-degree angle from the flat was the direct result of the polysilicon gate electrode geometry. The polysilicon gate electrodes for these devices were purposely designed to have lengths of 1 μm. Gate electrode misalignment coupled with the SF_6 plasma over-etch step contributed to the creation of asymmetric lateral gates for both the (100) coupled resonators, in-phase and out-of-phase devices (Fig. 28).

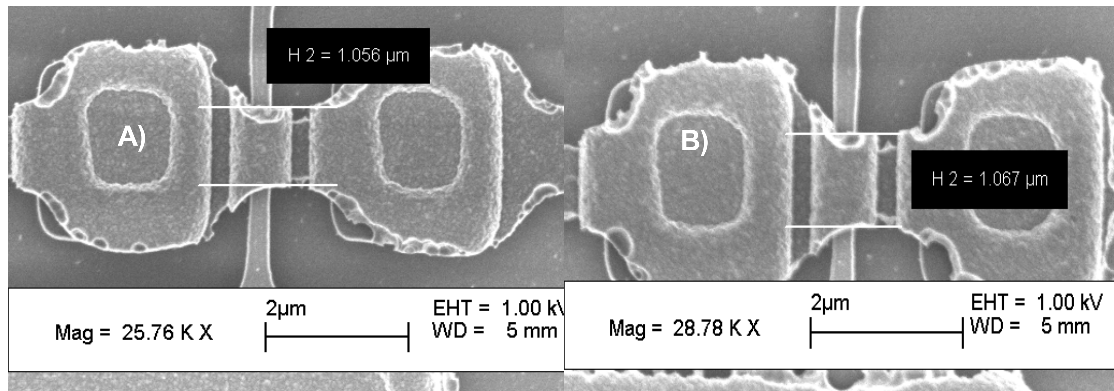

Figure 28. Polysilicon gate electrodes for A) (100) in-phase coupled resonator and B) (100) out-of-phase coupled resonator. The devices were located next to each other on the same die.

Figure 29 shows the measured S_{21} transmission response for the out-of-phase device with 260 nm wide nanowires and an in-phase device with similar width nanowires. The phase response for each (100) device was no longer as smooth as the phase response for OP-A (Fig. 13) suggesting a likely transition into nonlinear operation for both devices. It should also be noted, from Fig. 29, that the resonant frequency of the in-phase device, 110 MHz, was larger than the out-of-phase coupled device, 108 MHz, even though the in-phase device was biased at a larger V_D. A modal analysis was performed on ANSYS 11 assuming 260 nm wide nanowires and using the (100) stiffness matrix for Silicon. The resonant frequency was calculated to be 104.3 MHz for the in-phase mode and 111.8 MHz for the out-of-phase mode. ANSYS also predicts a distinct in-plane mode at 111.9 MHz (Fig. 30) which has roughly the same resonant frequency as the out-of-phase mode. Since the gate electrodes for the both in-phase and out-of-phase

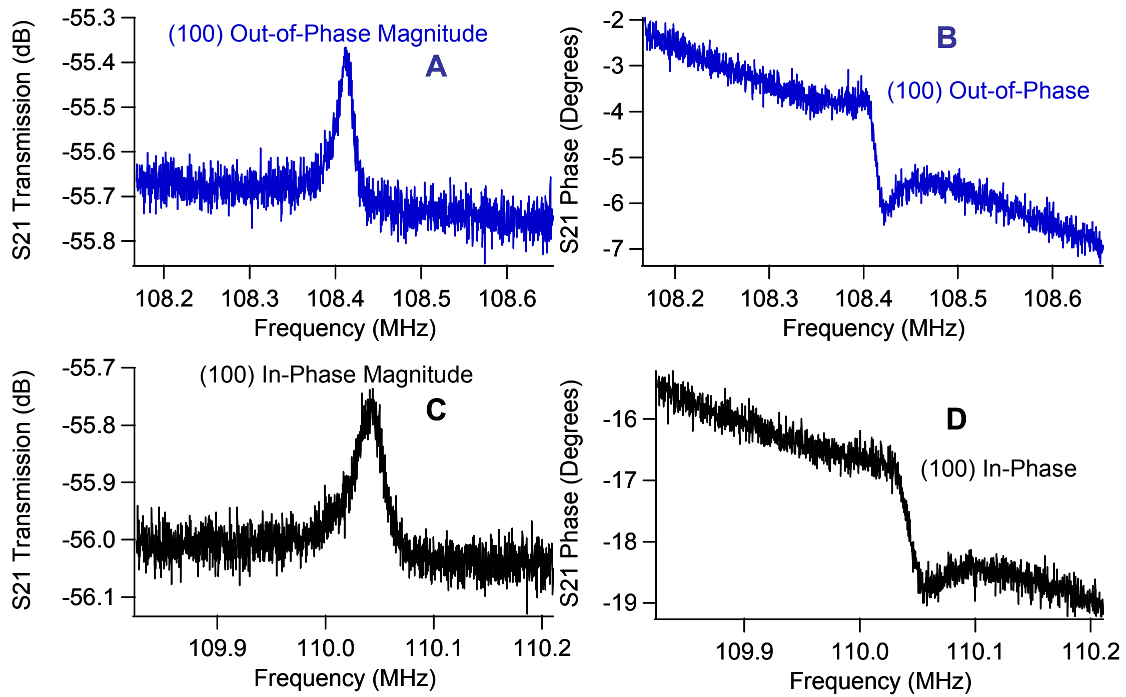

Figure 29. A) Magnitude response and B) Phase response of (100) Out-of-Phase resonator with V_D = 5.7V, V_S = 2V, V_G = 0V, and P_{RF} = -14dBm. C) Magnitude response and D) Phase response of (100) In-of-Phase resonator with V_D = 6V, V_S = 2V, V_G = 0V, and P_{RF} = -14dBm.

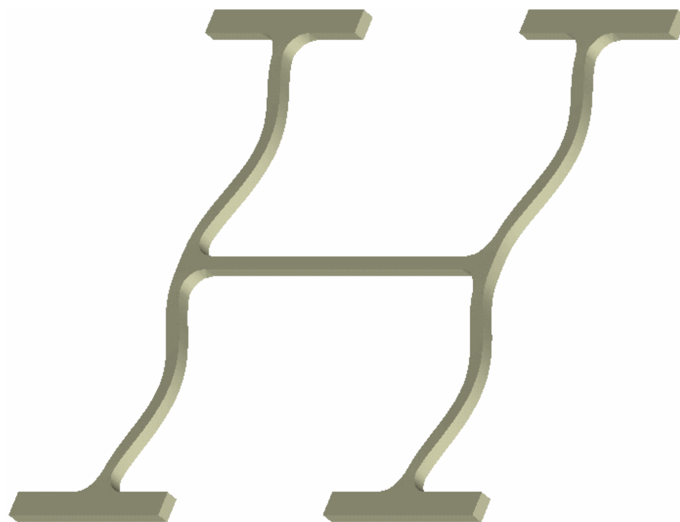

Figure 30. In-plane mode predicted by ANSYS 11 for 260nm wide (100) coupled nanowires.

devices were laterally asymmetric, the in-plane mode might have been actuated for both devices. The nonlinear behavior and the measured resonant frequencies of both devices also hint at the in-plane resonant mode. Further testing to confirm this conclusion was not possible since the out-of-phase device was destroyed during testing. SEMs later confirmed that the coupling nanowire was destroyed by the current passing through the device, see Fig. 31. The (100) in-phase device no longer functioned after imaging the device with the SEM, which may have been due to electrons charging the isolated SOI nanowires during imaging.

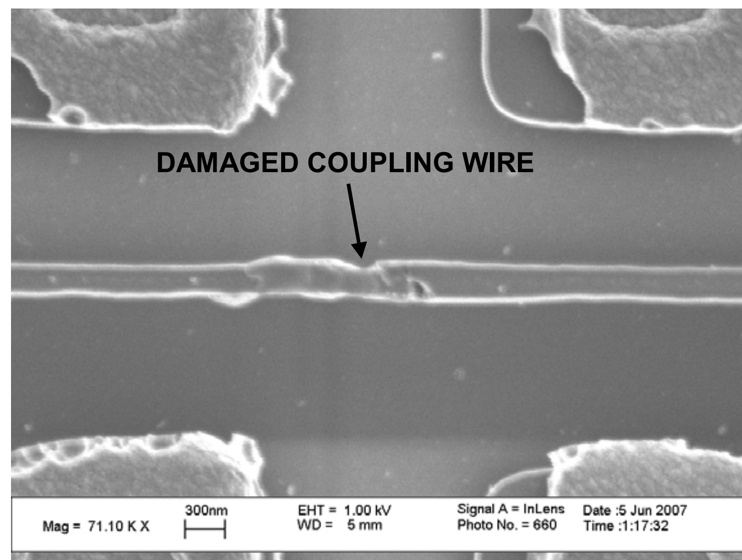

Figure 31. Damaged coupling wire of the (100) out-of-phase device. The conduction path from the source to drain was severed.

4.5.2 Nonlinear 2nd Mode Nanowire Resonators

The second mode nanowires resonators were the first devices tested using the field-effect resistance modulation measurement technique. The S_{21} transmission response of these devices was extremely nonlinear.

A 11 μm long 2nd mode device was first tested as a two port capacitive resonator (Fig. 32) up to 40 MHz. Two gate electrodes, separated by 1.9 μm, were used to force and sense the displacement of the nanowire capacitively (Fig. 32) while the nanowire was biased at 8V. Only one very small resonant peak was detected within the 40 MHz frequency span at an input power of -7dBm (Fig. 33A). The large capacitive feedthrough overwhelmed the two port capacitive signal from the vibrating nanowire. Then the field-effect testing technique was performed on the same device with V_D = 3V, V_S = 2V, and V_G = 0V with P_{RF} = -10dBm. Figure 33B shows the measured transmission response for the field-effect measurement in which two nonlinear peaks were detected. The first field-effect peak (Fig. 33C) was measured at the same resonant frequency as the two port capacitive peak coinciding with the (100) fundamental mode at 19.2 MHz, predicted with

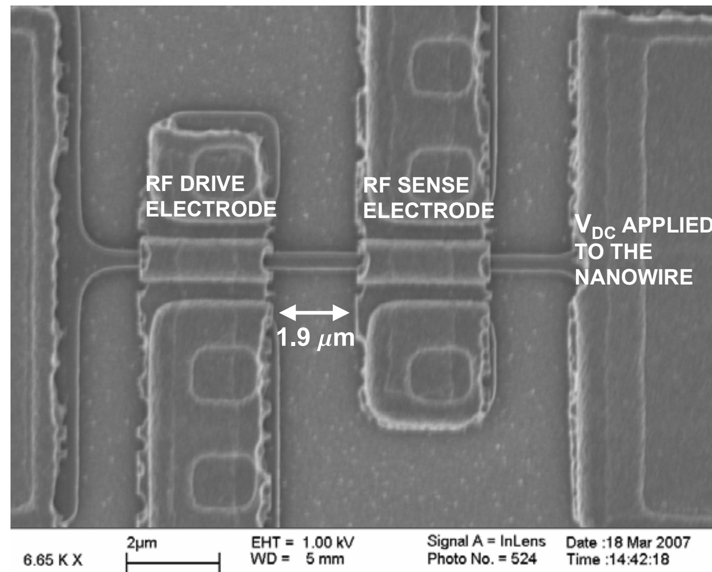

Figure 32. Two port capacitive test set-up for the first 2nd mode nanowire resonator tested. The nanowire for this device was aligned with the flat for (110) sidewalls and was 380 nm wide and 11 μm long.

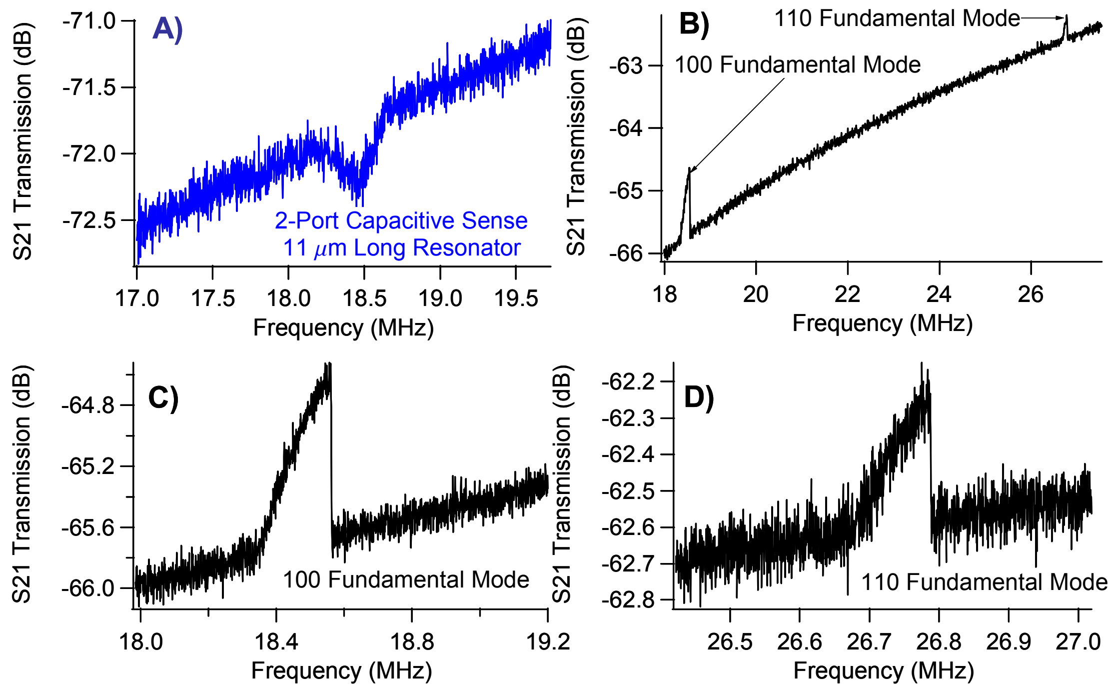

Figure 33. A) Two port capacitive S_{21} Transmission Magnitude for V_{DC} = 8V and P_{RF} = -7dBm. B) Field-Effect S_{21} Transmission Magnitude for V_D = 3V, V_S = 2V, V_G = 0V, and P_{RF} = -10dBm. C) A close up of the first field-effect peak shown in (B). D) A close up view of the second resonant peak measured in (B).

an ANSYS modal analysis. The field effect measurement of the first mode had a larger magnitude than the two port capacitive measurement even though the feedthrough was larger for the field-effect measurement. The second resonant peak (Fig. 33D), from the field-effect measurement shown in Fig. 33B, coincides with the (110) fundamental mode at 28.1 MHz predicted with ANSYS. The measured (110) fundamental mode may be the result of unequal lateral gap spacing on either side of the nanowire resonator since there was no visible gate asymmetry in Fig. 32 similar to the gate asymmetry shown in Fig. 25.

After compiling the data, from Fig. 33, it was realized that the resonant 2nd mode frequency was outside of the target 40 MHz span initially used for both the two port capacitive and field-effect measurements. The device was subsequently tested in the field-effect configuration at frequencies above 40 MHz. The resonant frequency of the 2nd mode was measured at 53 MHz, moreover, the device was exhibiting tapping mode behavior similar to the work reported in [26] (Fig. 34). V_D and P_{RF} were decreased to measure the linear magnitude response of the device, however, all attempts to extract the linear response were unsuccessful. After the device was imaged with the SEM to extract the nanowire dimensions, it no longer operated. All subsequent 2nd mode nanowire resonators were tested using the field-effect technique because the output signals from the

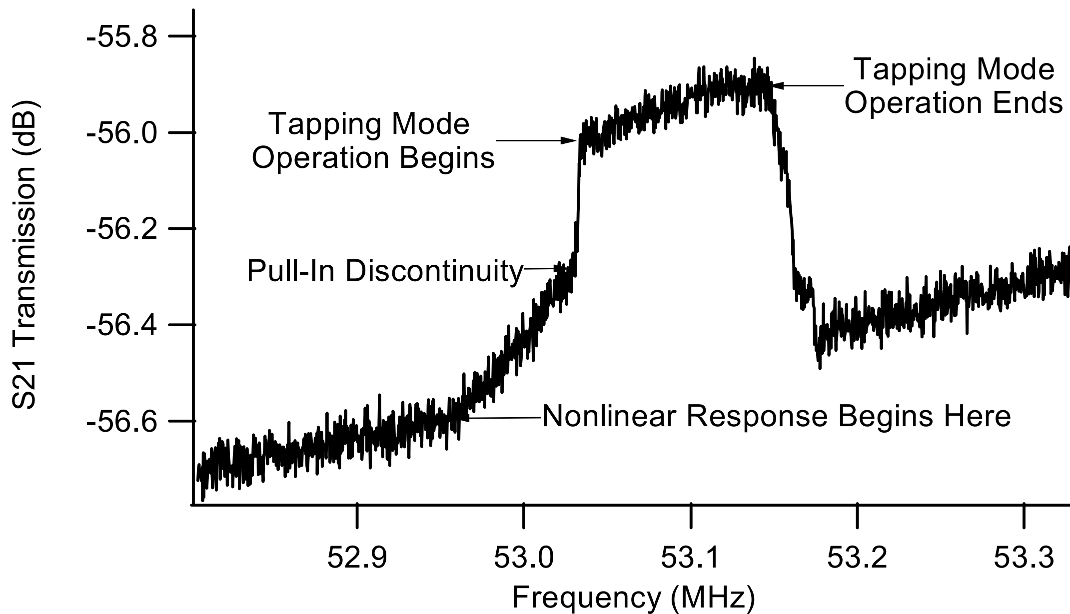

Figure 34. S_{21} Transmission magnitude measurement for the 11 μm long second mode device. $V_D = 3.1V$, $V_S = 2V$, $V_G = 0V$, and $P_{RF} = -10dBm$. The measured transmission response exhibits tapping mode characteristics.

nanowire resonators were more easily measured in the presence of large parasitic capacitances than the one-port or two-port capacitive techniques.

A 16 μm long, 350 nm wide second mode resonator was also tested. The (110) aligned device was adjacent to the 11 μm long device described above, (Fig 35). The distance between the gate electrodes was 3 μm for the 16 μm nanowire resonator, so the (100) fundamental mode was not actuated like the previous shorter device, however, the device was still nonlinear. A 1dB peak was measured at a resonant frequency of 29.9 MHz (Fig. 36), ANSYS predicts the second mode at 28 MHz. Attempts to extract the linear response of the device also failed.

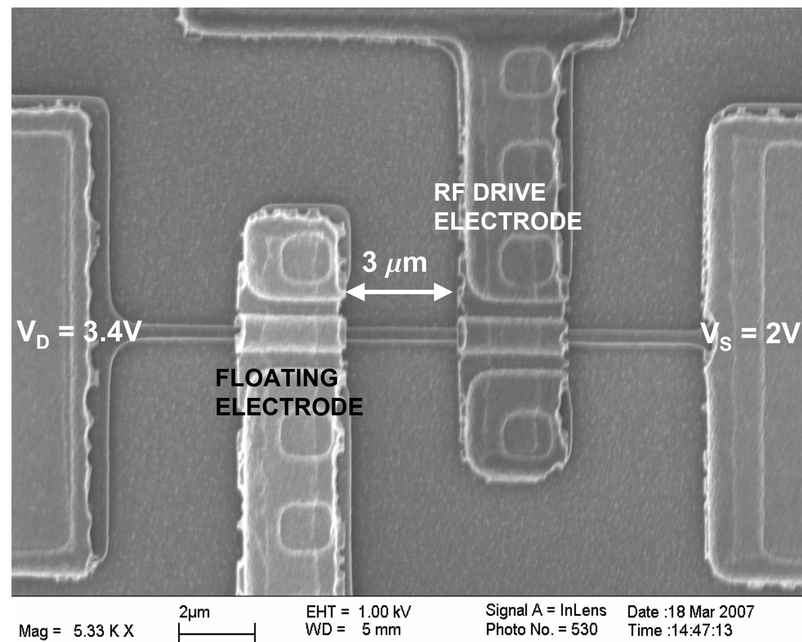

Figure 35. A (110) aligned 16 μm long and 350 nm wide 2nd mode resonator. P_{RF} = -10dBm, V_D = 3.4V, V_S = 2V and V_G = 0V.

Some (100) oriented 2nd mode nanowires were also tested (Fig. 37). The anticipated resonant frequency for the 16 μm device was 24.8 MHz and 48.1 MHz for the

11 μm long device. Figure 37A demonstrates the ability to tune the resonant frequency and Fig. 37B shows just how sensitive the magnitude response is to the RF signal power. Both (100) 2nd mode devices were still highly nonlinear.

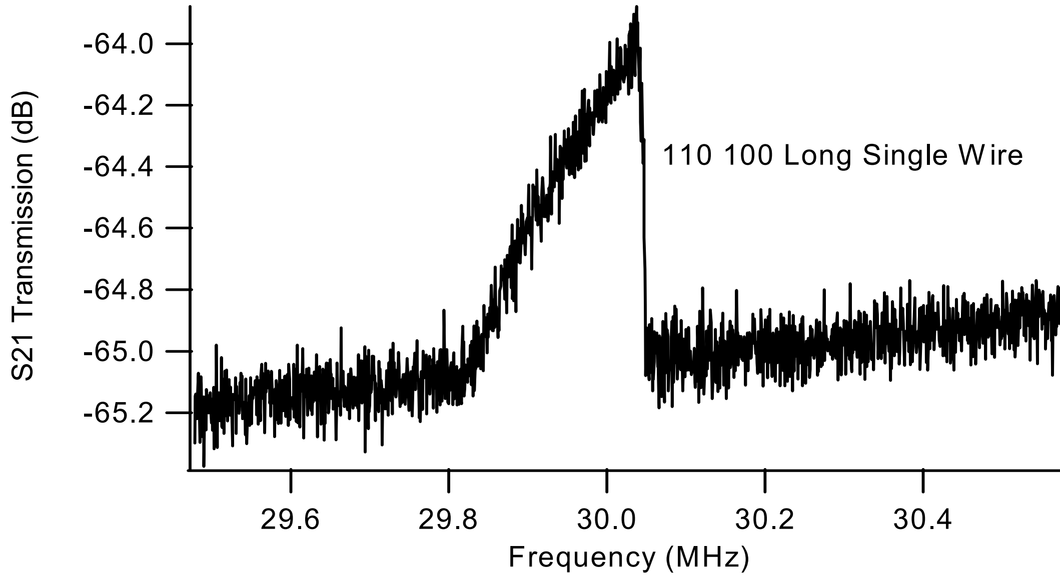

Figure 36. S_{21} transmission magnitude for the device shown in Fig. 32.

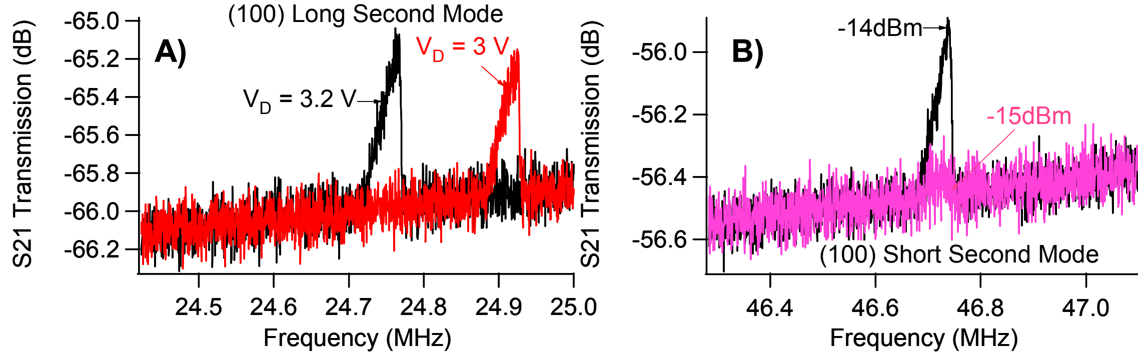

Figure 37. S_{21} transmission data for (100) second mode devices. A) 16 μm long, 330 nm wide nanowire response with V_D = 3.2V (black) or 3V (red) , V_S = 2V, V_G = 0V, and P_{RF} = -13dBm. B) 11 μm long, 380 nm wide nanowire response with V_D = 3.2V, V_S = 2V, V_G = 0V, and P_{RF} = -14dBm (black) and -15dBm (pink).

4.6 Chapter Summary

A new field-effect measurement technique for silicon nanowire resonators has been demonstrated on both single nanowire resonators and mechanically coupled nanowire resonant systems. The measurement technique exploits the semiconducting nature of single crystal silicon by employing electric fields to deplete three surfaces of the silicon nanowires. Harmonic motion is induced electrostatically with localized tri-gate polysilicon electrodes. As the nanowires deflect, the depletion regions on the lateral surfaces of the wire grow and recede, altering the resistance of nanowire segments located beneath the gate electrodes. The DC current passing through the wires at resonance is subsequently modulated and the AC current component can be easily detected with a network analyzer even in the presence of large parasitic capacitances.

A first-order model was developed to explain the electromechanical behavior of the device. Although the results of the model did not exactly match the measured response of the device, the model does lend credence to the proposed depletion-mode field-effect sense mechanism. Finally, nonlinear nanowire resonators were demonstrated using the field-effect characterization technique at relatively low bias voltages, which may open possibilities for integration with CMOS electronics for signal processing and computation applications.

4.7 References

[1] C. Durand, et al., "Characterization of IN-IC Integrable In-Plane Nanometer Scale Resonators Fabricated by a Silicon on Nothing Advanced CMOS Technology," *Proceedings of the 21st IEEE International Conference on Micro Electro Mechanical Systems (MEMS 2008)*, Tucson, AZ Jan. 13-18 2008 pp.1016-1019.

[2] K. L. Ekinci and M. L. Roukes, "Nanoelectromechanical Systems," *Review of Scientific Instruments*, Vol. 76, 2005, article #061101.

[3] A. N. Cleland and M. L. Roukes, "Fabrication of high frequency nanometer scale mechanical resonators from bulk Si crystals," *Applied Physics Letters*, Vol. 69, No. 18, Oct. 28 1996 pp.2653-2655.

[4] A. N. Cleland, *Foundations of Nanomechanics*, Springer-Verlag, Berlin Germany 2003.

[5] X. L. Feng, et al., "Dissapation in Single-Crystal 3C-SiC Ultra-High Frequency Nanomechanical Resonators," *Technical Digest of the 2004 Solid-State Sensor and Actuator Workshop*, Hilton Head Isl, SC. June 4-8, 2006, pg. 86-89.

[6] A. Husain, et al., "Nanowire-based very-high-frequency electromechanical resonator," *Applied Physics Letters*, Vol. 83, No. 6, Aug. 2003, pp.1240-1242.

[7] Y. T. Yang, et al., "Zeptogram-Scale Nanomechanical Mass Sensing," *Nano Letters*, Vol. 6, No. 4, Apr. 2006, pp.583-586.

[8] V. Sazonova, et al., "A tunable carbon nanotube electromechanical oscillator" *Nature*, Vol. 431, Sept. 2004, pp.284-287.

[9] V. A. Sazonova, *A Tunable Carbon Nanotube Resonator*, Cornell University Ph.D. Dissertation, Aug. 2006.

[10] H. B. Peng, et al., "Ultrahigh Frequency Nanotube Resonators," *Physical Review Letters*, Vol. 97, Aug. 2006, article# 087203.

[11] H. B. Peng, et al., "Microwave electromechanical resonator consisting of clamped carbon nanotubes in an abacus arrangement," *Physical Review B*, Vol. 76, July 2007, article #035405.

[12] S. Heinze, et al., "Carbon Nanotubes as Schottky Barrier Transistors," *Physical Review Letters*, Vol. 89, No. 10, Sept. 2002, article# 106801.

[13] H. C. Nathanson and R. A. Wickstrom, "A Resonant-Gate Silicon Surface Transistor With High-Q Band-Pass Properties," *Applied Physics Letters*, Vol. 7 No. 4, Aug. 15 1965 pp. 84-86.

[14] W. E. Newell, "Tuned Integrated Circuits – A State-of-the-Art Survey," *Proceedings of the IEEE*, Vol. 52, 1964, pp.1603-1608.

[15] N. Abele, et al., "Comparison of RSG-MOSFET and capacitive MEMS resonator detection," *Electronics Letters*, Vol. 41, No. 5, Mar. 2005, pp.242-244.

[16] H. C. Nathanson, W. E. Newell, R. A. Wickstrom, and J. R. Davis, "The Resonant Gate Transistor," *IEEE Transactions on Electron Devices*, Vol. ED-14, No. 3, Mar. 1967, pp.117-133.

[17] N. Abele, et al., "Ultra-Low Voltage MEMS Resonator Based on RSG-MOSFET," *Proceedings of the 19th IEEE International Conference on Micro Electro Mechanical Systems (MEMS 2006)*, Istanbul, Turkey Jan. 22-26, 2006, pp.882-885.

[18] D. Grogg, D. Tsamados, N. D. Badila and A. M. Ionescu, "Integration of Mosfet Transistors in MEMS Resonators for Improved Output Detection," *Proceedings of the 14th International Conference on Solid-State Sensors, Actuators and Micro-systems (Transducers 2007)*, Lyon, France June 10-14, 2007, pp.1709-1712.

[19] S. A. Bhave, *Electrostatic Transduction for MEMS Resonators*, University of California, Berkeley Ph.D. Dissertation Fall 2004.

[20] L. Chang, *Nanoscale Thin-Body CMOS Devices*, University of California, Berkeley Ph.D. Dissertation Spring 2003.

[21] S. –B. Shim, M. Imboden and P. Mohanty, "Synchronized Oscillation in Coupled Nanomechanical Oscillators," *Science*, Vol. 316 April 6, 2007, pp.95-99.

[22] M. Bescond, et al., "3D Quantum Modeling and Simulation of Multiple-Gate Nanowires MOSFETS," *Technical Digest of the IEEE International Electron Device Meeting*, Dec. 13-15, 2004, pp.617-620.

[23] B.S. Doyle, et al., "High Performance Fully-Depleted Tri-Gate CMOS Transistors," *IEEE Electron Device Letters*, Vol. 24, No. 4, Apr. 2003, pp.263-265.

[24] Q. Zou, U. Sridhar, Z. Wang, "Silicon as an Electronic Material in Electrostatic MEMS," *Proceedings of the 8th International Conference on Solid-State Sensors, Actuators and Microsystems (Transducers 1999)*, Sendai, Japan June 1999.

[25] V. Kaajakari: http://www.kaajakari.net/%7Eville/research/tutorials/elasticity_tutorial.pdf

[26] E. Quevy, B. Legrand, D. Collard, and L. Buchaillot, "Tapping-Mode HF Nanometric Lateral Gap Resonators: Experimental and Theory," *Proceedings of the 12th International Conference on Solid-State Sensors, Actuators and Micro-systems (Transducers 2003)*, Boston, MA June 8-12, 2003, pp.879-882.

[27] J. Saijets and M. Aberg, "MOSFET RF Extraction Uncertainties Due to S Parameter Measurement Errors," *Physica Scripta*, Vol. T114, 2004, pp.244-247.

Chapter 5. Conclusions and Future Work

The previous chapters have described the design, fabrication, and characterization of silicon nanowire based resonant systems. Silicon nanowires were used as mechanical coupling beams which perturbed the frequency response of a coupled pair of flexural-mode MEMS resonators. Single nanowire and mechanically coupled nanowire resonators were characterized using a new field-effect detection scheme, which may facilitate integration with CMOS electronics.

5.1 Nanowire Coupled MEMS Resonators Conclusions

Precise control over the nanowire coupler dimensions and location is required for future ultra-narrow bandwidth MEMS filters. Therefore, the combination of i-line photolithography, photoresist ashing, and focused ion beam etching used to fabricate the coupled devices described in Chapter 2 is not well suited for MEMS filters. In addition to nanoscale coupling beams, narrow band MEMS filters should be fabricated with high-Q MEMS resonators to minimize insertion loss [1]. The nitride pillars anchoring the MEMS resonators are etched when the coupled systems are released in vapor HF, resulting in low-Q resonators due to increased anchor losses and unmatched MEMS resonators due to variations in anchor stiffness. The coupled resonant devices do not have a ground plane and capacitive signals are only measured with one of the MEMS resonators limiting the signal-to-feedthrough ratio of the measured magnitude response.

In spite of the above limitations, a low-velocity coupled MEMS filter was demonstrated with a bandwidth of 60 kHz at 18 MHz. The bandwidth, or frequency spans, of the maximum velocity coupled devices could not be tuned below 780 kHz because the nanowire couplers buckled after they were trimmed with a focused ion beam

to widths below 200 nm. Although the nanowire coupled MEMS resonators were not suitable for use as electromechanical signal processing devices, the silicon nanowires described in this thesis behaved as excellent flexural-mode coupling beams for clamped-clamped MEMS resonators. The coupled devices could ultimately find use as nanometrology instruments since their frequency span, or bandwidth, was sensitive to the stiffness of the nanowire coupler.

5.2 Silicon Nanowire Resonators Conclusions

A new field-effect transduction scheme was demonstrated on silicon nanowire resonators at room temperature in a vacuum of 1 mTorr. In contrast to the magnetomotive transduction technique [2], the signals measured using the field-effect detection technique were an order of magnitude larger than the magnetomotive techniques (10s of microvolts compared to single microvolts). However, the signal to background, or feedthrough, levels for field-effect sensed nanowire resonators are about 0.2 dB compared to 8 dB for inductively sensed nanowire resonators [2]. Consequently, the quality factors of the field-effect sensed silicon nanowire resonators were estimated using a lorentzian curve fit. While the field-effect detection method was less electronically complex than the signal mixing technique demonstrated on resonating carbon nanotubes (CNTs) [3,4], the carbon nanotube resonators were operated at room temperature and at ambient pressure. Futhermore, a DC bias current was not required for the signal mixing technique. However, unlike the mixing scheme, the demonstrated field-effect detection scheme produced detectable RF signals in the presence of large parasitic capacitances. Finally, the surface quality of the silicon nanowires appears to

degrade over time corresponding to a drop in transmission magnitude for field-effect sensed silicon nanowires.

5.3 Suggestions for Future Work

5.3.1 Top Down Fabrication Process

Pillar-type anchors are required to suspend polysilicon tri-gate electrodes above MEMS and NEMS resonators with gaps on the order of tens of nanometers. Undoped poly diamond or SiC pillars should be used in future fabrication processes to avoid anchor damage during the vapor HF release step. Acoustically mismatched anchor materials could also minimize anchor losses resulting in higher quality factor resonators [5].

Modern 193 nm photolithography should be used to pattern the silicon nanowires with proximity correction to provide tighter control over the length and width of the nanostructures. Nanowires with widths on the order of tens of nanometers could be patterned with 193 nm lithography techniques used in the microelectronics industry.

A thin dry oxide passivation layer should be grown on the silicon nanowire resonators to control the surface charge density of the nanowires [6]. A high dielectric constant material, which is resistant to HF, should be deposited on top of the passivation layer to ensure that the field-effect transduction efficiency does not decrease over time. The lateral sacrificial oxide should be thinner to ensure greater gate control over the lateral nanowire surfaces. Alternatively, an encapsulation process could be developed or adapted to encase the devices in a suitable vacuum environment.

Finally, SOI wafers with highly doped handle wafers should be used as the starting material to provide a ground plane for the resonant devices. Highly doped silicon

structures, which are electrically coupled to the ground plane, should be fabricated in close proximity to the resonant devices to further reduce the magnitude of the feedthrough capacitance.

5.3.2 Nanowire Coupled MEMS Resonators

Extensional-mode nanowires should be coupled to high-Q bulk mode resonators in order to create ultra-narrow bandwidth MEMS filters. Lateral VLS nanowires are ideal for this application because their stiffness could be much lower than couplers with the same height as the MEMS resonators [7,8]. Furthermore, once the metallized tip of lateral VLS nanowires makes contact to opposing lateral silicon surfaces, a mechanically rigid epitaxial link to the opposing surface is created [9,10]. An oxide window process could be adapted to grow silicon nanowires on the lateral surfaces of single or poly crystalline resonators [11] (reviewed in Appendix C), however device yields would be low because VLS nanowire synthesis is still a random process.

Extensional-mode nanowire couplers could be used to study the giant piezoresistance effect [12,13,14] of silicon nanowires as a function of frequency, similar to [15]. The envisioned piezoresistance probe system would require multiple bulk-mode resonators with either conductive or non-conductive VLS nanowire couplers to electrically isolate bulk-mode mechanical drive resonators from the source and drain resonators (see Fig. 1).

RF strained FET operation could potentially be demonstrated provided that double- or tri-gate electrodes are in close proximity to the extensional mode nanowire (gap < 20 nm) to achieve reasonable threshold voltages (Fig. 1). A passivation layer must be grown on the nanowire to control its surface charge density and to ensure that the

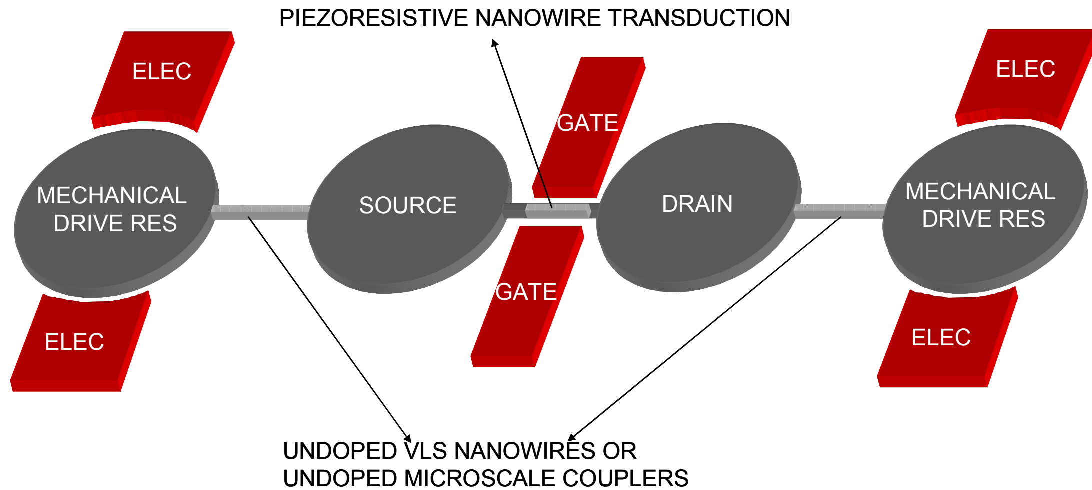

Figure 1. Bulk-mode resonator architecture proposed to probe the piezoresistive properties of nanowires at RF frequencies. The left and right most resonators are actuated electrostatically and electrically isolated from the source and drain resonators. The RF signal would be sensed out of the source or drain resonators. The mechanical drive resonators would induce a longitudinal mechanical strain on the nanowire between the source and drain.

threshold voltage does not drift significantly [16].

5.3.3 Silicon Nanowire Resonators

The DC current path should be shortened to decrease the drain voltage required to extract a detectable signal from the mechanically coupled nanowire resonators. This can be accomplished by redesigning the layout such that the drain and source electrodes make contact to the opposing ends of the same nanowire (Fig. 2). The layout redesign would also free up the second parallel nanowire which could be used exclusively to drive the sense nanowire mechanically (see Fig. 2). The nanowire mechanical coupler should be highly resistive to minimize the current flowing between the drive and sense nanowires

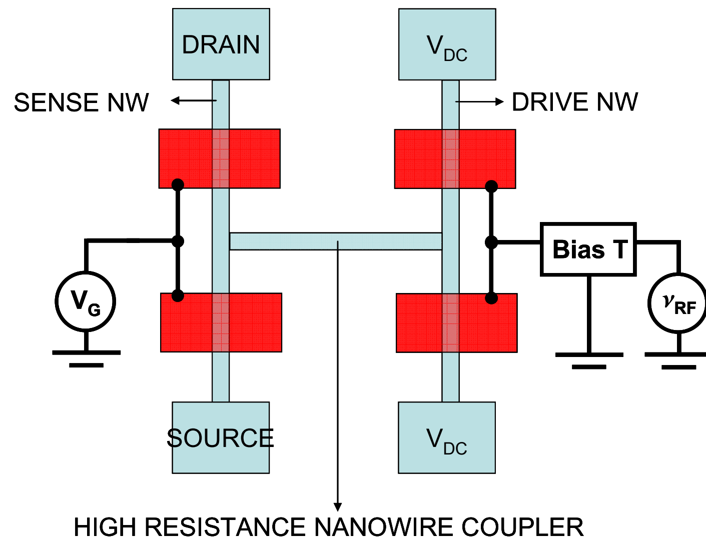

Figure 2. The proposed layout redesign would create a drive and sense nanowire configuration. A high resistance nanowire coupler would be required for this redesign.

through the nanowire coupler.

Multiple port operation could be demonstrated by mechanically coupling many nanowire resonators. In addition, multiple in-phase vibrating nanowires could be connected in parallel such that all the RF current signals add [1]. Assuming a 10 μm long, 280 nm wide nanowire has a resistivity of $6\text{X}10^{-3}$ Ω−cm, the resistance of the nanowire would be 7.8 kΩ; therefore, approximately 150 parallel nanowire resonators would be required to match to the 50 Ω impedance of a network analyzer.

Other mechanical coupling strategies should be investigated such as torsional-mode couplers [8]. Capacitive coupling strategies should also be pursued similar to the work presented in [17].

Finally, the frequency, gate length, electrostatic gap, and nanowire diameter limits would have to be investigated for the field-effect sensing technique described in Chapter 4. The method could also be adapted to single or multiple VLS nanowires provided that a suitable merged VLS-microfabrication process is designed.

5.4 References

[1] S.-S. Li, Y.-W. Lin, Z. Ren, and C. T.-C. Nguyen, "An MSI Micromechanical Differential Disk-Array Filter", *Proceedings of the 14th International Conference on Solid-State Sensors, Actuators and Microsystems* (*Transducers 2007*), Lyon, France, June 10-14, 2007 pp.307-311.

[2] X. L. Feng, R. He, P. Yang, M. L. Roukes, "Very High Frequency Silicon Nanowire Electromechanical Resonators," *Nano Letters*, Vol. 7, No. 7, 2007, pp.1953-1959.

[3] V. Sazonova, et al., "A tunable carbon nanotube electromechanical oscillator" *Nature*, Vol. 431, Sept. 2004, pp.284-287.

[4] H. B. Peng, et al., "Ultrahigh Frequency Nanotube Resonators," *Physical Review Letters*, Vol. 97, Aug. 2006, Article# 087203.

[5] J. Wang, J. E. Butler, T. Feygelson, and C. T.-C. Nguyen, "1.51-GHz Nanocrystalline Diamond Micromechanical Disk Resonator With Material-Mismatched Isolating Support," *Technical Digest of the 17th IEEE International MEMS Conference (MEMS 2004)*, Masstricht, The Netherlands, Jan 25-29, 2004, pp.641-644.

[6] K.-i. Seo, et al., "Surface Charge Density of Unpassivated and Passivated Metal-Catalyzed Silicon Nanowires," *Electrochemical and Solid-State Letters*, Vol. 9, No. 3, 2006, pp.G69-G72.

[7] S.-S. Li, Y.-W. Lin, Y. Xie, Z. Ren, and C. T.-C. Nguyen, "Small Percent Bandwidth Design of a 423-MHz Notch-Coupled Micromechanical Mixler," *Proceedings of the 2005 IEEE International Ultrasonics Symposium*, Rotterdam, The Netherlands, Sept. 18-23, 2005, pp.1295-1298.

[8] R. A. Johnson, *Mechanical Filters in Electronics*, Wiley, New York, NY 1983.

[9] A. San Paulo, et al., "Mechanical eleasticity of single and double clamped silicon nanobeams fabricated by the vapor-liquid-solid method," *Applied Physics Letters*, Vol. 87, 2005, article #053111.

[10] M. Tabib-Azar, et al., "Mechanical properties of self-welded silicon nanobridges," *Applied Physics Letters*, Vol. 87, 2005, article #113102.

[11] A. San Paulo, et. al., "Suspended Mechanical Structures Based on Elastic Silicon Nanowire Arrays," *Nano Letters*, Vol. 7, No. 4, pp.1100-1104.

[12] T. Toriyama, Y. Tanimoto, and S. Sugiyama, "Single Crystal Silicon Nano-Wire Piezoresistors for Mechanical Sensors," *Journal of Microelectromechanical Systems*, Vol. 11, No. 5, Oct. 2002, pp.605-611.

[13] R. He and P. Yang, "Giant Piezoresistance effect in silicon nanowires," *Nature Nanotechnology*, Vol. 1. Oct. 2006, pp.42-46.

[14] K. Reck, J. Richter, O. Hansen, and E. V. Thomsen, “Piezoresistive Effect in Top-Down Fabricated Silicon Nanowires,” *Technical Digest of the 21st IEEE International Conference on Micro Electro Mechanical Systems (MEMS 08)*, Tucson, AZ. Jan 13-17, 2008, pp.717-720.

[15] J. T. M. van Beek, et al., “Scalable 1.1 GHz fundamental mode piezo-resistive silicon MEMS resonator,” *Technical Digest of the IEEE International Electron Device Meeting*, Dec. 13-15, 2007, pp.411-414.

[16] D. Grogg, D. Tsamados, N. D. Badila and A. M. Ionescu, “Integration of Mosfet Transistors in MEMS Resonators for Improved Output Detection,” *Proceedings of the 14th International Conference on Solid-State Sensors, Actuators and Micro-systems (Transducers 2007)*, Lyon, France June 10-14, 2007, pp.1709-1712.

[17] L. Pescini, H. Lorenz, and R. H. Blick, “Mechanical gating of coupled nanoelectromechanical resonators operating at radio frequency,” *Applied Physics Letters*, Vol. 82, No. 3, pp.352-354.

Appendix A. Maximum Velocity Coupled Device Model

The general procedure for modeling maximum velocity devices outlined in section 2.6 was followed to estimate the frequency span of MVA with a 232 nm wide coupler (Ch. 2, Fig. 15) and the nanowire tethered island coupler from Chapter 2 (Fig. 17).

MVA results (with 232 nm coupler)

Bias Voltage (V)	Mode 1 (MHz)	Mode 2 (MHz)	Center Freq. (MHz)	Freq. Span (MHz)
8.5	17.67	18.52	18.10	0.85
9	17.65	18.50	18.08	0.85
9.5	17.62	18.46	18.04	0.84
10	17.58	18.43	18.01	0.85
10.5	17.56	18.40	17.98	0.84
11	17.55	18.40	17.97	0.85
11.1	17.55	18.39	17.97	0.84
11.5	17.53	18.38	17.96	0.85
12	17.51	18.35	17.93	0.84

Table A1. Data from MVA with FIB trimmed 232 nm wide coupler.

Bias Voltage (V)	Mode 1 (MHz)	Mode 2 (MHz)	Center Freq. (MHz)	Freq. Span (MHz)
8.5	17.72	18.49	18.11	0.78
9	17.69	18.47	18.08	0.78
9.5	17.66	18.44	18.05	0.78
10	17.64	18.42	18.03	0.78
10.5	17.62	18.40	18.01	0.78
11	17.60	18.38	17.99	0.78
11.1	17.60	18.38	17.99	0.78
11.5	17.58	18.36	17.97	0.78
12	17.57	18.35	17.96	0.78

Table A2. Model results for MVA with FIB trimmed 232 nm wide coupler.

(A.1) $f_0(V_P) = a + bV_P$, a = 18.50 MHz = f_0, and b = -0.05 MHz/V with R^2 = 0.972

(A.2) $V_{EFF}(V_P) = a + bV_P + cV_P^2$, a = -0.26V, b = 0.81, c = -0.03/V with R^2 = 0.964

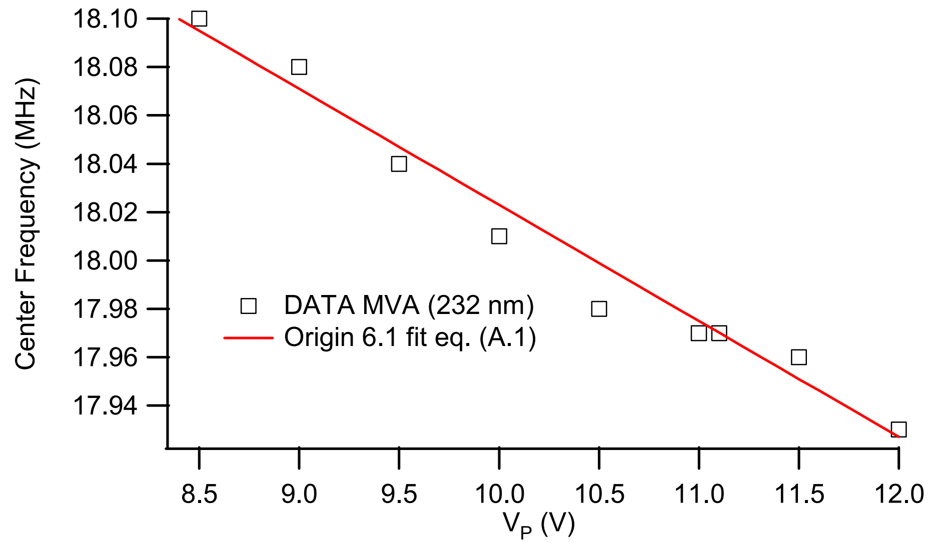

Figure A1. Center frequencies for the FIB trimmed MVA (232 nm wide coupler) versus V_P. The red fitting curve was generated in Origin using a linear fit due to the inflection point recorded at 11V. The unbiased resonant frequency, f_0, used for the model was 18.50 MHz

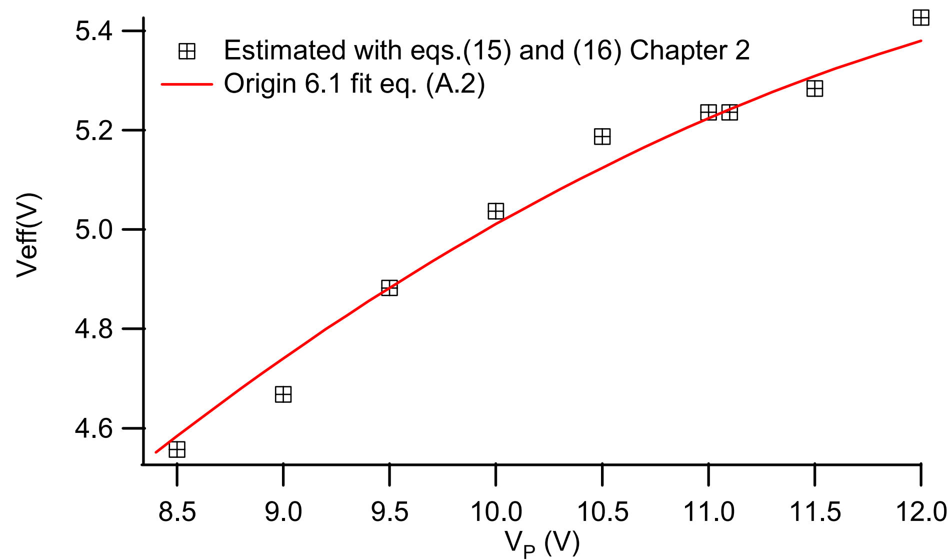

Figure A2. V_{EFF} calculated using Eqs. (15) and (16) given as discrete points for MVA after the coupler was trimmed with the FIB (232 nm wide) and the Origin derived function from Eq. (A.2) (red trace).

MVA (232 nm) was also modeled using the V_{EFF} Origin fit, Eq. (17) for MVA before the coupler was trimmed and f_0 = 18.23 MHz. The results are given in Table A3. The results closely match the model results from Table 2A.

Bias Voltage (V)	Mode 1 (MHz)	Mode 2 (MHz)	Center Freq. (MHz)	Freq. Span (MHz)
8.5	17.72	18.50	18.11	0.78
9	17.70	18.48	18.09	0.78
9.5	17.68	18.46	18.07	0.78
10	17.66	18.44	18.05	0.78
10.5	17.63	18.41	18.02	0.78
11	17.61	18.39	18.00	0.78
11.1	17.60	18.38	17.99	0.78
11.5	17.58	18.36	17.97	0.78
12	17.56	18.34	17.95	0.78

Table A3. Model results for MVA (232 nm wide coupler) using f_0 = 18.23 MHz and V_{EFF} from Eq. (17) with a = -0.77 V, b = 0.39, and c = -6E-4 /V just like MVA with the 380 nm wide coupler.

Model Results for the Device Shown in Chapter 2 Fig. 17

The width of the coupler was calculated using a weighted average:

$$\text{(A.3)} \quad W_{AVE_FIG17} = \frac{160(L_{LT}) + 460(L_{IS}) + 180(L_{RT})}{L_{LT} + L_{IS} + L_{RT}} \quad [nm]$$

where L_{LT}, L_{IS}, and L_{RT} are the lengths of the left tether (2.8 μm), island (1 μm), and right tether (2.6 μm) respectively.

Bias Voltage (V)	Mode 1 (MHz)	Mode 2 (MHz)	Center Freq. (MHz)	Freq. Span (MHz)
6	15.86	17.34	16.60	1.48
6.5	15.82	17.31	16.57	1.49
7	15.78	17.27	16.53	1.49

Table A4. Data before the nanowire coupler was trimmed at P_{RF} = -14dBm.

Bias Voltage (V)	Mode 1 (MHz)	Mode 2 (MHz)	Center Freq. (MHz)	Freq. Span (MHz)
4.7	16.30	17.08	16.69	0.78
5	16.29	17.06	16.68	0.77
5.3	16.28	17.05	16.67	0.77
5.5	16.26	17.04	16.65	0.78
5.8	16.23	17.00	16.62	0.77
6	16.22	16.99	16.61	0.77
6.3	16.20	16.98	16.59	0.78

Table A5. Measured response after the nanowire coupler was trimmed at P_{RF} = -17dBm.

Bias Voltage (V)	Mode 1 (MHz)	Mode 2 (MHz)	Center Freq. (MHz)	Freq. Span (MHz)
4.7	16.25	16.96	16.60	0.70
5	16.24	16.94	16.59	0.70
5.3	16.22	16.92	16.57	0.70
5.5	16.21	16.91	16.56	0.70
5.8	16.19	16.89	16.54	0.70
6	16.17	16.87	16.52	0.70
6.3	16.14	16.85	16.49	0.70

Table A6. Modeling results after the nanowire coupler was trimmed at P_{RF} = -17dBm. F_0 was estimated to be 16.72 MHz from the maximum value of Eq. (A.3).

(A.4) $f_0(V_P) = a + bV_P + cV_P^2$, a = 16.54 MHz, b = 0.11 MHz/V, c = -0.02 MHz/V^2 with R^2 = 0.964.

(A.5) $V_{EFF}(V_P) = a + bV_P$, a = -2.97V, b = 0.87 with R^2 = 0.982.

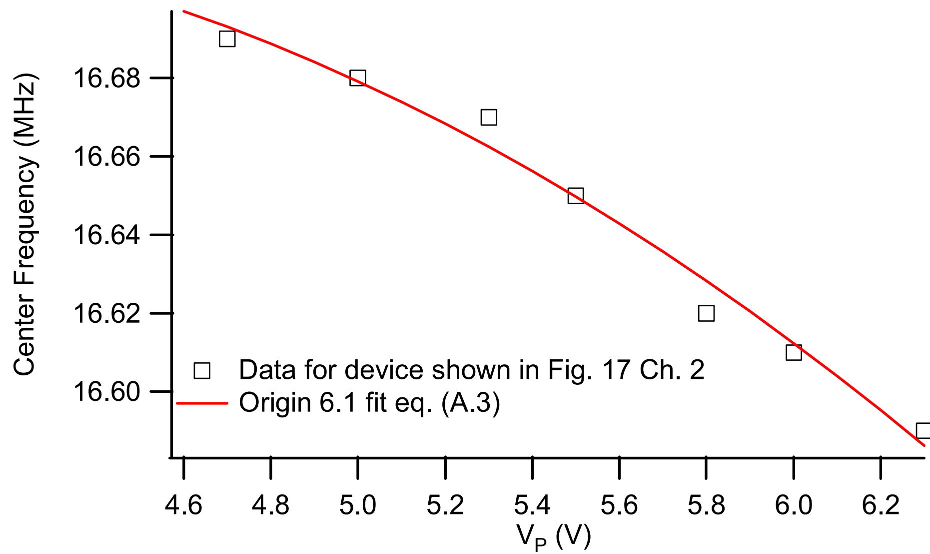

Figure A3. Center frequencies for the maximum velocity device from Fig. 17 Ch. 2 versus applied voltage (from Table A5). The red fitting curve was generated in Origin Eq. (A.4). The unbiased resonant frequency used for the model was 16.72 MHz.

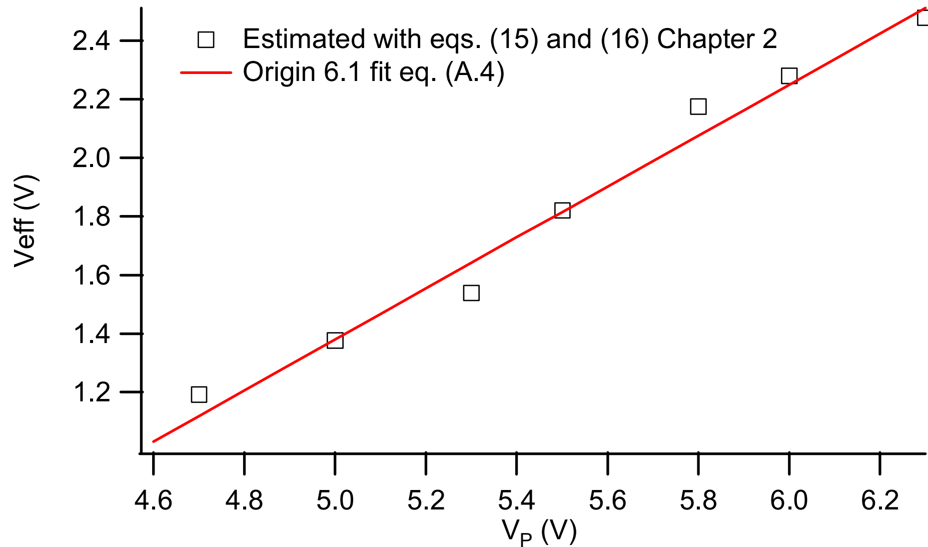

Figure A4. V_{EFF} calculated using Eqs. (15) and (16) and the Origin derived function from Eq. (A.5) (red trace).

Appendix B. Transconductance Calculation

Measured S parameters are typically required to calculate the transconductance of RF field-effect transistors. Using the linear magnitude, referred to as M for this discussion, and the phase θ of the S parameters the real and imaginary components can be calculated:

(B.1) $$S_{xy} = M_{xy}cos(\theta_{xy}) + jM_{xy}sin(\theta_{xy})$$

where j = $\sqrt{-1}$, the cosine term and the sine term are the real and imaginary components of S_{xy} respectively. The real and imaginary components of the S parameters are then used to calculate the transconductance g_m using [1]:

(B.2) $g_m = Real(y_{21})$, where

(B.3) $$y_{21} = \frac{-2S_{21}}{Z_0((1+S_{11})(1+S_{22})-(S_{12}S_{21}))}$$

Z_0 = 50 Ω is typically used for transistor calculations [1].

Although the nanowire resonators described in Chapter 4 are not vibrating transistors, Eqs. (B.1)-(B.3) were used to calculate the transconductance of vibrating nanowire resistors. S_{11}, S_{12}, and S_{22} were not measured for device OP-A. However, a new device, with the same orientation (Fig. 1B), was released and all four S parameter were measured (Figs. 2B-9B). The S parameters were measured at V_D = 6V, V_S = 2V, V_G = 0V, and P_{RF} = -14dBm, represented by the black traces in Figs. 2B-9B. To measure the feedthrough levels, represented by the purple traces in Figs. 2B-9B, the drain voltage was decreased to V_D = 5.2V while maintaining the other voltages and RF signal power constant. A S_{11} signal peak was not visible in Figs. 2B-3B, so S_{11} was eliminated from Eq. (B.3):

(B.4) $$y_{21} = \frac{-2S_{21}}{Z_0((1+S_{22})-(S_{12}S_{21}))}.$$

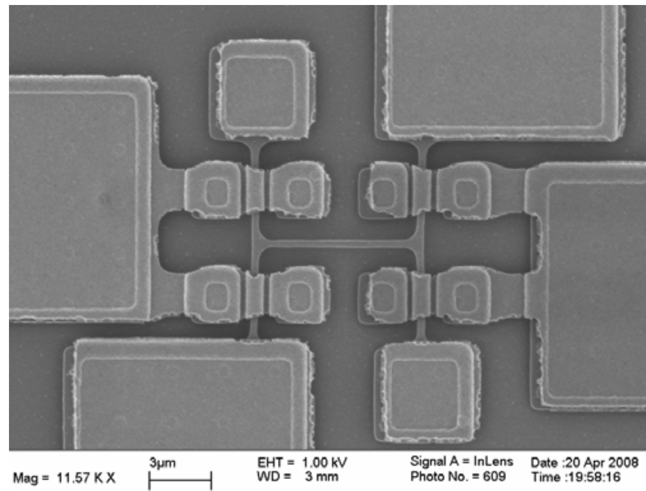

Figure 1B. Out-of-phase device, with 290 nm wide nanowires, used to measure S_{11}, S_{22}, S_{12}, and S_{21}.

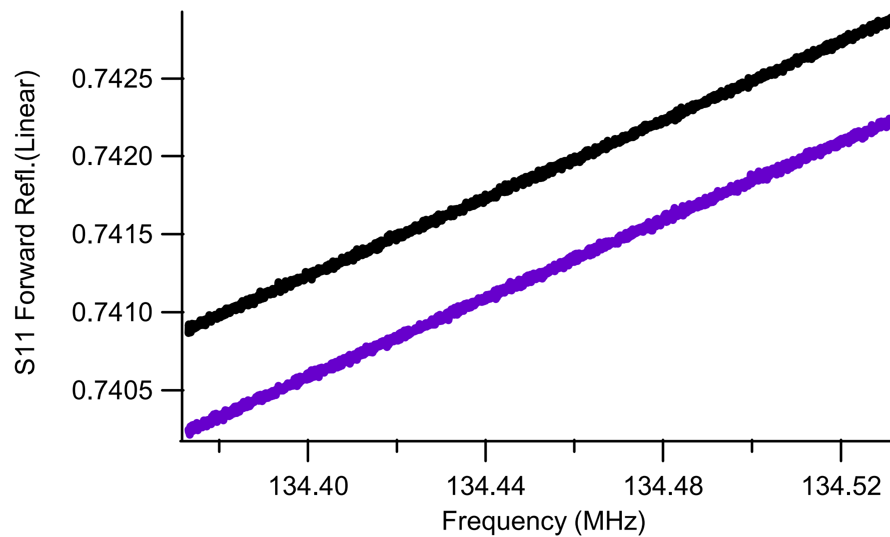

Figure 2B. S_{11} linear magnitude. The black trace is the measured signal and the purple trace is the feedthrough.

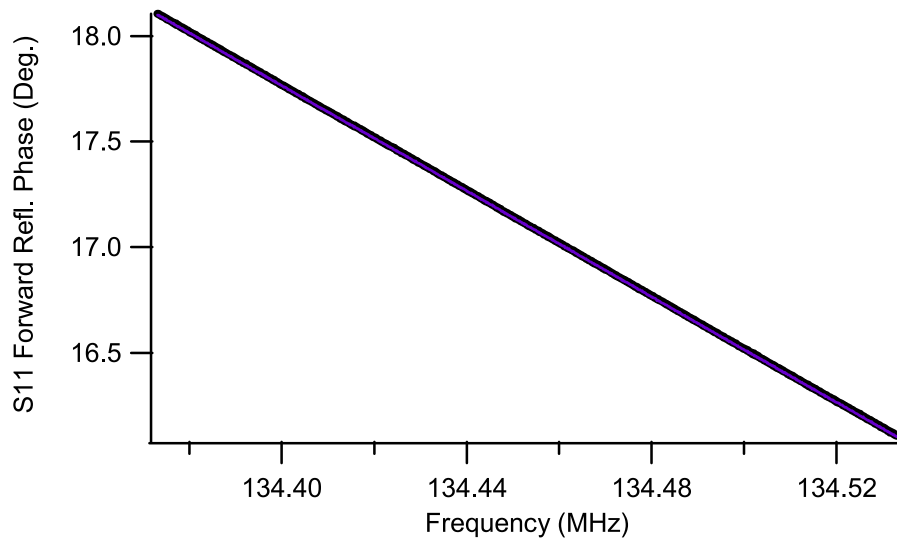

Figure 3B. S_{11} phase. The purple feedthrough phase lies on top of the black signal phase.

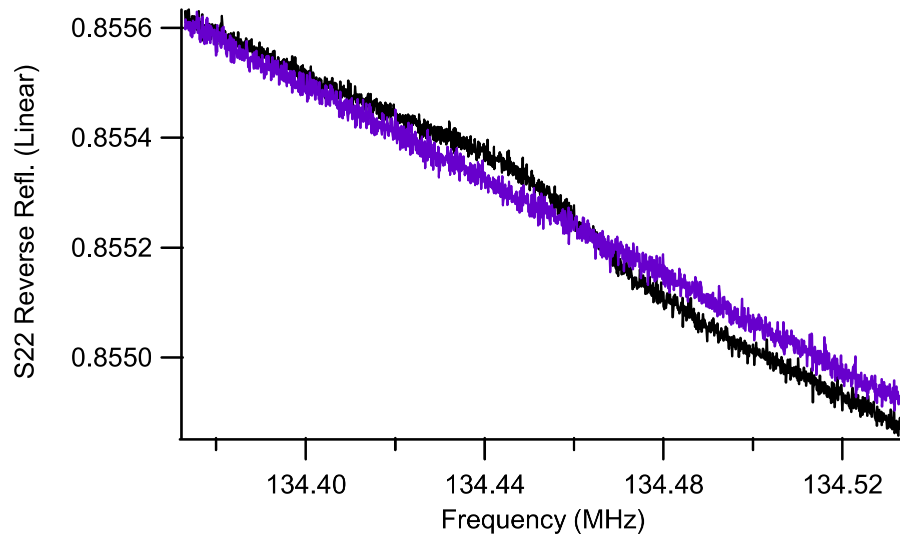

Figure 4B. S_{22} linear magnitude. The black trace is the measured signal and the purple trace is the feedthrough.

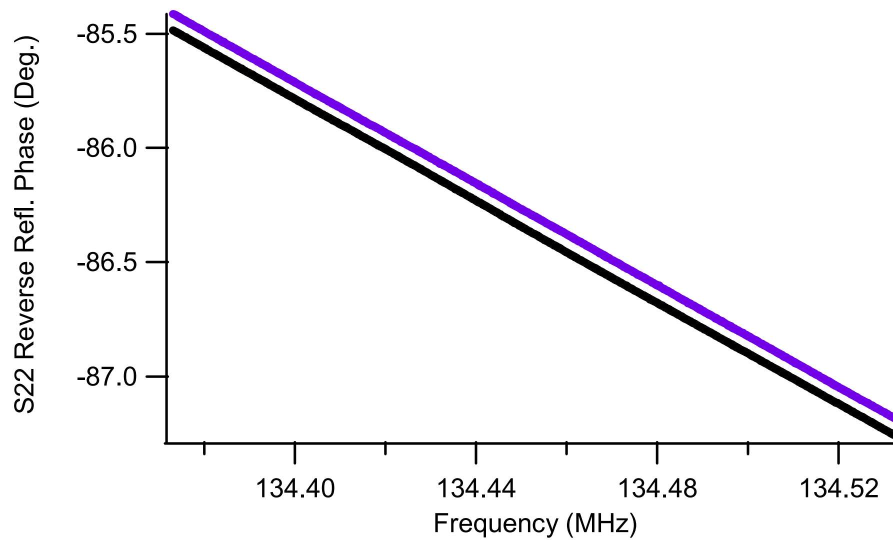

Figure 5B. S_{22} phase. The black trace is the measured signal and the purple trace is the feedthrough.

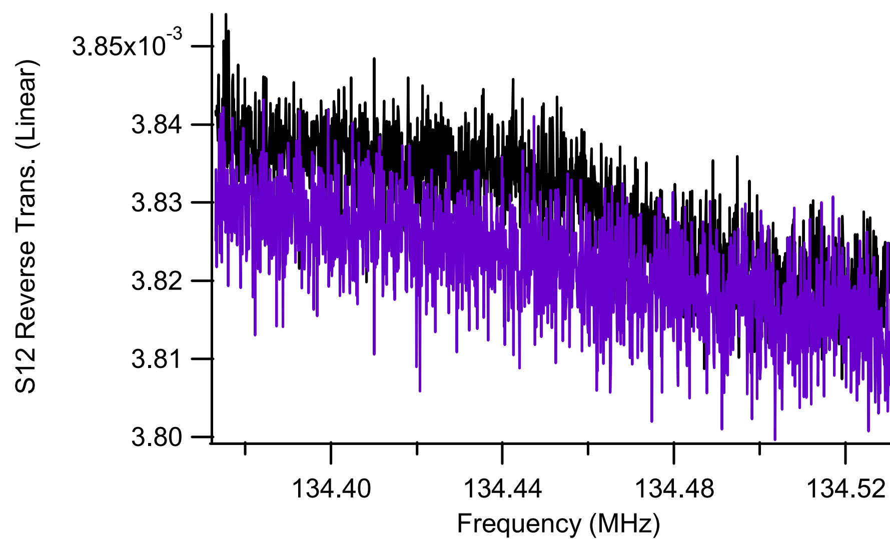

Figure 6B. S_{12} linear magnitude. The black trace is the measured signal and the purple trace is the feedthrough.

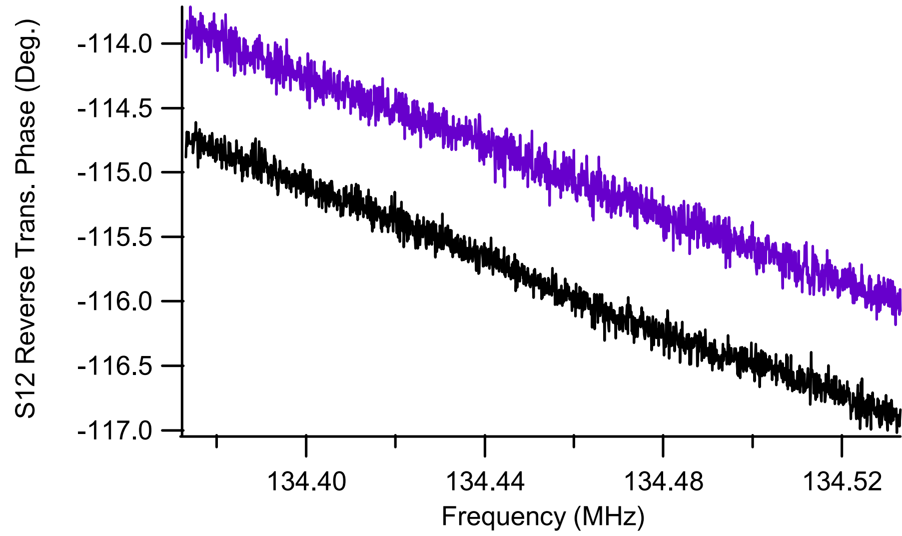

Figure 7B. S12 phase. The black trace is the measured signal and the purple trace is the feedthrough.

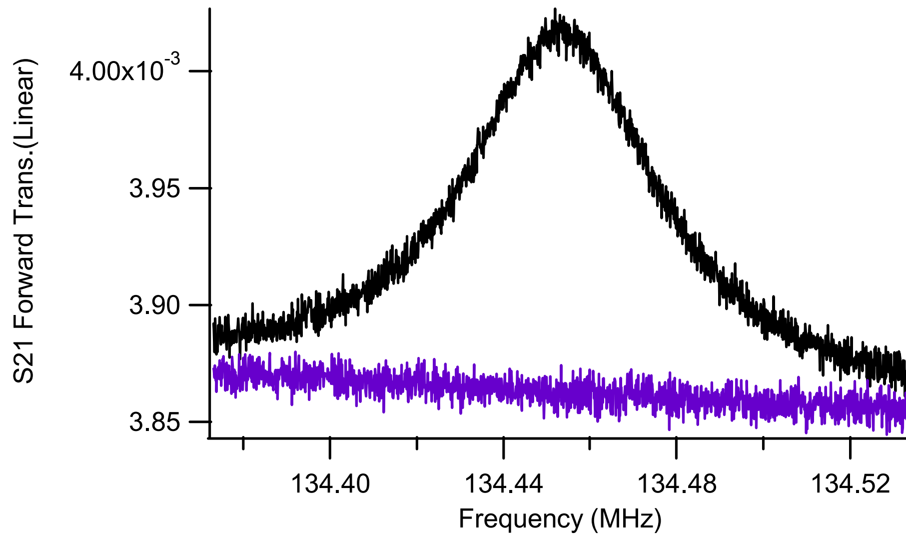

Figure 8B. S_{21} linear magnitude. The black trace is the measured signal and the purple trace is the feedthrough.

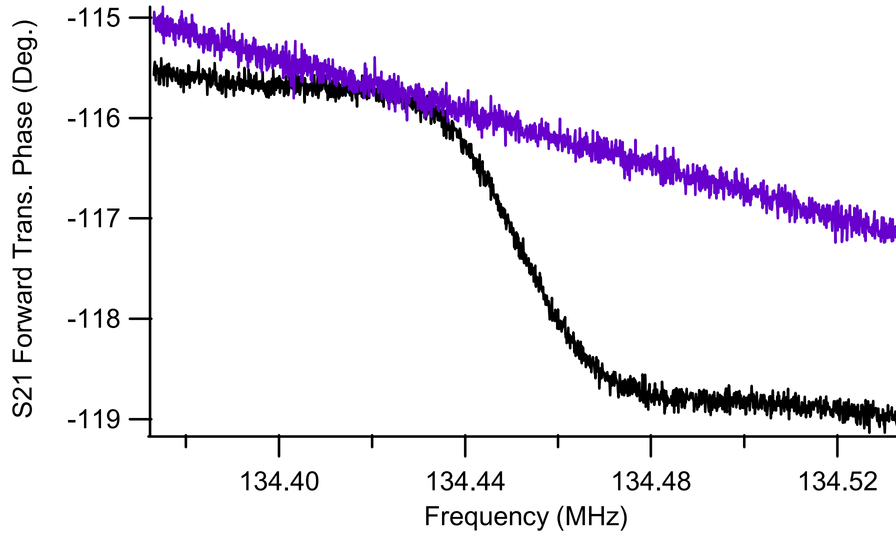

Figure 9B. S_{21} phase. The black trace is the measured signal and the purple trace is the feedthrough.

S_{22}, S_{12}, and S_{21} were redefined with respect to the feedthough levels measured for each parameter. The relative phase θ_{Rxy} for each S parameter was defined as:

(B.5) $$\theta_{Rxy} = \theta_{xy} - \theta_{xyFT}$$

where θ_{xy} corresponds to the black phase traces measured for each S_{xy} and θ_{xyFT} corresponds to the purple feedthrough levels measured (Figs. 5B,7B and 9B) for each S_{xy}. θ_{xyFT} was then set to zero over the 160 kHz frequency span depicted in Figs. 5B,7B and 9B. The real and imaginary components of S_{22}, S_{12}, and S_{21} were also normalized to the feedthrough levels:

(B.6) $$S_{Rxy} = M_{xy}cos(\theta_{Rxy}) + jM_{xy}sin(\theta_{Rxy}) - M_{xyFT}cos(0) - jM_{xyFT}sin(0)$$

which reduces to:

(B.7) $$S_{Rxy} = M_{xy}cos(\theta_{Rxy}) + jM_{xy}sin(\theta_{Rxy}) - M_{xyFT}$$

where M_{xy} is the linear magnitude of the S parameters, black traces from Figs. 4B,6B and 8B, M_{xyFT} is the linear magnitude of the S parameter feedthrough levels, purple traces from Figs. 4B,6B and 8B. Equation (B.4) now becomes:

$$(B.8) \quad y_{21} = \frac{-2S_{R21}}{Z_0((1+S_{R22})-(S_{R12}S_{R21}))}.$$

Equations (B.8) and (B.2) were then used to calculate the transconductance of the device shown in Fig. 1B (see Fig. 10B). Since S_{12} was very small relative to the feedthrough level, the $S_{R12}S_{R21}$ term was dropped from Eq. (B.8) and the transconductance was recalculated (Fig. 11B). Finally S_{R22} was also eliminated from Eq. (8.B) leaving only S_{R21} to calculate the transconductance (Fig. 12B):

$$(B.9) \quad y_{21} = \frac{-2S_{R21}}{Z_0}.$$

The peak values of transconductance for Figs. 10B-11B were 6.69X10^{-6} μS compared to 6.68X10^{-6} μS for Fig. 12B. Therefore, the only S parameter that matters for the mechanically coupled out-of-phase resonators is S_{21}.

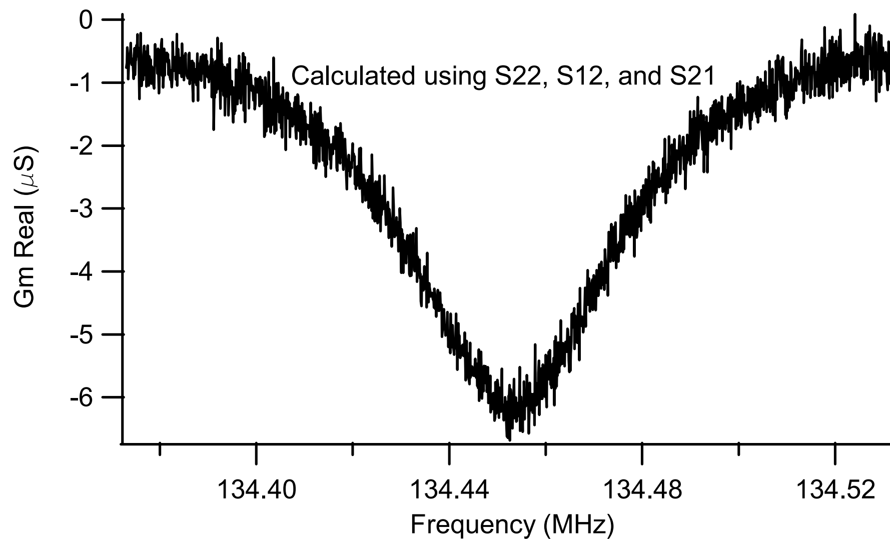

Figure 10B. Transconductance calculated using Eqs. (B.8) and (B.2).

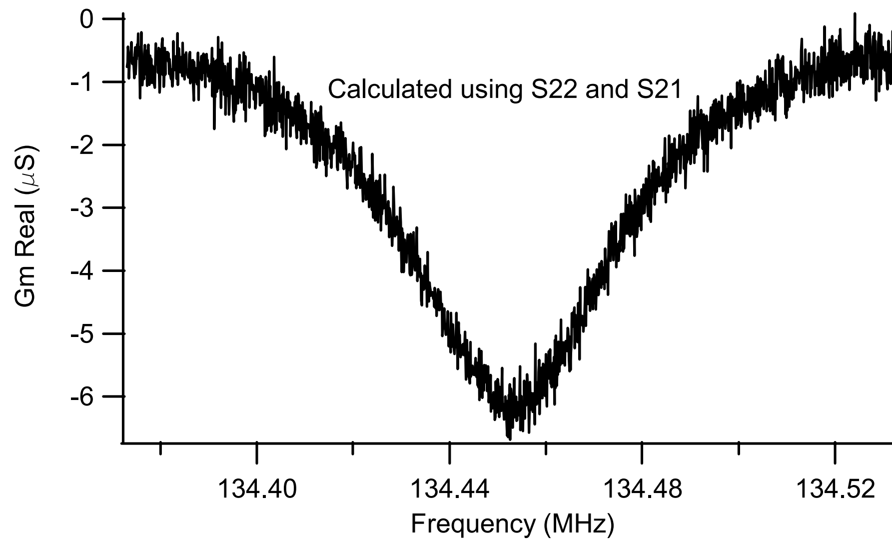

Figure 11B. Transconductance calculated using Eqs. (B.8) and (B.2) without S_{R12}.

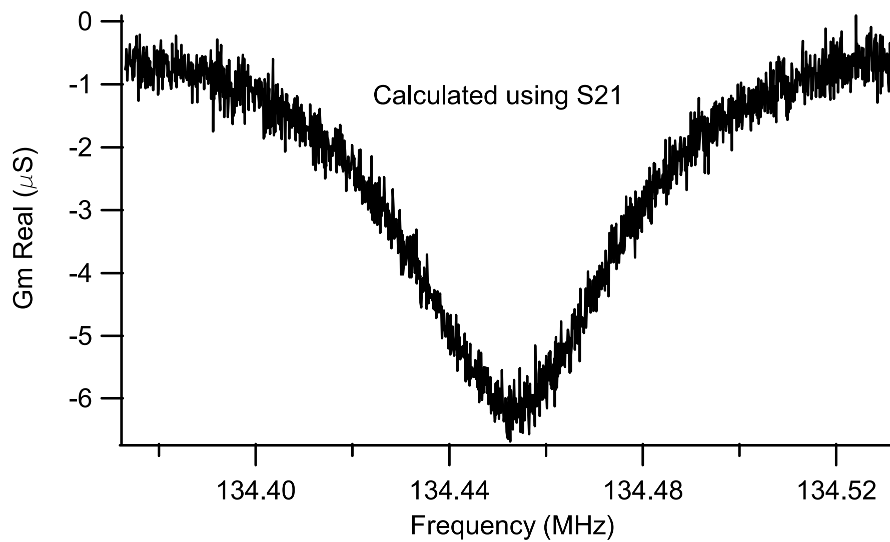

Figure 12B. Transconductance calculated using Eqs. (B.9) and (B.2).

OP-A Transconductance Calculations

The transconductance for OP-A was calculated at V_D = 5.5 and 5.9V using only the S_{21} forward transmission measurements (Figs. 13B-16B). The feedthrough levels for these devices were estimated using the one port capacitive measurements. The transconductance plots for 5.5 and 5.9V are given in Figs. 16B and 17B respectively.

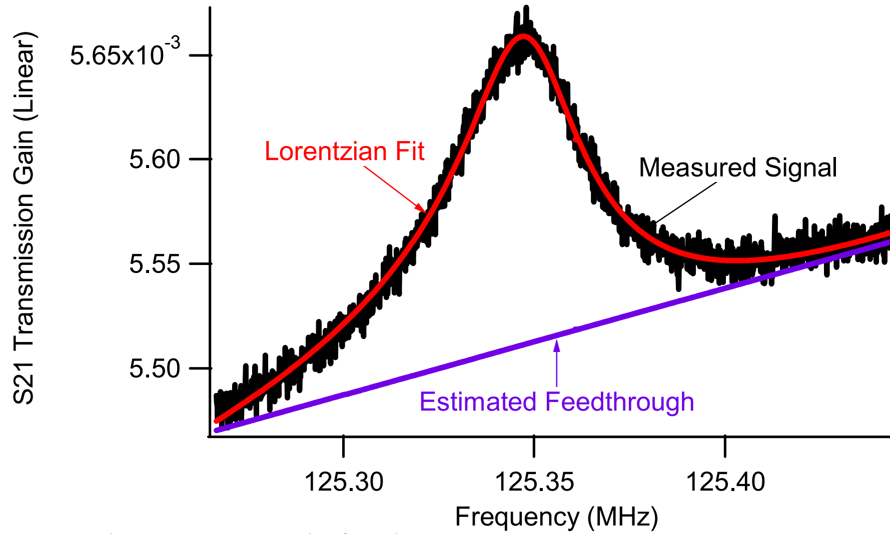

Figure 13B. S_{21} linear magnitude for device OP-A at V_D = 5.5V, V_S = 2V, V_G = 0V, and P_{RF} = -14dBm. The feedthrough level was estimated with the one-port capacitive transmission.

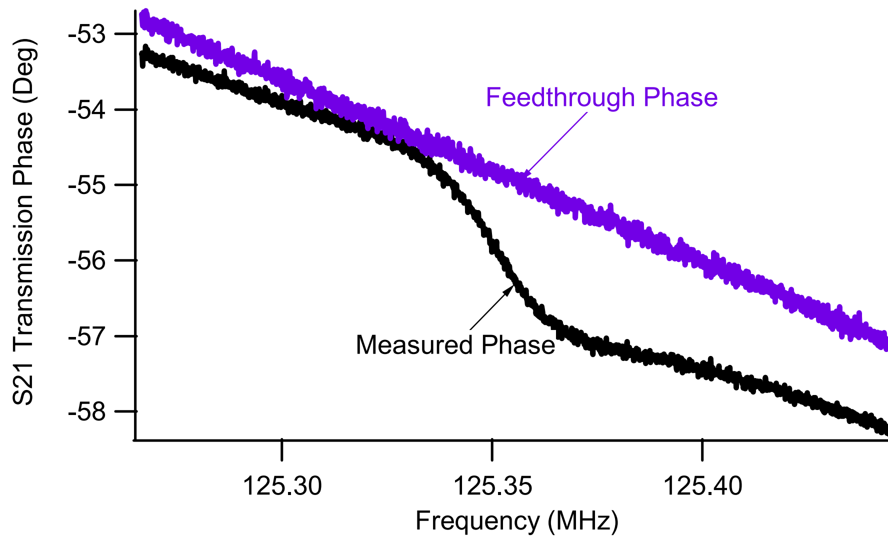

Figure 14B. S_{21} phase for device OP-A at V_D = 5.5V, V_S = 2V, V_G = 0V, and P_{RF} = -14dBm. The feedthrough level was estimated with the one-port capacitive transmission.

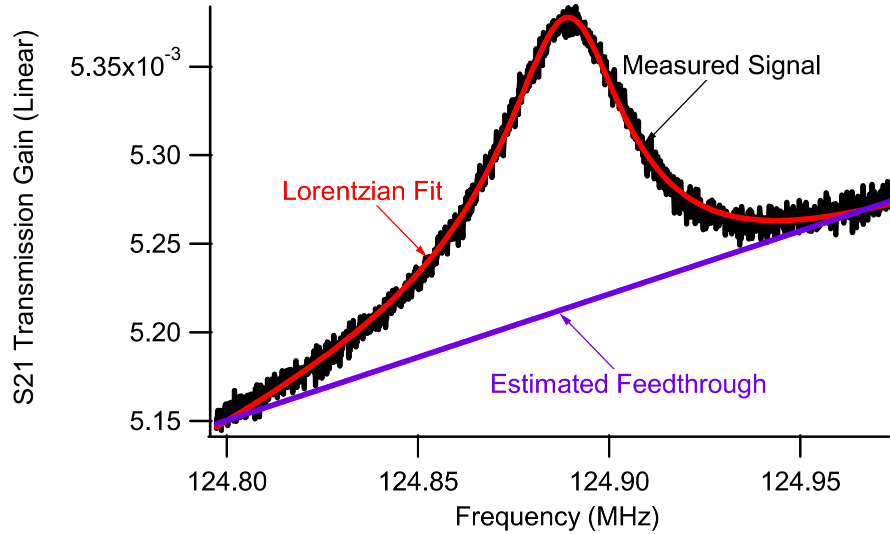

Figure 15B. S_{21} linear magnitude for device OP-A at V_D = 5.9V, V_S = 2V, V_G = 0V, and P_{RF} = -14dBm. The feedthrough level was estimated with the one-port capacitive transmission.

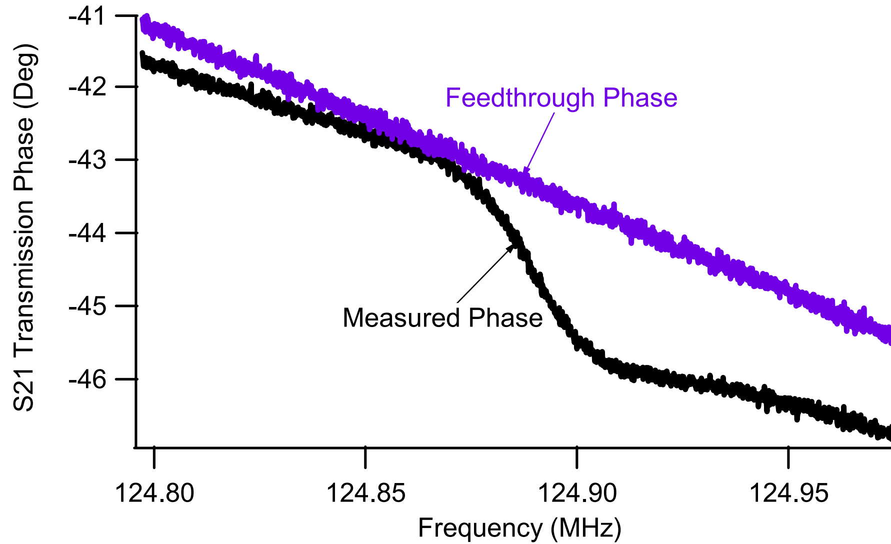

Figure 16B. S_{21} phase for device OP-A at V_D = 5.9V, V_S = 2V, V_G = 0V, and P_{RF} = -14dBm. The feedthrough level was estimated with the one-port capacitive transmission.

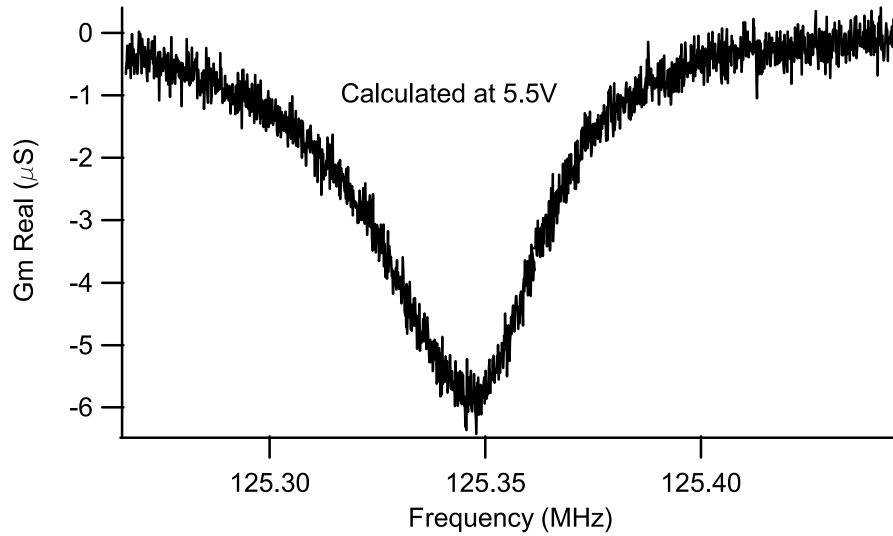

Figure 17B. Transconductance calculated using eqs. (B.8) and (B.2) for device OP-A at V_D = 5.5V, V_S = 2V, V_G = 0V, and P_{RF} = -14dBm.

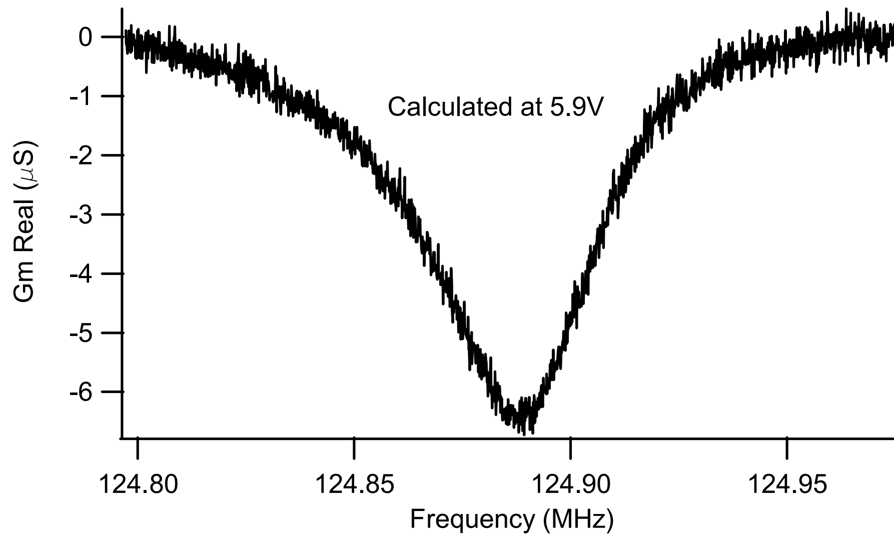

Figure 18B. Transconductance calculated using eqs. (B.8) and (B.2) for device OP-A at V_D = 5.9V, V_S = 2V, V_G = 0V, and P_{RF} = -14dBm.

Reference:

[1] J. Saijets and M. Aberg, "MOSFET RF Extraction Uncertainties Due to S Parameter Measurement Errors," *Physica Scripta*, Vol. T114, 2004, pp.244-247.

Appendix C. Top-Down and Bottom-Up Process Integration

A fabrication process was developed to integrate bottom-up VLS nanowires with top-down silicon on insulator (SOI) microstructures. VLS nanowire nucleation sites were defined on the sidewalls of the microstructures with i-line photolithography followed by a hydrofluoric acid etch step to remove oxide from the lateral surfaces of the microstructures. The process was used to create microstructures suspended by arrays of lateral silicon nanowires. The simplest structure consisted of a nanowire array clamped to the sidewall of an anchor structure at one end and to a freely suspended micropaddle at the other; the device resembled a single clamped microcantilever with a body composed of a uniformly dense, well-oriented nanowire array instead of bulk Si (see Fig. 1C).

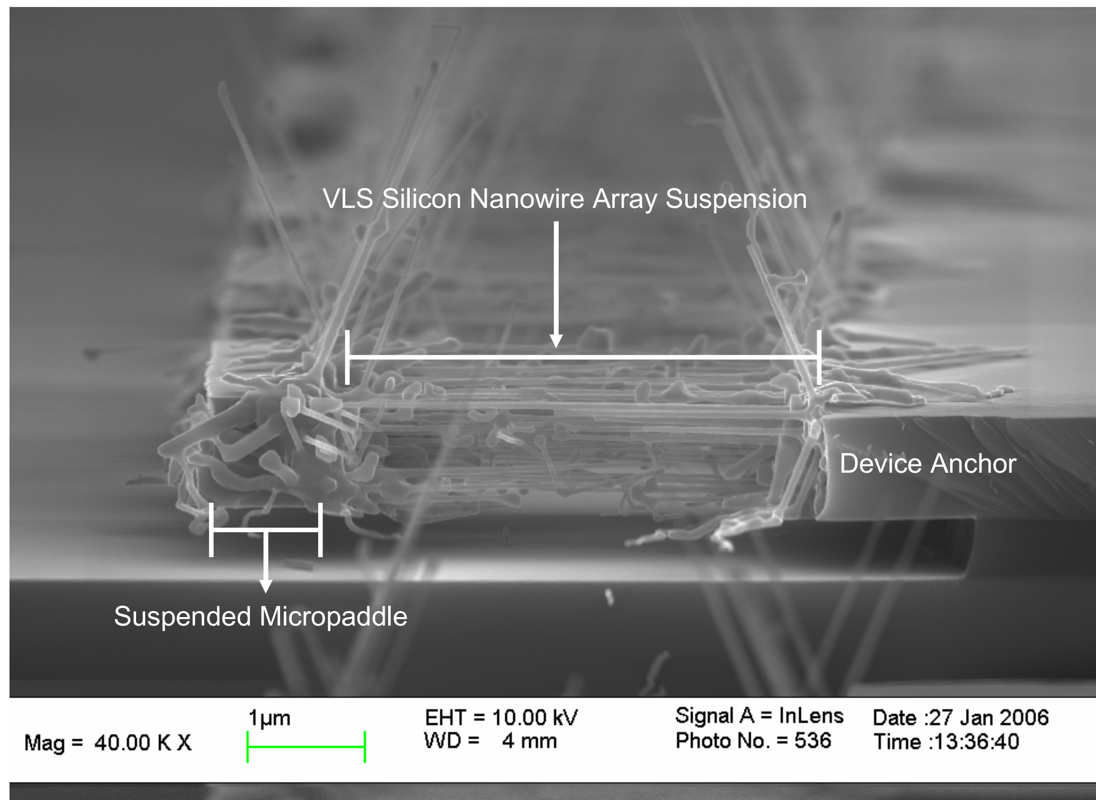

Figure 1C. Released silicon nanowire array based microcantilever. SOI sidewalls are (111) to grow lateral VLS nanowires.

Six inch (110) SOI wafers with (111) flats were used as the starting material for the merged process (Fig. 2C). The (111) oriented crystal planes were required to grow lateral VLS nanowires from the sidewalls of the microstructures [1].

First, the device layer was thermally oxidized to obtain a 160 nm thick oxide layer (Fig. 3C). Then, the micropaddles and the anchors were defined with (111)-oriented

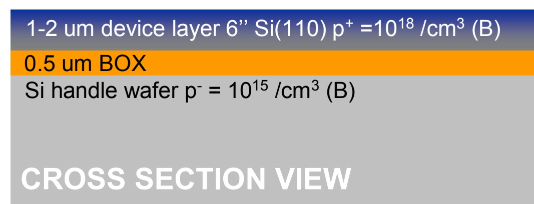

Figure 2C. Top view and cross section view of the boron doped (110) SOI wafer.

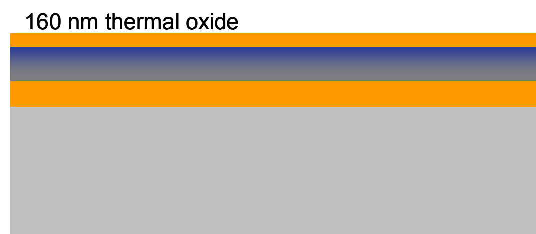

Figure 3C. A 160 nm thick thermal oxide was grown on the device layer

sidewalls with optical lithography and subsequent reactive ion etching of the top oxide and Si device layer (Fig. 4C). A 50 nm oxide was thermal grown or deposited (high temperature oxide) on the trench sidewalls (Fig. 5C). A final lithography step was

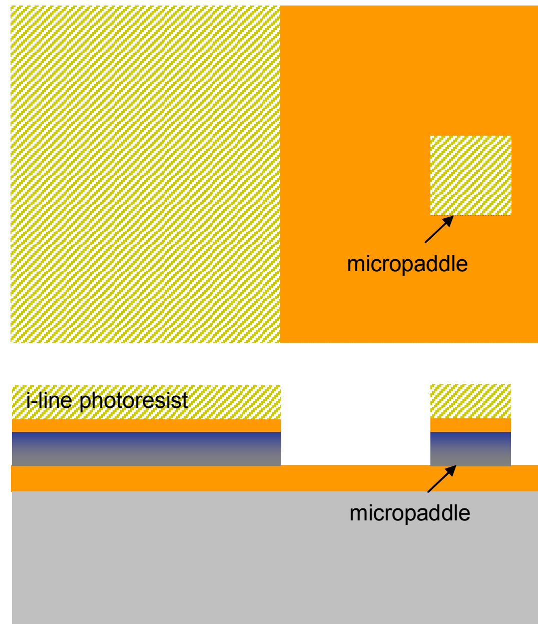

Figure 4C. The micropaddle was defined and etched into the device layer.

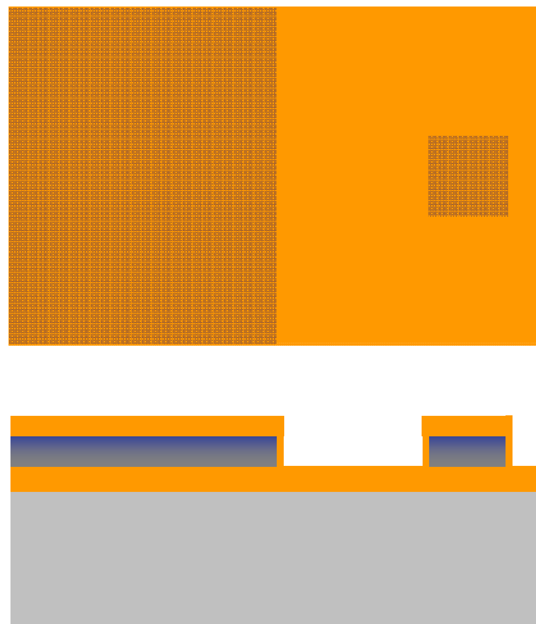

Figure 5C. A 50 nm oxide was deposited or thermally grown on the microstructure sidewalls.

used to define the sidewall areas from which the nanowires were grown. The oxide film on the lithographically exposed areas was etched with 10:1 buffered hydrofluoric acid (BHF). The etch rate of thermal oxide in 10:1 BHF was relatively stable at 1 nm/sec. The photoresist patterned wafers were placed in a 10:1 BHF bath for 55 sec to remove the 50 nm thick oxide film from the sidewalls. Five extra seconds were added to the time to ensure that the oxide was completely removed from the sidewall surfaces while only a fraction of the oxide on top of the microstructures was consumed (Fig. 6C).

The silicon nanowires were selective grown from the sidewall surfaces where the oxide was removed. This was accomplished by selectively depositing catalyst particles on the exposed silicon sidewalls with a galvanic displacement process (Fig. 7C). Then, the nanowires were grown in an atmospheric chemical vapor furnace at 850 °C using a $SiCl_4$ precursor [2]. The buried oxide was etched to release the microstructures (Fig. 8C).

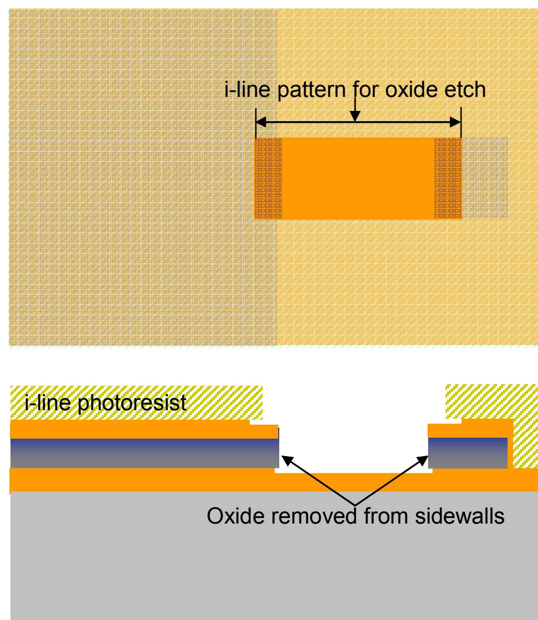

Figure 6C. The second mask of the process defines the target lateral nanowire growth surfaces. The oxide was removed from the microstructure sidewalls while the oxide on the top surface was partially etched.

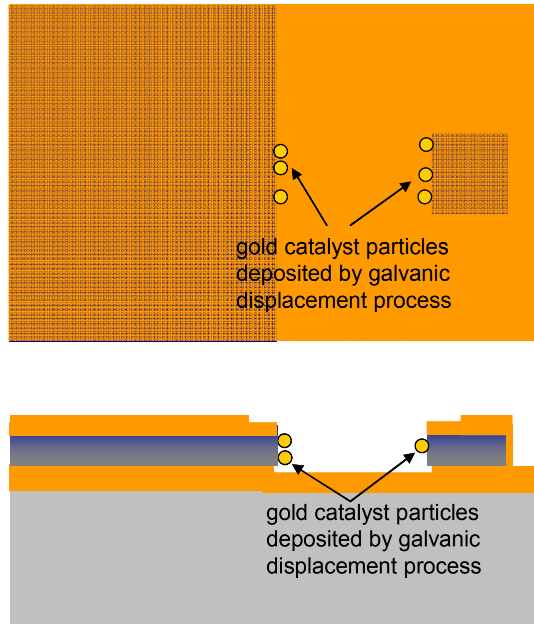

Figure 7C. Galvanic displacement was used to deposit gold nanoparticles on the exposed silicon sidewall regions.

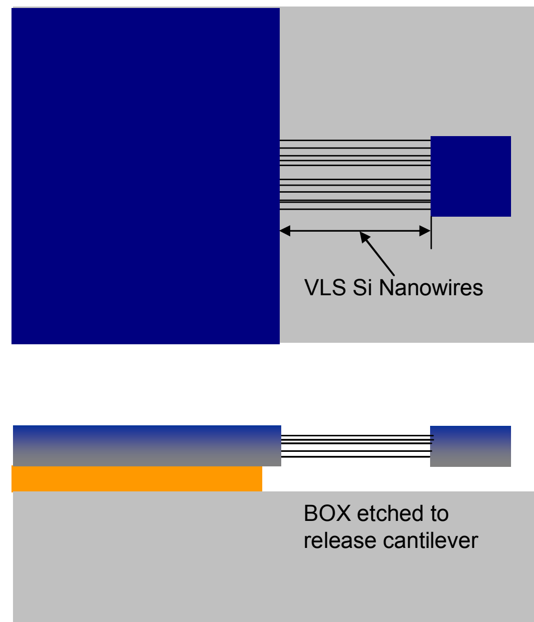

Figure 8C. Nanowires were grown following catalyst deposition and the structures were released in 5:1 BHF followed by a critical point drying step.

The defining characteristic of the process was the galvanic displacement method used for the deposition of the Au catalyst nanoparticles which was adapted from [3]. In this process, the Au nanoparticles were deposited by placing the substrates in a reversed micelle microemulsion that was prepared by mixing a water-based plating solution with *n*-heptane and a surfactant, sodium bis(2-ethylhexyl) sulfosuccinate (AOT, $C_{20}H_{37}O_7SNa$). The water based solution consisted of 0.2 M HF and 0.01 M $KAuCl_4$. The AOT/heptane solution was made by dissolving 0.33 M AOT in *n*-heptane. The two solutions were mixed to make microemulsions with different water-to-surfactant molar ratios R = [H2O]/[AOT]. The reversed micelles that were formed in the microemulsions contained the water-based solution and had a radius R_m that depended on R according to the empiric law $R_m = 0.175R + 1.5$ nm [4]. It has also been demonstrated that the diameter of the resulting Au nanoparticles was directly proportional to the diameter of the micelles, providing a means of controlling the diameter of the Au nanoparticles and consequently the diameter of the nanowires [3].

An AFM was used to characterize the mechanical properties of the nanowire array based cantilevers shown in Fig. 9C. Measurement details are given in [2]. The total spring constant, k_{TOTAL}, of the devices was:

(C.1) $$k_{TOTAL} = \frac{k_{ARRAY}}{n_{ARRAY}}$$, where

(C.2) $$k_{ARRAY} = N_{NW} k_{NW} = \frac{12 N_{NW} E_{(111)} \pi R_{NW}^4}{4 L_{NW}}$$

n_{ARRAY} corresponds to the number of nanowire arrays in each cantilever device, k_{ARRAY} is the spring constant of one array of nanowires, N_{NW} is the number of parallel nanowires in

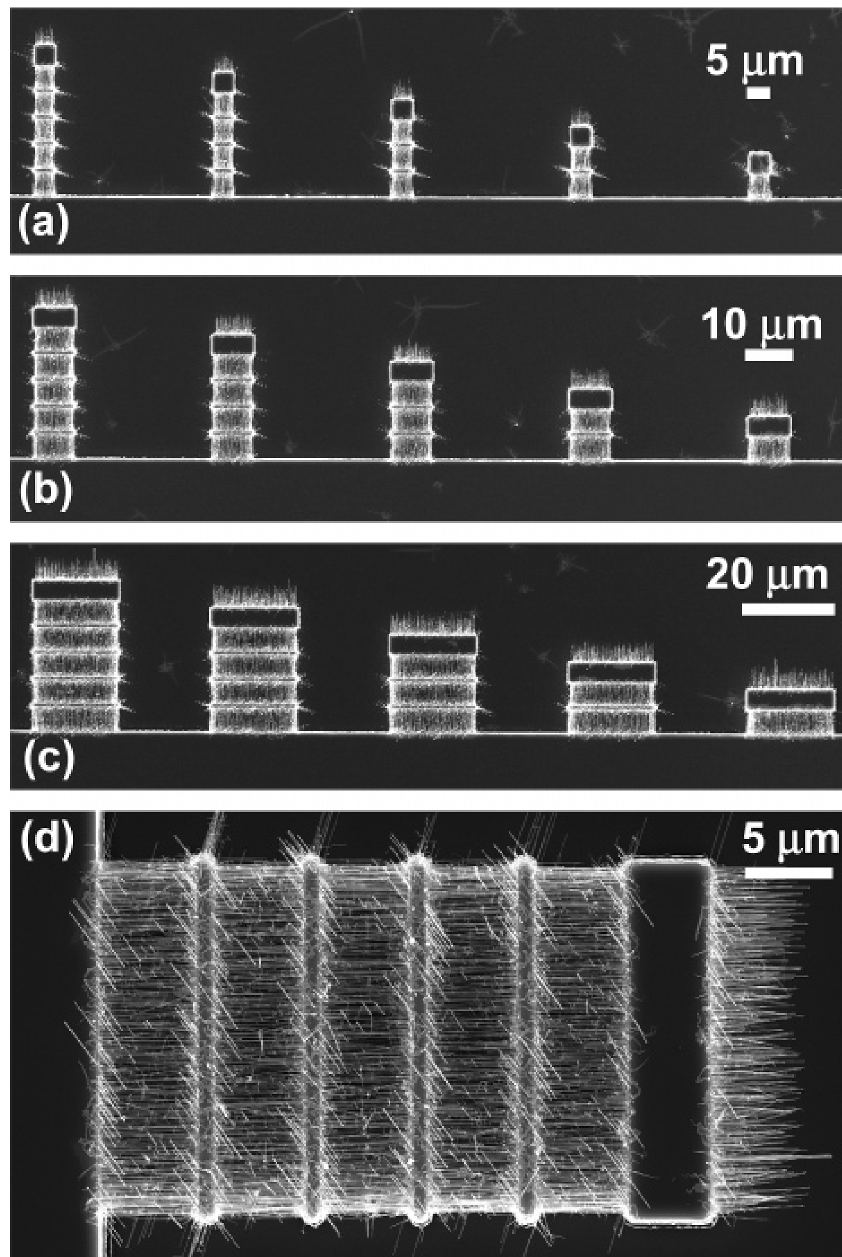

Figure 9C. Structures fabricated for AFM mechanical characterization: A) 5 μm wide structures with one to five linked arrays (right to left) of 5 μm long nanowires; B) 10 μm wide structures with one to five linked arrays; C) 20 μm wide structures with one to five linked arrays; D) 20 μm wide structure composed of 5 arrays of 5 μm long nanowires.

each array, k_{NW} is the spring constant of a single nanowire, L_{NW} and R_{NW} are the length and radius of an individual nanowire, and $E_{(111)}$ = 169 GPa. The measurement results demonstrated the general trends predicted by Eqs. (C.1)-(C.2) (Fig. 10C). The 20 μm wide cantilevers were stiffer than both the 10 and 5 μm wide cantilevers because there were more nanowires in the 20 μm wide nanowire arrays. Cantilevers composed of more than one nanowire suspension array had lower spring constants (Fig. 10C).

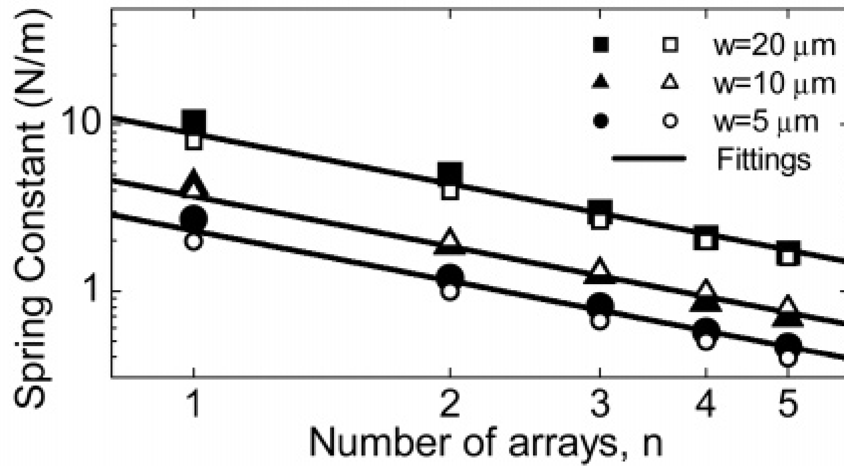

Figure 10C. Spring constant vs number of arrays obtained by linear fittings of force vs deflection data. Solid symbols correspond to experimental results while hollow symbols represent data obtained from finite element simulations.

Single nanowire devices could also be created by diluting the micelle based galvanic displacement process. Low density nanowire arrays were grown, with Greg Döerk's aid, between two patterned electrodes with a gate electrode in close proximity, Figs. 11 and 12C. These devices were designed to be single nanowire resonators, however, the nanowires that were grown on these chips were not conductive enough to

generate a detectable RF current using the mixing detection method described in Chapter 4.

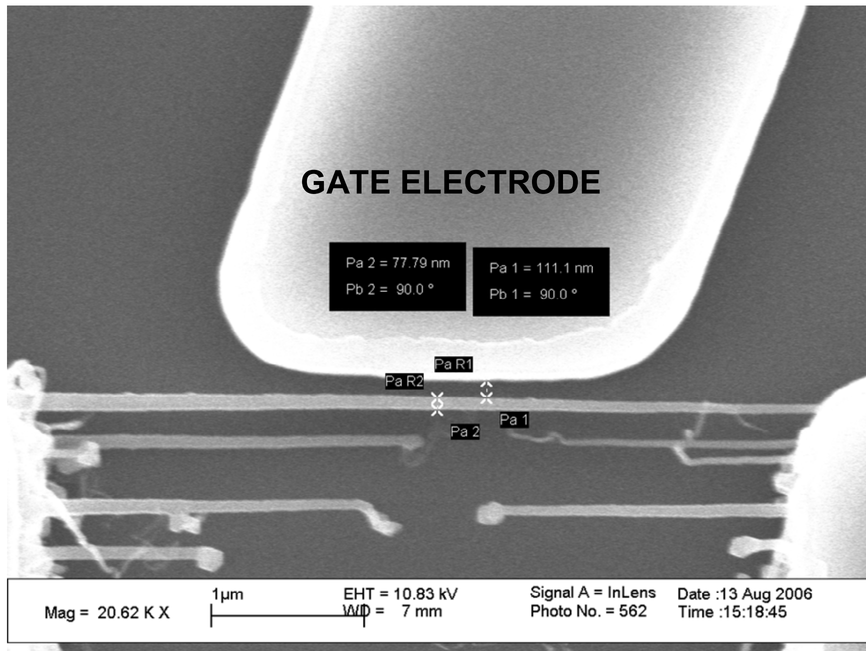

Figure 11C. 5 μm long, 79 nm wide silicon nanowire. The gate was 111 nm away from the wire

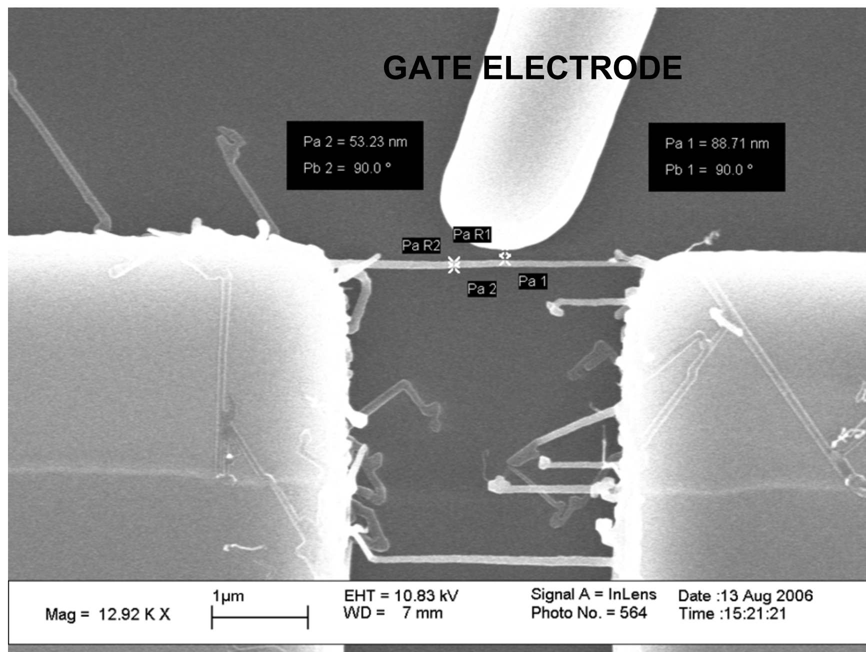

Figure 12C. 2.5 μm long, 53 nm wide silicon nanowire. The gate was 90 nm away from the wire.

Appendix C References

[1] M. S. Islam, S. Sharma, T. I. Kamins, and R. S. Williams, "Ultra-high-density silicon nanobridges formed between two vertical silicon surfaces," Nanotechnology, Vol. 15, Jan. 2004, pp.L5-L8.

[2] A. San Paulo, et al., "Suspended Mechanical Structures Based on Elastic Silicon Nanowire Arrays," *Nano Letters*, Vol. 7, No. 4, pp.1100-1104.

[3] D. Gao, et al., "Selective Growth of Si Nanowire Arrays via Galvanic Displacement Processes in Water-in-Oil Microemulsions," J*ournal of the American Chemical Society*, Vol. 127, May 2005, pp.4574-4575.

[4] L. Magagnin, V. Bertani, P. L. Cavallotti, R. Maboudian, and C. Carraro, "Selective deposition of gold nanoclusters on silicon by a galvanic displacement process," Microelectronic Engineering, Vol. 64, 2002, 479-485.